A COMPARISON OF FLUID AND HEAT CONTROL CONCEPTS

FOR A

BINARY RANKINE CYCLE

SOLAR DYNAMIC SPACE POWER SYSTEM

by

Seung Jin Song

BSE, Duke University

(1986)

SUBMITTED IN PARTIAL FULFILLMENT

OF THE REQUIREMENTS OF THE

DEGREE OF

MASTER OF SCIENCE

IN AERONAUTICS AND ASTRONAUTICS

at the

MASSACHUSETTS INSTITUTE OF TECHNOLOGY

January 1988

© Massachusetts Institute of Technology 1988

Signature of Author_____
Department of Aeronautics and Astronautics
January 15, 1988

Certified by_____
Professor Jean F. Louis
Thesis Supervisor

Accepted by_____
Professor Harold Y. Wachman
Chairman, Departmental Committee on Graduate Students

1

A Comparison of Fluid and Heat Control Concepts
for a
Binary Rankine Cycle
Solar Dynamic Space Power System
by
Seung Jin Song

Submitted to Department of Aeronautics and Astronautics
on January 15, 1988 in partial fulfillment of the
requirements for the Degree of Master of Science in
Aeronautics and Astronautics

ABSTRACT

A conceptual study was done to reduce the mass and improve the reliability of the solar dynamics space power system; the efforts were focused on the fluid and heat control components. A mercury-toluene binary Rankine cycle with 25 kWe output at 42% efficiency was used as the base cycle.

A survey of literature on bearings and seals was done for application in containing the working fluids in turboalternator pumps. A fluid control system using gas lubricated foil journal bearings, spiral groove thrust bearings, and ferrofluidic seals is suggested. One possible lubricant is nitrogen. A preliminary design of rotating film radiator suggests that a radiator with a specific mass of 5.5 kg/kWt or 3.52 kg/m^2 is attainable. Lastly, a receiver with liquid lithium thermal storage system is suggested. The concept circumvents the thermal energy storage material containment problem and reduces its associated mass. A preliminary design suggests that a specific mass of 5.90 kg/kWt for the collector-receiver assembly. The study concentrated on using existing technologies to assure reliability.

Thesis Supervisor: Dr. Jean F. Louis
Title: Professor of Aeronautics and Astronautics

Acknowledgement

I express my sincere gratitude to Professor Louis for giving me the opportunity to work on this project. His insight, advice, and patience throughout the project have been much appreciated. Working with Professor Louis has been an enlightening experience.

I would like to thank my friends at MIT for their support, especially the members of Korean Graduate Students Association, Bor Chuyan Lin, and Randy Cotton.

Finally, I express my deepest appreciation and gratitude to my parents for their never-ending sacrifice, support, and love.

List of Symbols

C_p = specific heat (J/kg K)

D = hydraulic diameter

dx = width of oil flow sections in the heat exchanger for rotating film radiator

δ = film height, condensate layer height

ϵ = emissivity

ff = friction factor

Δh= enthalpy difference

h = heat transfer coefficient (W/m^2K)

η = efficiency

k = thermal conductivity (W/m K)

l = half height of RBMR container (m)

lfin = fin length

m_i = mass flow rate of substance i

μ =absolute viscosity (kg/m s)

NOT = number of oil flow sections in heat exchanger

Nu = Nusselt Number

Pr = Prnadtl Number

ρ = density (kg/m^3)

r = radius (m)

Re = Reynolds Number

σ = Stefan Boltzmann constant, surface tension

τ = shear stress

T = absolute temperature (K)

v = specific volume (m^3/kg)

ν = kinematic viscosity (m^2/s)

V = velocity (m/s)

ω = rotational speed (rpm)

x = quality

Subscripts

i = inside

o = outside

r, θ, z = axes in the polar coordinate system

vap, g = vapor

f = liquid

w = wall

List of Figures

.

List of Tables

Chapter 1

INTRODUCTION

Currently, NASA envisions an operational permanent manned Space Station by the mid-1990's. The Space Station would serve as a base camp for further space exploration, scientific research, and space industrialization. Such ventures will require durable, multi-kilowatt electrical power systems (EPS) which can adapt to the evolving Space Station needs. The launch schedule and costs constrain the EPS design. Meeting the 1990 launch deadline and the 10-year-long service life requirement at a reasonable cost requires a technically mature EPS which is more efficient, lighter, and more compact than current designs.

The three competitive EPS types are photovoltaic, solar dynamic, and nuclear systems. Photovoltaic EPS contains solar arrays, which convert solar energy into electricity, and electrochemical batteries, which store electricity for the eclipse of each orbit. The solar dynamic EPS concentrates the solar energy via a mirror and heats a fluid which, in turn, drives a turbine to generate power. The energy storage is done in a thermal energy storage (TES) system which utilizes either latent or sensible heat. The nuclear EPS is similar to the solar dynamic EPS, except that a nuclear reactor acts as the energy source. Since the nuclear reactor can be run continuously, an energy storage system is not necessary.

The nuclear EPS has a thermal efficiency comparable to that of solar dynamic EPS. It is potentially preferable to solar dynamic systems for high power levels (1 MW) because light, compact reactors can replace the bulky collector mirror and TES. However, for the anticipated initial power range of 75-300 kWe, the mass of shielding necessary for protection of personnel and equipment from radiation makes the nuclear EPS heavier than the solar dynamic EPS. Furthermore, nuclear EPS poses extra safety issues such as its effect on astronauts' extra-vehicular activity (EVA) and the safety of reactors during launch and reentry.

Photovoltaic EPS have successfully powered most of the past space ventures; therefore, it has the highest technical maturity and poses the least development risk. However, its low efficiency (~10%) requires large solar arrays and high capacity batteries. The large arrays can interfere with EVA and shuttle docking. Furthermore, the low-earth orbit (LEO) of the Space Station will cause excessive atmospheric drag on large surface

structures. The high drag will require frequent boosting which increases the system maintenance cost. Worse yet, the high specific masses of arrays and batteries mean a massive system with high launch costs.

Although it lacks the technical maturity of the photovoltaic EPS, the solar dynamic EPS also offers many advantages. Its high thermal efficiency (20-40 %) decreases the size and mass of the collector mirror and radiator, the two most massive components of the EPS. Smaller components allow compact configuration which is easier to control. Also, the TES is lighter than the heavy electrochemical batteries used by photovoltaic EPS. Furthermore, the solar dynamic EPS can provide both thermal and electrical energy (cogeneration) at any temperature within the cycle's temperature range. This leads to an even more efficient energy production as the thermal energy can be directly supplied from the heat rejection legs of the cycle without going through the losses in the thermal-mechanical-electrical-thermal transformation process.

Three candidate cycles for solar dynamic EPS are Stirling, Brayton, and Rankine Cycles. Due to the extensive terrestrial experience with the latter two, much of research effort to date has focused on Rankine and Brayton Cycles. Rankine cycle is a two-phase cycle in which a liquid is pumped, vaporized, expanded, and condensed. Brayton cycle is a single-phase cycle in which a vapor is compressed, heated, expanded, and cooled. In both cycles, energy is extracted during the vapor expansion leg.

Relative to the Brayton Cycle, the Rankine Cycle has the following disadvantages. First, the stability of two-phase flow in zero gravity is uncertain; vapor contact with heat exchanger surface can form hot spots which can cause premature failure. Second, the risk of pump cavitation exists if the inlet pump pressure is not properly controlled. Third, low quality vapor expansion can cause turbine erosion.

However, the Rankine Cycle also offers important advantages over the Brayton Cycle. First, constant temperature heat rejection, instead of over a range of temperatures, results in a lighter radiator. Second, pumping a liquid takes much less work than compressing a vapor: therefore, more net power can be extracted per given enthalpy drop. Most importantly, however, the constant temperature heat addition and rejection in the Rankine Cycle yields a high thermal efficiency which, theoretically, can approach the Carnot efficiency (Figure 1). Heat addition/rejection over a range of temperatures in Brayton Cycle causes large irreversibility and lowers effiency. Thus for comparable pressure and temperature ratios the Rankine Cycle can attain higher efficiency which reduces mass.

According to Fox [1], the Rankine Cycle's efficiency can be increased to over 40% by adding a topping cycle. Current Organic Rankine Cycle (ORC) systems have efficiencies of about 20 % because the maximum

.

temperature is limited to prevent excessive degradation of the working fluid (e.g. toluene). The addition of a topping cycle raises the thermal efficiency by increasing the heat addition temperature without increasing the working fluids' degradation rate. The system configuration is shown in Figure 2.

To reduce the overall mass and improve the reliability of the Binary Rankine Cycle, following key issues were identified; first, the design of a light weight condenser/boiler unit which can connect the topping cycle with the ORC for varying power outputs: second, containment of working fluids: and third, mass reduction of the two most massive components in the system, the radiator and the collector-receiver assembly. The first issue has already been addressed by Cotton [2]. The study found that a light-weight, compact condenser/boiler, whose mass is insignificant relative to the overall mass, can be built with existing technologies.

This thesis deals with the remaining two issues. Chapter 2 describes the reference cycle and the working fluids. The next two chapters focus on fluid control issues with emphasis on sealing the working fluids in the turbo-alternator-pumps (TAP). Chapter 3 discusses the bearing concepts and chapter 4 discusses the seal concepts. The remaining chapters address the thermal issues by focusing on the the radiator and the collector-receiver assembly. Chapter 5 contains a description and a preliminary design of a rotating film radiator (RFR) concept. Chapter 6 compares different receiver/TES concepts and recommends a concept utilizing liquid lithium TES. Chapter 7 contains conclusions and appendices contain analyses for different components.

Chapter 2

Binary Cycle

The reference binary cycle assumed in this thesis is equivalent to the one initially set by Fox [1] and modified by Cotton [2]. The objective of their cycle analyses was to improve the cycle efficiency utilizing only the well-proven components and working fluids.

Toluene (C_7H_8) and mercury were chosen as working fluids for the following reasons. Toluene has outstanding thermodynamic properties. The positive slope of liquidus on T-s diagram (Figure 3) means that any vapor expansion would occur under dry conditions, removing the risk of erosion. Its low critical pressure allows supercritical vaporization, eliminating problems associated with two-phase flow in zero-gravity. Its high heat of vaporization means large heat transfer capacity for a given temperature range. Furthermore, it has sufficiently high viscosity to be a lubricant [1].

Mercury has relatively low heat of vaporization which increases the required mass flow rate. Furthermore, its high vapor pressure and steep liquidus means that supercritical vaporization is not viable and that superheat is necessary to avoid erosion problems during the vapor expansion leg (Figure 4). Nevertheless, its high density results in mercury having the highest heat transfer rate per volume flow rate [1].

Best of all, both fluids have been well tested and extensively used. Mercury has been used as a working fluid in many terrestrial applications and tested for many hours in space-like environment during the SNAP-8 tests. Sundstrand has been testing Organic Rankine Cycle (ORC) using toluene for many years [3].

Fox set the following conditions on the reference cycle.

Maximum mercury temperature	1033 K
Minimum mercury temperature	654 K
Maximum toluene temperature	644 K
Minimum toluene temperature	350 K
Mercury turbine efficiency	0.75

Cotton set the cycle and determined power and heat transfer rates for each cycle by assuming certain pump and turbine efficiencies and pressure drop in each cycle. Figure 5 shows the mercury cycle superimposed over the toluene cycle with a summary of cycle points. The net power and heat transferred from each cycle per unit mass flow rate of the cycle's working fluid are as follows

$Pnet/m_{Hg}$	78.51 kWe/(kg/s)
$Qout/m_{Hg}$	251.13 kWt/(kg/s)
$Pnet/m_{tol}$	144.99 kWe/(kg/s)
Qin/m_{tol}	554.00 kWt/(kg/s)

Matching the Qout with Qin and assuming combined alternator/power distribution efficiency of 81%, the shaft output required to produce 25 kWe is 30.08 kWt. The reference cycle values are shown in the first section of Table 5.

Using the assumptions made by Fox [1], the binary Rankine cycle solar dynamic EPS mass-breakdown is as follows.

Collector Mirror	477 kg
Receiver	161 kg
Radiator	250 kg
Turbomachinery	34 kg
Condenser/Heater	8 kg
Regenerator	8 kg
Alternator and PMAD	15 kg

In the above mass-breakdown, the assumed receiver specific mass is 2.3 kg/kWt and the radiator specific mass is 5 kg/m² which are lower than the industrial figures of 10 kg/kWt and 10 kg/m², respectively. Even with these assumptions, the collector-receiver assembly and radiator masses account for 888 kg out of the total 953 kg. Since reductions in the masses of these components can favorably increase the specific power of this system, chapters 5 and 6 focus on reliable methods to reduce the masses of the radiator and the collector-receiver assembly. To improve the reliability of the EPS, attention was focused on the rotating machinery since they are inherently less reliable than components without moving parts. Furthermore, bearings and seals for the rotating machinery were identified as the critical components in not only preventing rotating machinery failure but also containing the working fluids and the next two chapters discuss the issues associated with the two components.

Chapter 3

Bearings for Turbo-Alternator-Pump

Prevention of contamination and containment of working fluids in the binary cycle depend strongly on the performance of the system's bearings and seals. Of the two, the bearings determine the type of seals needed. Therefore, a judicious choice of bearings could simplify the bearing/seal design, improve its efficiency, and reduce its mass. This chapter reviews past bearing designs and discusses a conceptual fluid control system using gas bearings and ferrofluidic seals.

The space environment is affected by the following particularities not encountered on earth: first, very low ambient pressure: second, radiation: third, presence of atomic or ionized oxygen and nitrogen: fourth, zero-gravity condition [4]. The vacuum causes accelerated evaporation of conventional lubricants such as oil and semi-solid grease; however, for a hermetically sealed system, the space vacuum should not affect the performance of the bearing system. The level of radiation, while considerable, is insufficient to damage either the bearing or the lubricant. The lack of molecular oxygen would retard the formation of oxide film on metal surfaces; the effects of such reduced protective oxide film formation on the friction and wear of the bearings is not clear. If necessary, however, such an oxide layer could be formed by operating the system on the ground prior to space operations. The zero-gravity conditions would lead to light load conditions which cause instability problems in radial bearings such as the half frequency swirl.

The binary cycle's turbo-alternator-pumps (TAP) are high speed, high temperature devices with a requirement of 10-year-long service life. The main loads on the bearings will be from the rotor imbalance/dynamics and the alternator's magnetic asymmetry. Under these conditions, efficiency, durability and reliability are of prime importance in the bearings.

3.1. Comparison of Bearing Types

The bearings are categorized into rolling element bearings and fluid film bearings. The rolling element bearings' capacity results from the direct contact of ball/rollers with both the journal and the bearing. The fluid film bearing use either gas or liquid for both lubrication and load capacity generation. The load capapcity is generated internally and/or externally (Figure 6)[5].

For application in TAP, the fluid film bearings offer more advantages than the rolling element bearings. The latter kind contains many attractive features such as reduced starting friction: less bearing power loss: higher tolerance of load, temperature, and speed fluctuations: stability at light load conditions: and ability to support both radial and axial loads. However, they are limited to moderate temperature and pressure ranges and need oil lubrication. Furthermore, the bearing materials have to meet the strict hardness requirement to withstand the contact loads, constraining the material selection. The direct contact results in a relatively high coefficient of friction at high speeds and can cause the bearing to fail without warning. Furthermore, the cyclic loads limit the reliability and the service life of the bearings [6].

Unlike the rolling element bearings, fluid film bearings can only support either radial or axial loads: therefore, a journal bearing and a thrust bearing are needed. Under light loads, the fluid film bearings are prone to experience fractional frequency instabilities. The most frequent one is the half frequency swirl in which the journal rotates about the bearings center at half the angular velocity at which the journal rotates about its own center. Also, in the case of liquid film bearings, the power losses are higher than in rolling element bearings. However, these weaknesses are more than offset by the lack of problems associated with direct contact. The fluid film bearings do not have the wear, friction problems and they do not have hardness constraint on material selection. Lastly, their performance at high speed and temperature is more efficient and reliable than the rolling element bearings [7].

Fluid film bearings are divided into six groups (Figure 6). They can be lubricated by either gas or liquid. Each group can then be subdivided into three subgroups. Hydrodynamic ones generate their own pressure: the hydrostatic ones are externally pressurized: and the hybrid ones are combinations of the former two (Figure 7). The hybrid bearings of both gas and liquid have been successfully tested in Brayton Rotating Units (BRU), potassium turboalternators, and Brayton Isotope Power Systems (BIPS) [8,9,10].

In the above examples, the tilting pad design was experimentally determined to be the most stable journal bearing. The tilting pad design was also more tolerant of thermal distortion, misalignments, and contaminant

particles than other bearings. However, its weaknesses are pivot wear; severe manufacturing and mounting tolerances; and the complexity of design.

Foil bearing development has sufficiently matured to substitute tilting pad bearing designs in the TAP. The two types of foil bearings, the cantilevered and the tensioned (Figure 8), are stable and have load capacity comparable to other types of bearings: a 1-in diameter shaft has been run upto 240.000 rpm without instability [11]. The bearings are also more tolerant than the tilting pad designs of dirt/moisture ingestion: they have been known to ingest particles larger than the clearance without failure and also run on liquid-vapor mixture without any problems. Furthermore, the compliance allows higher tolerance of thermal growth as well. and the much less severe manufacturing/mounting tolerance make them easier and cheaper to produce. The most significant advantage is the foil design's compactness and simplicity relative to the tilting pad design. Lastly. the foil bearing technology is a proven one. They have been successfully test-run on BRU's [12]. and have performed satisfactorily in various turbomachines under severe conditions. They performed under upto 22.6 g's and 811 K and showed mean time between failures of 55.00 to 95.000 hours [13].

For thrust loads, a bi-directional, spiral-groove, inward-pumping disk bearing is recommended (Figure 9). Foil thrust bearings is still in development stage. The tilting pad thrust bearing. like its journal counterpart. is complex, needing a load-equalizer and self-aligner for the pads: also it is sensitive to pressure fluctuations. On the other hand, the disk spiral-groove bearing is simple, and much design informations if readily available. The spiral groove was chosen because the grooves offer higher load capacity than steps. pockets or sectors in disks. and the inward-pumping was chosen over outward-pumping or the herringbone for the same reason [14].

3.2. Lubrication

As for lubrication, liquid lubrication offers high damping capability with better stability and a higher load/size coefficient than that of gas lubrication. However. they are limited to moderate temperature range by the lubricant's viscosity (μ_{liquid} $\frac{1}{T} \cdot \mu_{gas}$ $\sqrt{T}$). Gas lubrication, on the other hand. offers more efficient. and reliable performance at high temperature and speed: there is less bearing power loss and the temperature range is constrained by the material and not by the viscosity of the lubricant. Also. the cavitation problem is eliminated by using gas. However, one weakness is the low damping capability with consequent stability problems. Yet the air foil bearings' and He/Xe foil bearings' performances in airplanes and BRU's. respectively, show that such stability problems can be overcome [12, 13].

The three candidates for lubrication gases are toluene, mercury, and an inert gas such as nitrogen. Table

1 shows the physical properites of the three gases along with those of air. Toluene and mercury have sufficently high viscosity to be used as lubricants. However, the use of either in bearings would require a new technology development, and in the mean time, nitrogen, whose properties are similar to those of air, can be used for lubrication. Furthermore, until the seals prove themselves, nitrogen is also recommended as a purge gas for alternator rotor because of its relatively low density. Toluene, despite its high specific heat which would facilitate heat removal, is not recommended because of its high vapor density which would increase the windage losses.

3.3. Fluid Control System

The schematic of the proposed fluid control system is shown in Figure 10. Liquid toluene is used to cool the alternator stators, taking advantage of its high specific heat of 2.05 kJ/kg K at 400 K. Nitrogen, circulated through a separate loop, is used to purge the alternator rotor and lubricate the bearings. The system is an adaptation of the new Sundstrand RFMD concept [15].

Non-condensing nitrogen will be pumped through pipe 3 to cool the alternator rotors and lubricate the bearings. The liquid toluene will be pumped by a pitot tube (pipe 1) in the cold end of the RFMD to the alternator stator and the mercury seals to be used as the coolant. The nitrogen and mercury vapors will be kept separate by the ferrofluidic seals. Pipe 2 will return the liquid toluene to the RFMD and pipe 4 will return the nitrogen to the nitrogen pump. Visco-ferrofluidic mercury seals can be used on the mercury power shaft. These have shown zero leakage performance for sealing moderate-pressure gases [16]. Thus, intermixing or contamination of the vapors can be prevented.

As a redundant safety mechanism, an optional mercury trap is suggested: it is shown with dotted lines in Figure 10. Should any mercury/nitrogen vapor intermixing occur, the return flow in pipe 4 can be put through a cold mercury trap. This mercury trap could be a rotating mercury condenser cooled by liquid toluene or its own radiator. As the mercury condenses, the liquid mercury will centrifuge out and collect in pipe 5, later to be joined with other mercury in the cold end of mercury RFMD. The remaining nitrogen in the mercury trap will be returned to the nitrogen loop.

The system's advantages are many. First, the use of gas bearings simplifies the seal design by reducing the number of seals needed. This will be made more clear in the seal section. Such a reduction decreases the total power loss due to the seals. Second, the system solves the problems of contamination, separation and cavitation of working fluids. Furthermore, once the seals perform with zero leakage, the mercury trap and the

purge gas will no longer be necessary. Again, the reduction in auxilary equipment decreases the power loss and the system mass; simplifies the design; and increases the efficiency.

Use of toluene bearings will result in even more advantages. The toluene bearing system without the mercury trap is shown in Figure 11. Figure 11 is similar to Figure 10. except that, instead of nitrogen, some of toluene turbine exhaust is bled off through pipe 3 to the bearings and uitmately returned to the regenerator via pipe 4. Therefore, the nitrogen loop can be discarded altogether. Furthermore, lubrication with a working fluid assures a ready supply of the lubricant at all times. Lastly, toluene vapor's relatively high viscosity (Table1) shows that the toluene bearings could be more stable than either nitrogen or air bearings.

3.4. Conclusion

It should be pointed out that this conceptual design still needs studies, especially in the following areas. Experimental testing of foil bearing's response to the alternator magnetic imbalalnce is needed, even though the magnetic imbalance dod not affect the tilting pad bearing performance significantly [17]. Also, the gas foil bearings need more analysis to ensure satisfactory stability performance.

Chapter 4

Seals

Prevention of mercury loss, particularly the diffusion of mercury in the TAP is crucial to trouble-free operation of the mercury topping cycle. The system conditions require low leakage dynamic seals operating at high shaft speeds and temperature. For seal's working conditions, SNAP-8's conditions were assumed. Seals need to have a service life of 10,000 hours minimum at leakage rates of less than 1 lb/yr. Mercury vapor's temperature and pressure at the turbine outlet were 700 F and 20 psia, respectively. The 2-in-diameter shaft rotated at 12,000 rpm, achieving a peripheral speed of 1256 in/s [].

4.1. Comparison of Seal Types

Seals are divided into static and dynamic groups (Figure 12); the primary sealing surfaces in the former have little relative motion (e.g. gasket) while those of the latter have substantial relative sliding motion. The dynamic seals can be further divided into reciprocating seals for pistons and rotating seals for rotating shafts. The TAP seals belong to this latest category. This category is further divided into interfacial and interstitial seals. The interfacial seals include rubbing contact seals and controlled clearance seals: soft shaft packings. lip seals, circumferential shaft seals, and face seals belong to this group. The interstitial seals include fixed positive clearance seals such as labyrinth seals, bushing seals, viscoseals, and ferrofluidic seals [18].

Though appropriate for sealing high pressures, the interfacial seals, when compared to interstitial seals, have the disadvantages of lack of dependable analysis, strict geometric and surface requirements, the need for lubrication, limited seal life, and complexity of design. Since the rubbing contact of sealing faces occur at the microscopic level, it has been virtually impossible to accurately analyze such behavior. This problem of unpredictability is worsened by imperfect sealing surface conditions, eccentricities, and vibrations of the shaft, all of which may cause excessive rubbing. To reduce such undesirable effects, the interfacial seals require strict control over shaft's eccentricity, and surface conditions such as hardness and smoothness. Good lubrication is necessary to 1)remove heat generated from rubbing and 2)for the film to tighten the seal. However, even with good lubrication, friction and wear (adhesion, abrasion, corrosion, surface fatigue) destroy the surface

topography of the rubbing interface areas. Thus, the seal's performance and life expectancy are limited. Another risk of wear is contamination of the working fluid by fine wear debris. The high rotational speeds in the TAP worsens the above phenomenon. As more heat is generated, the temperature is increased with the consequent reduction in the lubricant's viscosity; the result is thinner film and more friction and wear. Lastly, the seal systems, consisting of multiple seal faces and rings are complex relative to interstitial seals and the increased complexity has negative effects on reliability, and maintainability.

Thus, for sealing at low to medium pressures, as in TAP conditions, interstitial seals are appropriate because of their simplicity, durability, reliability, and lack of maintenance requirement. Interstitial seals act by creating pressure drop in the liquid to be sealed in its clearance without affecting the rotation motion of the shaft. The pressure drop is achieved through throttling processes or by exerting external forces. Lack of rubbing significantly reduces the problems of friction and wear and extends the seal life indefinitely.

A labyrinth seal contains a series of chambers which incur irreversible acceleration/deceleration in the sealant fluid and causes its entropy rise, resulting in pressure drop. A bushing seal throttles by causing frictional losses along a small annular gap of constant cross-section. Various versions of both seals exist but they share one disadvantage of relatively high leakage rate per unit length; finite leakage is a requirement for effective throttling.

A viscoseal uses grooves on either housing and/or shaft to pump the sealant liquid, with zero net flow, by creating shear stresses in the sealant fluid to pump it back toward the high pressure region (Figure 13). Effective sealing is a function of groove parameters, viscosity of the sealant fluid, clearance, shaft speed, and eccentricity. Since shear stresses are viscosity-dependent, removal of heat is crucial to effective sealing and requires most of viscoseal's maintenance. Its main advantage, however, is that its pumping ability gives it potentital for very low leakage rates (comparable to contact seals) while avoiding rubbing contact. Furthermore, it can easily be used in tandem with other types of seals.

Ferrofluidic seal was first developed in the 1960's by NASA for zero-gravity operation and, since then, has gained ever-increasing industrial acceptance. It is the only interstitital seal which promises zero leakage. The clearance is hermetically sealed with film of a ferrofluid held stationary by ring magnets (Figure 14). A ferrofluid is a collodial suspension of submicron size magnetic particles in various carrier fluids. It behaves like any homogeneous carrier fluid except in magnetic fields (Figure 15). The ferrofluid seals' advantages are no shaft surface requirement; no limits on rotational speeds; no need for ultra-small clearances; more tolerance of shaft eccentricities and runout than other seals; no measurable friction or wear; indefinite life expectancy; no

22

limits on shaft size; and suitability for sealing gases against vacuum conditions. The disadvantages are the temperature limitation (< 373 K); the need for immiscibility between the ferrofluid and the working fluid: and inability to seal liquids.

There are various kinds of ferrofluids. Mercury itself has been successfully made into a ferrofluid by adding metallic sodium to mercury containing tin-coated iron particles. However, if ferrofluidic seals were to be used, it would be more sensible to use a ferrofluid inert with mercury such as fluorocarbon since the binary cycle uses mercury in both vapor and liquid phases at temperatures above 373 K [19].

4.2. SNAP-8 Seal-to-Space Design

SNAP-8 was a 35-kWe nuclear, turboelectric EPS which contained four independent loops. Sodium poptassium was heated by a nuclear reactor in the first loop, and via heat exchanger. heated mercury in the second loop. Expansion of mercury vapor drove the TAP: after the expansion, mercury was condensed and pumped back to the boiler. A second loop of sodium potassium transferred waste heat from the mercury loop to the radiator. Finally, a fourth loop contained polyphenyl ether. used for bearing lubrication and cooling of the alternator, electric motors, and controls. The decision to use oil lubrication was a conscious effort by NASA for ruggedness, reliability, and long life. Thus, the need arose not only to contain the fluids. but also to keep them from intermixing.

The SNAP-8 turbine was actually overhung at one end of the shaft. The turbine bearings were located between the turbine and the alternator while the alternator bearings were placed inside the alternator. The thrust load was balanced by a piston. driven by mercury from the turbine outlet, located at the turbine end of the shaft. The space seal was place between the bearing closest to the turbine and the turbine itself [20].

The space seal system consisted of a cooler.a visco-pump, a slinger. and molecular pump on the mercury side; and a slinger with a molecular pump on the alternator side (Figure 16). Each end also had a mechanical carbon face seal, for start-up and shut-down conditions. which were lifted off at steady-state operation. The cooler condensed mercury vapor at turbine's exit and visco-pump created an axial pressure gradient which pushed the condensate toward the slinger and prevented it from centrifuging back into the turbine wheel housing (Figure 13). Slinger pump, consisting of a step in the shaft. created a liquid-vapor (L-V) interface by centrifuging the condensate away from the shaft center. thus effectively sealing mercury. The vapor which evaporated from the L-V interface was pumped back to the L-V interface by the molecular pump. Same principles sealed polyphenyl ether on the alternator side. The little leakage from both ends were vented out to

space. The face seals were needed because the above three seals were effective only at steady-state rotation. or high rpm.

The slinger's "sputtering" problem, in which liquid droplets migrate toward the shaft center at high rpm due to the momentum force being greater than the surface tension force, was overcome by making the molecular pump's radial clearance smaller than the droplets' average diameter - 0.005 in compared to 0.01 ~0.025 in. Furthermore, the tendency of mercury film on the static wall to persist the L-V interface was overcome by coating the surface with Teflon to improve unwettability.

A prototype was ground-tested for 10,828 hours including 37 starts and was judged to be in good condition, capable of further operation. During the testing, the L-V interface was maintained at under 250 F and the leakage remained under 1 lb/yr rate. The viscoseal breakdown which results in gross leakage was not encountered during the operating conditions [21].

Upon post-test inspection, following conditions were observed. The viscoseal suffered minor cavitation damage; however, neither the structural integrity nor the sealing capability was affected. Other minor cavitation damage were visible at slinger/molecular pump juncture, a sign of weaker than design pumping ability of visco-slinger pump, and on the molecular pump itself due to temporary higher than normal turbine exit pressure. As for the alternator seals, inboard seal at the drive end and outboard seals at the anti-drive end showed brown/black deposits (Teflon). The bearings were in good condition, consistent with 10,828 hours of wear. The face seal on the turbine was severely worn, a result of leaked mercury liquid causing high axial load and wear on the face.

4.3. New Sealing Options

The next four designs show potential for application to binary cycle with their simplicity in design and low leakage rates. The first is an electromagnetic seal; the second is a ferrofluidic seal; the third is a viscoseal; and the fourth is a combination of the latter two.

The first design is an electromagnetically spun mercury seal patented by McHugh [22]. It is a combination slinger with an electromagnetic seal for low rpm sealing. A pair of magnets create an axial magnetic field while electric current is applied radially through mercury in an annulus. By Ampere's and Fleming's rules, a tangential force acts on mercury in the annulus causing it to spin around the shaft and form an effective seal. Unfortunately, no experimental data is available on the seal's performance. One disadvantage of this system is that its need for current and use of a slinger, which has higher power consumption than viscoseals, and its need for electric current increases power loss while decreasing the power output.

The second design was initially developed at Hitachi [23]. This is a combination of a slinger with a ferrofluidic seal. It has an advantage over other ferrofluidic seals in its tolerance for large radial vibration amplitudes which is desirable for off-design conditions. At high rpm, centrifugal forces keep the ferrofluid stationary, comparable to L-V interface in a slinger, while at low rpm or static conditions, the magnetic field dominates the sealing function. Despite its advantage of zero leakage, the ferrofluidic seal alone cannot yet be used to seal mercury for the following reasons. First, current ferrofluids evaporate rapidly and chemically breakdown at temperatures above 373 K. Second, the ferrofluidic seals can only seal gases at present because the ferrofluid/liquid interface becomes unstable at high shaft speeds.

The third design, shown in Figure 17, offers static sealing capability by allowing some axial movement of the viscoseal ring, eliminating an auxilary system of static seals. The step in the shaft acts as a slinger, centrifuging sealant liquid at high rpm. As rpm decreases, pressure in cavity C of the slinger decreases while vapor pressure at A remains constant. Thus, the viscoseal ring moves axially until faces D and F form a static gasket-like seal. An elastomeric ring, shown as dark circles, facilitates the axial movement of the viscoseal ring relative to the shaft. Reports indicate successful shutoff-no gas leakage-at 300 psia vapor pressure and room temperature [18].

The fourth design has not been experimentally tested but shows the most potential for zero leakage sealing without high power loss (Figure 18). Toluene can be used to condense and cool mercury vapor at the turbine-end; a viscoseal would form mercury liquid-vapor interface. As in SNAP-8, the herringbone grooves on the shaft prevent axial movement of the interface. Furthermore, with sufficient toluene massflow, the temperature of mercury liquid-vapor interface can be maintained at below 373 K. Same devices can be used on the bearing side. The low pressure vapor which escape from either end can be sealed and kept separate by a ferrofluidic seal. As the shaft is unlikely to experience any large amplitude radial vibrations, a regular ferrofluidic seal without a slinger should be sufficient. Injection/eduction of nitrogen at pressure above that of mercury at the turbine outlet can be added between the ferrofluidic and viscoseals as a redundant safety mechanism. Thus, the ferrofluidic seal acts as a nitrogen gas seal and mercury and lubricant vapors are prevented from direct contact with the ferrofluidic seal at all times, including startup and shutdown phases. Figure 19 shows the bearing/seal configuration for TAP.

4.4. Conclusion

The fourth design is recommended. The system is simple in design which improves its reliability and serviceability. Also, it has static sealing capability. Above all, it seals with zero leakage.

Chapter 5

Radiator

The radiator/condenser removes heat from toluene and rejects it to space. The low rejection temperature of the binary cycle makes it one of the two most massive components in the EPS. Therefore, the radiator mass reduction will have a significant effect on the mass of the whole EPS. This chapter contains a review of previous work and presents a preliminary design of a rotating film radiator concept (RFR) and rotating bubble membrane radiator (RBMR).

5.1. Concepts

The promising space radiator concepts which have been proposed are liquid droplet radiator (LDR), Curie point radiator (CPR), moving belt radiator (MBR), heat pump radiator (HPR), rotating bubble membrane raditor (RBMR), and rotating film radiator (RFR). The first five concepts have been evaluated by Begg [24]. The last one was mentioned by Feig [25], but no follow-up work was done. High reliability, low developmental risk, meteorite damage resistance, and light weight are the main desirable characteristics.

In RFR, heat is rejected from toluene to the low vapor-pressure radiator fluid (e.g. silicone oil) in a condenser heat exchanger. The fluid will be pumped to a nozzle on a disk which is rotated by a rotating platform. Rotating vapor seals such as the ones duscussed in Chapter 4 will be used to contain the fluid in the rotating platform. Upon ejection from a nozzle at the center on one side of the disk, some of the radiator fluid will be bled off onto the opposite side via slanted holes. The fluid then spreads into thin films, one on each side. As the centrifugal force accelerates the film radially outward, the film radiates heat directly to space. The disk's rotational speed controls the film thickness and velocity. Return piping at the disk edge returns the radiator fluid (Figure 20).

The HPR is the most developed of the six concepts. The heat pipe, with no moving parts, is a proven technology; therefore, it offers high reliability and little developmental risk. Although they lack the technical maturity of HPR, both RBMR and RFR do not require new technical development. Both rotating machinery and shaft vapor seals-to-space, the two key technical issues, have accumulated thousands of successful test

hours on earth. On the other hand, the LDR, CPR, and MBR require non-existent technologies. LDR requires a droplet generator/collector combination with a high degree of aiming accuracy. CPR requires a collector with a magnetic field generator and an effective heat exchanger to transfer heat to the solid particles from the working fluid. MBR requires seals which would wipe off the working fluid without leakage or damage to the belt as the belt exits the heat exchanger. All three components pose technical challenges, and, if built, would require much testing to prove their reliability.

In meteorite resistance, the LDR and CPR are better than RFR and HPR which, in turn, are better than MBR and RMR. Meteorites flying through the droplet sheet of LDR would cause only temporary flow disturbance along with some fluid loss; however, the overall performace would remain the same. CPR will have higher solid particle loss since the solid particles are more prone to be deflected upon collision with meteorites; however, the particles can be replenished to restore design performance. Punctures in either one of many (compartmentalized) HPR pipes or the rotating disk of RFR will cause performance degradation since the affected part can no longer aid in heat rejection. However, the isolation of damage minimizes the risk of a catastrophic failure. Conversely, punctures in the RBMR container or the MBR belt would cause rapid working fluid loss and a catastrophic failure.

In mass, HPR is the heaviest of all; its specific reported specific weights are greater than 10kg/kWt [26]. Relatively, the HPR and CPR show potential for an order of magnitude mass reduction while RBMR, RFR and MBR show potential for mass reductions greater than 50%.

After overall comparison, RBMR and RFR were chosen for preliminary design and comparison. Two assumptions common to both designs were as follows. First, aluminum was assumed to be the material for both components. Aluminum is attractive because it offers low cost; high strength; good corrosion resistance; good resistance against oil and many chemicals; low mass; high emissivity (0.8 for anodized aluminum); and high thermal conductivity (237 W/m K) [27]. Second, the temperature of space environment was assumed to be 250 K.

5.2. Rotating Membrane Radiator Design

A cylindrical container with low height rotating about the center axis of each circular side was assumed (Figure 21). For greater than 99% reliability against meteorite puncture, the container thickness of 0.001 m (1 mm) was also assumed [28]. The superheated toluene vapor is sprayed into the container from the center and is cooled in the central region of the disk before being condensed in the peripheral region as shown in Figure 21.

In the cooling section following equations were used to find heat transfer coefficient h. At radius r. given half-height of the disk 1 and angular velocity ω,

$$D = 2\pi r l/(\pi r + l) \tag{4.2.1}$$

$$G = m_{toluene}/(4\pi r l) \tag{4.2.2}$$

$$Re = GD/\mu \tag{4.2.3}$$

$$Nu = 7.54 \quad for\ Re\ <\ 10000 \tag{4.2.4}$$

$$Nu = 0.332 Pr^{1/3}\sqrt{Re} \quad for\ Re\ >\ 10000 \tag{4.2.5}$$

For the condensing section, a film condensation with zero shear at the vapor liquid interface was assumed. The implicit assumption in the use of this model is wetting of aluminum surface by toluene. Sparrow and Gregg [29,30] showed that the interfacial shear has little effect on analytical heat transfer prediction. Furthermore, either the existence of interfacial shear or the lack of wetting (drop-wise condensation) will promote heat transfer. Therefore, film condensation model provides a conservative estimate on the RBMR mass. For design purposes, the condensation model choice is not critical because simple calculations show that $q"_o$, heat flux on the radiating side, can not exceed $\epsilon\sigma(T^4_{sat} - T^4_{space})$, or 503 W/m^2. This means that the radiating side will determine the RBMR size.

Sparrow and Gregg developed correlations for h and condensate film height δ for film condensation on a rotating disk [29]. However, the correlations assumed a constant T_w, an unknown in RBMR. Therefore. analysis shown in Appendix A was done. instead. In the analysis. vertical velocity V_z. shear stress at interface τ_g, and vapor density ρ_g of toluene were ignored. For each container wall segment. either a incremental temperature or quality drop was assumed. Integrating the τ_{rz} equation for V_r and condensate film height δ led to the heat transfer coefficient $h = k/\delta$ on the inner surface of the container wall segment. Assuming that the inner and outer surface temperatures are the same (a reasonable assumption due to high thermal conductivity and thinness of the aluminum container wall). the heat balance equation was solved for the segment's wall temperature, T_w, via Newton-Raphson method. With the q" known. the amount of heat rejected by the segment. dQ, was calculated which then led to calculation of required area. dA. which. in turn. gave the outer radius required. The calculations were stopped when the quality, x. reached 0.

As Figure 22 shows. the RBMR's mass reaches its limiting value at relatively low rotational speed of 100

rpm because the condensate layer thickness reaches its limiting value at that rotational speed. The low angular velocity is favorable because it means low power expenditure. Figures 23 and 24 show condensate layer thickness, and T_w as functions of r. It is clear that very thin film of about 20 micrometers can achieved at low rpm due to the low toluene mass flow rate. Furthermore, it is interesting to note that the wall temperature and film height remain constant. This trend is in agreement with Sparrow and Gregg's model which suggests a constant condensate layer for an assumed constant T_w. The RBMR's specific masses are 5.4 kg/kWt or 5.72 kg/m^2.

5.3. Rotating Film Radiator Design

A silicone oil such as diffusion pump oil (e.g.Dow Corning 705) was chosen as the radiator fluid for its high emissivity (0.8) and low vapor pressure (10^{-9}torr) [31]. High emissivity reduces the required surface area and low vapor pressure minimizes evaporative fluid loss. Assuming a 50 m^2 radiating area and using a Langmuir equation for evaporation into vacuum [4],

$$m_{loss} = P_{vap}\sqrt{\frac{MW}{2\pi kT}}\ A$$ (4.3.1)

```
where MW = molecular weight
      P_vap = vapor pressure
      k= Boltzmann's constant
      T = absolute temperature of space
      A = area
```

The cumulative evaporation loss over a ten-year period turns out to be less than 0.3 kg. This is actually an over-estimate because the model assumes zero concentration of oil vapor in space near the radiating surface. Thus, evaporative loss is not an issue in RFR if silicone oil is used.

In the RFR, thickness of 0.0005 m (0.5 mm) was assumed for both the disk and the heat exchanger. Although large, the disk only needs to be thick enough to withstand the centrifugal stress due to rotation. Simple calculation showed that 0.5 mm is sufficiently thick for structural reasons and also offers 99 % reliability of no-puncture over a 10-year-cycle. Also the 0.5 mm thickness assures over 99 % reliability of no-puncture for the heat exchanger which is much smaller than the disk. Furthermore, rotational speed of 100 rpm was assumed.

The disk sizing was done as follows. The variables were maximum and minimum oil temperatures. For a given pair of end temperatures, the oil mass flow rate, m_{oil}, was determined. The disk size was increased by adding rings of 0.01 m width (dr); this procedure is equivalent to increasing the disk area by increasing the radius by 0.01 m increment. For each ring element, the Reynolds number, Re, and the film height, δ, were

calculated to check for turbulence in the flow. Kirkpatrick showed that the rotating film flow remains laminar for Re below 1000 [32].

$$Re(r) = \frac{2m_{oil}}{(\pi\mu r)}$$ (4.3.2)

$$\delta(r) = 0.909 \frac{Re^{1/3}}{(r\omega^2/v^2)^{1/3}}$$ (4.3.3)

Then, wave on-set Reynolds number, Re_{wave}, was calculated to check whether waves occur; waves would occur if the Re falls below the Re_{wave}. Thus, the four possible flow regimes are wavy turbulent, non-wavy turbulent, wavy laminar, and non-wavy laminar.

$$Re_{wave} = 1.62 \left(\frac{\sigma^3 \rho}{\mu^4 \omega^2 r}\right)^{0.125}$$ (4.3.4)

Then the critical mass flow rate, $m_{critical}$, was calculated to check if the mass flow rate is sufficient to overcome the surface tension and maintain the film flow . For mass flow rates below the critical value, the film would break up into rivulets.

$$m_{critical} = 0.806 \sigma^{0.6} \left(\frac{\mu\rho}{r\omega^2}\right)^{0.2}$$ (4.3.5)

σ = surface tension

Then, the energy balance equation,(Equation 4.3.6), for each segment was solved for the film temperature T_i by the Newton-Raphson method which then determined the amount of heat rejected for each segment [1].

$$\frac{m_{oil}C_p(T_i-T_{i+1})}{2} = \frac{2\pi r\delta(r)k(2T_i-T_{i+1}-T_{i-1})}{dr} + dr2\pi r\epsilon\sigma(T^4_i-T^4_{space})$$ (4.3.6)

The procedure was repeated until the film temperature reached the specified minimum oil temperature.

Above routine was combined with an LMTD-method heat exchanger design routine which calculated the heat exchanger length and mass [33]. Due to the poor heat transfer properties and low flow rates of both toluene and the oil, a plate-fin structure, which has high Nusselt number, Nu, for small hydraulic diameters, was assumed (Figure 25). The input variables were the width of each oil flow section (dx), the fin length (lfin), and number of oil flow sections (NOT). The height of oil flow sections was assumed to be twice the fin length. The toluene side resistance was neglected because the radiating side controls the overall heat transfer rate which means that the oil side controls the heat transfer rate in the heat exchanger.

Initiallly, the two routines were combined to determine the optimum operating temperature range where the overall mass, including those of the heat exchanger, the disk, and the oil, is minimized. For a given maximum oil temperature, the minimum oil temperatures were swept down from the maximum temperature until either the minimum temperature reached 250 K or the oil mass flow rate fell below the critical mass flowrate; then, the minimum oil temperature where the overall mass is minimized was chosen for each maximum oil temperature . As expected, the optimum temperature was not dependent on the type of heat exchanger chosen; for any set of heat exchanger parameters, the overall mass is minimized at maximum temperature of 348 K and minimum temperature of 301 K. For dx = 0.001 m, lfin = 0.007 m, and NOT = 500, the mass breakdown is as follows.

T_{max}	T_{min}	Heat Exchanger	Oil	Disk	Total
349 K	311 K	11.143 kg	142.508 kg	79.576 kg	233.227 kg
348 K	301 K	7.866 kg	131.329 kg	89.420 kg	228.615 kg*
347 K	301 K	7.018 kg	131.759 kg	90.201 kg	228.978 kg

After the operating temperature range determination, a segment-by-segment heat exchanger design was done to check the LMTD design value and to optimize the heat exchanger mass. Input parameters included the ones used in the LMTD routine plus the height of toluene condensing section, l. The toluene condensing section width was determined by NOT, dx, and the assumed fin thickness of 0.0005 m. The homogeneous condensation model [34] was used for the toluene condensation in the energy design for three reasons. First, the choice of toluene condensation model is not a factor in the heat exchanger design because the oil side resistance is O(-2) while condensation model applied to toluene yields resistance of O(-3) or smaller. Second, there is lack of experimental data of toluene in forced convective condensation. Third, the homogeneous model has been known to give reasonable heat transfer and pressure drop predictions for forced convective condensers [2]. The toluene heat transfer coefficient was limited to a maximum value of $50000W/m^2K$ and the minimum toluene exit pressure requirement was 34000 Pa. For each dx, l, and NOT, lfin values were varied until an optimum lfin which met exit pressure requirement was found. The optimum for each NOT, along with overall heat exchanger dimensions, are as shown below. For dx = 0.001 m and l = 0.001 m.

NOT	lfin	height	width	length	mass
500	0.004 m	0.012 m	.75 m	.90 m	8.528 kg
400	0.004 m	0.012 m	0.60 m	1.12 m	8.463 kg*
300	0.0055 m	0.015 m	0.45 m	1.25 m	8.65 kg

Thus, for the assumed reference conditions, the heat exchanger mass is optimized at NOT of 400. The exit toluene pressure requirement was not a constraint in mass optimization for NOT of either 500, or 400; however, the exit pressure requirement did constrain the optimization for NOT of 300.

Figures 26 ~ 28 show respectively the height, temperature, and Re of film as functions of radius for the reference RFR. Figure 26 shows that, even for low rotational velocity, the film becomes thin (< 0.001 m) at short radius of 0.45 m.This is advantageous because a thin film can be established with low power expenditure. Figure 27 shows that most of heat rejection occurs in the outer region of the disk as shown by the increasing temperature profile steepness. Figure 28 shows that the film flow remains laminar. Furthermore, as Table 2 shows, the film is wavy in the region inside the radius of 0.63 m, but non-wavy at radii greater than 0.63 m. This is encouraging because film is absolutely steady throughout most of its flow. However, one point needs experimental validation. That the program checked for $m_{critical}$ at each radius and found the m_{oil} to be sufficient to overcome surface tension suggests that rivulets are unlikely to develop. However, Espig's results show that rotating film flow splits into rivulets for Re below 10 [35]. One credible method of validation would be to run rotating film flow and heat transfer experiments on one of the Shuttle missions.

RFR's mass is insensitive to rotational speed for two reasons. First, for each ring element of film, the low thermal conductivity and the low height of oil film make the amount of conductive heat transfer to and from each ring element negligible compared to the amount of radiative heat transfer from the ring element to space. Second, the film height does not decrease significantly at rotational speeds above 100 rpm.

Combining the optimized heat exchanger mass with that of oil and disk, the RFR yields specific masses of 5.59 kg/kWt or 3.52 kg/m^2.

5.4. Conclusion

In specific mass, both RBMR and RFR compare favorably to HPR whose most recent specific mass is about 10 kg/kWt. To verify the correlations used in the design, rotating disk flow and toluene condensation experiments should be carried out in space environment.

Chapter 6

Receiver

The receiver's high mass and weak technological base makes it a weak link in the whole system. Therefore, the design and development of an efficient and reliable receiver deserves the utmost attention. This chapter compares eight receiver concepts and recommends a receiver concept utilizing liquid lithium as TES; the recommendation is based on the concept's light weight and simplicity.

6.1. Concepts

Following is a brief description of each concept. The schematic of each concept is shown in Figure 29 and the energy flow diagrams for each orbit is shown in Figure 30. The first is a heat pipe design pursued by Sundstrand. During insolation, both mercury vaporizing and the lithium fluoride (LiF) TES charging are done in the axial heat pipes in the receiver. During the eclipse, the axial heat pipes transfer energy from the freezing LiF to the vaporizing mercury. The circumferential heat pipes even out any non-uniform heat flux distribution, which could occur due to tracking error, by transferring energy away from the hot spots [36].

The second concept divides the receiver into two regions of relatively high and low heat flux regions. During insolation, the LiF TES charging and mercury superheating are done in the low flux region while mercury preheating and low-quality vaporization are done in the high flux region. During the eclipse, the valves will direct the mercury flow to only the part of the receiver where the LiF TES is located. The preliminary design of this receiver was done by Fox [36].

The third concept has the LiF TES separated from the receiver. During the insolation, only the mercury vaporization with excess superheat is done in the receiver, and the LiF TES is charged by the excess superheat of the mercury [37]. During the eclipse, the valves will direct the mercury only to the LiF container, bypassing the the receiver altogether.

The fourth concept has mercury vaporization and LiF TES charging done together in the receiver: the TES is contained in bellows wrapped around the mercury vaporizer pipes. This concept is similar to the first

concept in that the mercury flow remains constant during both insolation and eclipse; however. the heat pipes are not used. This concept was pursued by NASA Lewis and MIT [38, 39].

Next three concepts use 'slush', which consists of immiscible LiF/Li melts, as the TES. The slush is liquefied during the insolation and thickened during the eclipse as the LiF freezes. Fifth concept has both mercury vaporization and slush melting done in the receiver during the insolation. During the eclipse, the valves direct both fluids away from the receiver to a heat exchanger (e.g. concetric counterflow type) where the thickening slush vaporizes mercury. A little but constant slush flow through the receiver is necessary during the eclipse to prevent freezing of lithium (melting point at 452 K) or LiF (1121 K). either of which could plug up the plumbing.

The sixth concept is similar to the fifth except that mercury will be vaporized in the heat exchanger during both insolation and eclipse. Therefore, only the slush is liquefied in the receiver during insolation.

Seventh concept has only the lithium of the slush pumped; only the lithium is heated in the receiver during insolation. The heated lithium, by entering the cylindrical TES container at the outermost radius melts the frozen LiF on the wall and causes the slush to rotate in the container. The rotation centrifuges out the frozen LiF, whose density is about three times that of lithium, and minimizes the concentration of frozen LiF in the center of the cylindrical container where the charged slush is kept. Simultaneously, the melted slush is pumped from the center of the cylindrical container to the heat exchanger where mercury is vaporized. The thickened slush, upon exiting heat exchanger, also enters the container at the outermost radius of the cylindrical container. centrifuging out the frozen LiF. During the insolation, the LiF flow through the receiver is greater than the lithium flow through the heat exchanger by a factor of (1+(35/59)) so that, at the end of eclipse. during which the lithium flow through the receiver is close to nil. all of the LiF is solidified onto the container wall.

The eighth concept utilizes only lithium as the TES. During the insolation. lithium is heated in the receiver. Some of the heated lithium is stored in a cylindrical container with a movable thermal barrier separating the relatively cold lithium from the hot lithium. The rest of the heated lithium is used to vaporize mercury in the heat exchanger. During the eclipse, lithium flow to the receiver decreases to a minimum (sufficient to prevent freezing) and the stored hot lithium will vaporize mercury: at the end of the eclipse. the accumulated cold lithium will occupy most of the cyldrical storage tank at which time the insolation will begin and the lithium flow through the receiver resumes.

6.2. Thermal Energy Storage Selection

Many forms of TES exist, including chemical batteries, and phase chagne materials (PCM) such as LiF. PCM's are particularly attractive for the high energy storage density due to the high heat of fusion and the availability of this heat at a constant temperature. The properties desired in the PCM are as follows [40].

property	desired	influence
melting temperature	> peak cycle temperature	cycle efficiency
heat of fusion	high	storage mass
thermal conductivity	high	charging/discharging rate
heat capacity	high	reserve capacity
density	high	storage volume
thermal expansion	low	container volume change
volume change on fusion	low	container volume change
viscosity	low	heat transfer
vapor pressure	low	chemical stability
corrosion	none/low	performance, reliability
long-term stability	high	performance, reliability

The PCM's can be divided into salt and metallic groups. The heats of fusion for the two groups are comparable. However, the higher thermal conductivities and densitites of the metallic PCM's make them more attractive for heat transfer purposes. Nevertheless, the metallic PCM's react with metals at high temperatures, and, therefore, containment of metallic PCM's is an unresolved technical issue. Ceramic is a possible containment material, but experimental data is lacking in that area [41]. Therefore, the salt PCM's, most of which can be contained by Ni or Nb based alloys, were selected for this design. Table 3 lists some of the salt PCM's with melting points above 1033 K; LiF surpasses the other candidates as the most effective PCM (Figure 31) with its high heat of fusion.

Since the LiF was chosen as the PCM, LiF/Li was the logical choice for slush. The assumption that all of the enregy storage would still occur in the form of LiF phase transition with the conductive lithium acting as the energy transfer agent led to the conclusion that the LiF/Li slush system would be the most mass-efficient one.

Lithium was chosen over other liquid/transition metals for three reasons: the specific heat, the melting temperature, and the boiling temperature. The two temperatures have to have a range greater than that between 654 K and 1033 K (the low and high temperatures in the mercury cycle of the binary cycle) to ensure that the metal stays liquid at all times. High specific heat is desirable to reduce mass for storing a certain amount of energy for a given ΔT. As a secondary factor, high density is desirable to reduce volume of storage for a given mass, thus decreasing the container mass. Of all the metals only lithium and sodium have the appropriate melting/boiling points. Of the two, despite its lower density, Li was chosen because of its specific heat almost three times that Na (Table 4) [42].

6.3. Receiver Material Selection

The need to contain corrosive liquid metals such as lithium and mercury at elevated temperatures (1100 ~ 2000 K) under high pressure (0.1 ~ 5.0 MPa) require following properties in the candidate receiver material [40].

parameter	desired	influence
melting point	high	structural rigidity
thermal conductivity	high	receiver size
density	low	receiver mass
modulus of elasticity	high	stiffness
ultimate tensile strength	high	structural rigidity
yield strength	high	structural rigidity
creep strength	high	structural rigidity
fatigue strength	high	structural rigidity
fracture toughness	high	meteorite damage
oxidation/corrosion resistance	high	structural rigidity
fabricability	high	manufacturing ease

Due to the high temperatures involved, refractory metals, including tungsten (Tu), molybdenum (Mo), tantalum (Ta), niobium (Nb), thorium (Th), and titanium (Ti) were considered. In the following comparisons, a reference temperature of 1100 K was assumed. The relatively low melting points of Ti (1953 K) and Th (2023 K) excluded them from further consideration. Furthermore, despite its high melting point (3660 K) and high thermal conductivity (137 W/m K), Tu was rejected for its high density (19300 kg/m^3). Property comparisons of remaining Mo, Nb, and Ta can be seen in Table 5.

Ta was rejected because of its combination of high density and low thermal conductivity which would result in a heavier and bigger receiver than one made of either Mo or Nb. However, its outstanding heat and structural properties would make it a good alternate material.

Nb is the second best choice, if the hoop stress in plumbing could be kept below 20 MPa. Its low creep strength is its biggest weakness. However, its low density and high thermal conductivity combined with very good resistance against liquid metals make Nb an attractive choice. A particularly good Nb alloy for handling liquid metals is Nb-1Zr which combines good strength with excellent fabricability: the Zr additions results in resistance against lithium, sodium, and potassium corrosion upto 1283 K.

Mo was chosen as the receiver material for its good strength, especially at elevated temperatures (Figure 32): high thermal conductivitiy: high stiffness: good retention of mechanical properties after thermal cycling: low coefficient of expansion; and, above all, good resistance against Li and Hg - less than 1 mil/yr corrosion against Li at 1173 K. A Mo alloy with TZM has shown outstanding high temperature properties with higher creep and tensile strength than pure Mo. Also Mo-30W is especially resistant against liquid metals [27].

6.4. Comparison of Concepts

Thermal stress minimization is important for material's prolonged service. Concepts one, four and five will be practically isothermal receivers around either the melting point of heat pipe fluid (concept one) or 1121 K, the melting temperature of LiF (concepts four and five). Such constant temperature makes thermal stress along the receiver depth negligible. On the other hand, concepts two, three, six, seven, and eight would have thermal stresses along the depth of receiver as the coolant (mercury or lithium) temperature increases along the receiver length. As for radial thermal stress across the heat transfer surface, the combination of Mo's high thermal conductivity and the thinness (< 0.001 m) of heat transfer surfaces would make them negligible.

The non-uniform heat flux distribution tolerance is crucial to creep prevention and reliable performance of the receiver throughout its service life. Mirror imperfections (slope errors and shadowing factors), tracking errors, and void formation (between LiF and container) can cause non-uniform heat flux distribution. The non-uniformity, if not evened out, will not only cause uneven mercury vaporization/TES charging but also cause hot spots, which, in turn, will increase thermal stresses, fatigue, corrosion, and creep. Concept one has the most tolerance due to its use of heat pipes. Concept eight could be just as tolerant: lithium's high thermal conductivity and heat transfer coefficient can effectively transfer energy from the high energy region. Concepts three, five, six, and seven will be less tolerant than eight due to the relatively low thermal conductivity of the LiF/Li slush. However, that the above concepts use combined convective/conductive heat transfer (avoiding void formation) and that the slush and lithium are more conductive than LiF alone make them more tolerant than concepts two and four whose stationary LiF TES leaves them vulnerable to void formation and unable to handle any non-uniformity.

The TES containment is important to prevent TES container rupture. One major problem of LiF TES is the 35% volume change of LiF upon phase transition. Such contraction can create voids between LiF and the container, creating hot spots. The low thermal conductivity of LiF was mentioned above. Another problem is that of thermal ratcheting, in which cyclic freezing/thawing causes trapped expansion of LiF which leads to container rupture. Bellows which could be used in concepts one through five have been tested on earth as a means to compartmentalize LiF and minimize void formation but their performance in zero-gravity environment is unknown at best. The lithium TES of concept eight offers many advantages when compared to both the LiF and slush TES. First, the volume change of Li upon phase transition is a mere 1.5 %. Also the density change of lithium between 668 K and 1125 K is 11%. The volume change can be addressed by attaching an accumulator. Advantages of lithium TES to the slush TES include elimination of the risk of unexpected plugging of plumbing by the freezing LiF, and the better stability of homogeneous lithium over that

of heterogeneous slush. Nevertheless, concepts five through seven are advantageous over the first four concepts because, even though LiF is a part of the TES, the slush form of the TES allows pumping and the use of an accumulator.

The mode of heat transfer is important in determining the effectiveness and the speed of TES charging/discharging. Concepts one through four depend on conduction through liquid and solid LiF, both of which are relatively non-conductive ($k_{liquid\ LiF}$ = 2.5 W/m K, $k_{solid\ LiF}$ = 7.5 W/m K). Concepts five through seven depend on convection through the liquid melts and conduction through solid LiF. Concepts eight depends solely on convection through lithium. Concept five through seven are more effective than the first four because the slush would prevent formation of solid LiF layers on heat transfer surfaces during TES discharge: the solid formation degrades heat transfer performance due to low thermal conductivity of solid LiF. Furthermore, convection through LiF/Li slush, which is more conductive than the liquid LiF, has less resistance than conduction through liquid LiF. Concept eight is advantageous over concepts five through seven. First, it eliminates conduction through LiF which is the slower part of the two part process. Second, lithium's thermal conductivity, higher than that of LiF/Li slush, allows faster charging and discharging of the TES.

Simplicity is another important criterion, and the eighth concept is the simplest and probably the most reliable of all the concepts considered. Centrifuging out the liquid LiF from the LiF/Li liquid mix (concept seven), controlling the LiF volume change (concepts one through five), preventing the slush from freezing (concpet six) all require extra but necessary equipment such as a centrifuge motor, valves, and bellows. The eighth concept circumvents above problems by using simple reliable components such as a container, a pump, and a heat exchanger.

Above all, however, mass is the single most important criterion for both concept evaluation and optimization because it has the strongest effect on the initial launch and the on-orbit maintenance cost [2]. Fox and Lurio [36, 38] showed that the TES and the collector mirror are the most massive components in the collector-receiver assembly. The receiver itself and insulation accounted for 14 kg compared to 100 kg of TES in Fox's design. Calculations show that very light TES mass is possible for the eighth concept: for example, for a ΔT of 500 K, 70.5 kg of lithium is needed for TES compared to 141 kg of LiF needed for the first seven concepts. Assuming that the combined mass of heat exchagner, container, and pump is less than the 70.5 kg difference, eighth concept will be lightest system. The second lightest group of receivers include those of concept three and four. Concept three's extra mass is due to the need for valves and concept four's extra mass is due to the need for aperture door which would prevent aperture loss during the eclipse: it is assumed that the masses of valves and the aperture door are comparable. Concept two would be heavier than either one of

concepts three and four because concept two requires both the valves and the aperture door. Concepts five through seven would be heavier than concepts two through four because of the need for a sufficient amount of lithium to form slush with the 141 kg of LiF. Among the three, concept five will be heavier than either six or seven due to its need for an aperture door. The weakest candidate in mass criterion is concept one; the heat pipes would increase the receiver mass to at least twice that of concept four [37].

Thus, for simplicity and light mass, the eighth concept is chosen for preliminary design.

6.5. Preliminary Design Procedure

A. Reference Cycle and Top Li Temperature Determination

First, the dependence of the collector-receiver assembly mass on the two variables, the binary cyle efficiency and the lithium ΔT was determined. The assembly mass refers to the sum of masses of the collector mirror, the lithium TES, the receiver, the heat exchanger, the lithium container, and the meteorite shielding.

The mirror mass is inversely proportional to the cycle efficiency and the fourth power of average receiver temperature which is assumed to be equivalent to the average lithium temperature.

$$average\ lithium\ temperature = 4\sqrt{\frac{maximum\ Li\ temperature^4 + minimum\ Li\ temperature^4}{2}}$$

The average receiver temperaure determines the optimum collector efficiency which is the quotient of energy absorbed by the Li TES and the Hg divided by the energy incident on the collector mirror [40]. Since the mirror is the single most massive component in the whole assembly, mirror-mass minimization is crucial to a light-weight design.

The Li TES, as discussed before, is inversely proportional to the LiΔT. However, due to the need for a positive pinch temperature difference between the temperatures of Li and Hg in the heat exchanger (Figure 33), the minimum Li temperature is actually a function of the maximum Li temperature. For this design, mercury and lithium temperatures at 3 were assumed to be 963 K and 968 K, respectively. For a given mercury cycle and m_{Hg}, amount of heat needed in the vaporizer/superheater between 3 and 5 is the product of m_{Hg} and the mercury enthalpy change between 3 and 5 (Δh_{Hg}). Thus, given the amount of heat needed by mercury between 3 and 5, the lithium mass flow rate, m_{Li}, can be determined as a function of maximum Li temperature which determines the lithium temperature difference between 3 and 5. Once the m_{Li} is known, the minimum lithium temperature can be calculated from the heat needed by mercury in the section between 2 and 3. The mass of lithium TES is the product of lithium mass flow rate and the eclipse duration time.

The receiver mass is directly proportional to the amount of energy required by the lithium TES and mercury, and, therefore, is inversely proportional to the cycle efficiency.

The heat exchanger mass is inversely proportional to the maximum lithium temperature. Using the NTU design method, a higher maximum lithium temperature will lower the effectiveness which will decrease the NTU which, in turn, will decrease the necessary area, and consequently the mass.

The lithium container mass is also inversely proportional to the maximum lithium temperature: a higher maximum lithium temperaure means a lower mass of lithium for TES which leads to a lower volume container.

The meteorite shielding mass is inversely proportional to both the cycle efficiency and the maximum lithium temperature. Since the shielding mass is proportional to the exposed area [44], lowering the exposed receiver area (with a higher cycle efficiency) and the lithium container area (with a higher maximum lithium temperature) will decrease the shielding mass.

Initially for a given maximum lithium temperature and the reference binary cycle, the overall binary cycle efficiency was varied by varying the m_{Hg}. The equations for the calculations of the cycle efficiency and the masses fo the components are listed in Appendix B. One constraint was continuous power output of 25 kWe. The results of analysis are shown in Figure 34. Figure 34a shows that the maximum cycle efficiency occurs at the m_{Hg} at which the heat out of the Hg cycle matches exactly the heat needed by the toluene cycle. Consequently, it can be seen that assembly mass is minimized at the same m_{Hg} for concept two (Figure 34b), concept eight with maximum lithium temperature of 1255 K (Figure 34c) and 1400 K (Figure 34d).

Once the relationship for the optimum m_{Hg} for a given binary cycle was determined, the second analysis varied the cycle efficiency by varying the superheat temperature of mercury (T5 in Figure 33) while letting the rest of the parameters remain constant. Thus the input variables were the maximum Li temperature and the mercury cycle parameters - the maximum mercury temperature , maximum mercury enthalpy (enthalpy at T5), P/m_{Hg}, and Q_{out}/m_{Hg}. The toluene cycle parameters were assumed to remain constant at reference values. The equations for this analysis are listed in Appendix C. Figure 35 shows the overall cycle efficiency as a function of maximum mercury temperature, and Figure 36 shows the total assembly mass as a function of maximum mercury temperature at varying maximum lithium temperatures. Figure 39 also shows the total assembly mass estimates for concepts two and three for comparison. The mass difference between concepts two and three are due to the shielding mass difference. Concept two, which has the LiF TES integrated into the receiver, requires shielding just for the receiver while concept three, whose LiF TES is outside the receiver, requires shielding for

both the receiver and the container. The receiver mass alone for concept one (9.7 kg/kWt) is 769.8 kg. Addition of mirror mass and shielding mass would put the combined mass over 1000 kg. From the two graphs, it can be seen that the overall cycle efficiency and the total assembly mass are not very sensitive to maximum mercury temperature. However, the assembly mass is strongly influenced by the maximum lithium temperature. For example, the lithium TES is not competitive with concept two unless the maximum lithium temperature exceeds 1255 K. Therefore, it was decided to assume the same reference cycle used by Fox and Cotton, and design receivers for the maximum lithium temperatures of 1255 K and 1400 K. Variables are listed in Table 5.

B. Receiver Design

The codes, CAV2 and CVT2, initially written at Ford Aerospace and modified at Sandia, were used to calculate the flux distribution and the Li temperature distribution in a given receiver geometry, respectively.

The receiver material assumed in the design was Mo and it was also assumed that a coating would be used in the receiver cavity to increase the surface's emissivity to 0.9 from that of uncoated Mo of 0.1. The reflectivity assumed for the coating was 0.3.

Below is a table of ther relevant input variables for the two cases (the quantities in parentheses are the actual quantities/units used in the codes).

Maximum Li T	1255 K (982 C)	1400 K (1127 C)
Minimum Li T	922 K (649 C)	899 K (626 C)
m_{Li}	(639.488 lbm/hr)	(424.845 lbm/hr)

To determine the most mass-effective receiver, various receiver geometries shown in Figure 37 were tried for a constant mirror size and aperture size. The results showed that the shape C was the most mass-effective shape (highest LiΔT/kg receiver). For the chosen shape C, the lithium flow area assumed is an annulus as shown in Figure 38. Easiest way to visualize the geometry is to imagine one shell lying inside another shell of exactly the same shape but of a slightly larger size. The size difference will determine the Reynolds number and pressure drop of the lithium flow, and, consequently the heat transfer coefficient from the receiver to lithium. Lithium is introduced into the receiver at the beginning section of the cone section and removed at the middle of the spherical section.

Annulus flow area means increased risk of single point failure. This increased risk is compensated by having receiver wall thickness of 0.001 m (greater than twice the 90 % no-penetration thickness of 0.000473 m) and multiple-layer foil insulation/shielding of combined thickness 0.000473 m. A compromise design could

include four fins connecting the inner and outer area into four equal sections, reducing the single-point-failure risk and improving the structural rigidity of the receiver at the expense of a slightly higher mass.

The optimum aperture sizes were determined for C-type receivers of different sizes. The procedure was similar; for a constant mirror size and a receiver size, the aperture size was varied to find the optimum aperture size. Figure 39 shows the dimensions of four trial receivers with optimized apertures.

The next step was to find the minimum collector-receiver mass combination. In the initial mass sensitivity analysis, the collector efficiency calculated was an optimum collector efficiency based solely on the aperture size. The use of CAV2/CVT2 codes, however, enabled us to take the receiver's shape and mass into consideration. The underlying assumption is that, although their values might differ slightly, the optimized total collector-receiver assembly mass based on aperture size alone (as was done in the initial analysis) has a similar dependence on the maximum lithium temperature and the maximum mercury temperaure as does the optimum collector-receiver based on aperture size and receiver shape/mass (using CAV2/CVT2). Thus, for the trial receivers, the collector sizes were varied until the desired lithium temperature rises were achieved. The results are shown below.

Maximum Lithium Temperature = 1400 K

Type	Collector η	Receiver Mass	Mirror Mass	Total Mass
C1	0.8185	5.5493	307.6885	313.2378
C2	0.8314	9.7153	302.94	312.6553
C3	0.8382	14.5537	300.4762	315.0299
C4	0.8413	19.0381	299.3569	318.395

$^{*}Q_{receiver}/Q_{mirror\ reflected} = 0.982$

$Q_{Li}/Q_{receiver} = 0.937$

Maximum Li Temperature = 1255 K

Type	Collector η	Receiver Mass	Mirror Mass	Total Mass
C1	0.8217	5.5493	306.5106	312.06
C2	0.8371	9.7153	300.8794	310.595
C3	0.8464	14.5537	297.5643	312.118
C4	0.8506	19.0381	296.1078	315.146

$^{**}Q_{receiver}/Q_{mirror\ reflected} = 0.983$

$Q_{receiver}/Q_{receiver} = 0.944$

The CAV2/CVT2 output for the two chosen receivers (with *'s) are shown in Tables 6 and 7.

C. Heat Exchanger Design

For the heat exchanger design, a counter-flow type with the mercury flowing in the inner tube with a swirl-flow inducer was assumed. The design was split into four regions: the preheater, the vaporizer for x < 0.88, the vaporizer for x > 0.88, and the superheater. The preheater heat transfer and pressure drop were determined from [42]

	Laminar	Turbulent
Nu	3.66	$6.7 + 0.0041(RePr)^{0.793}e^{41.8Pr}$
ff	16/Re	$0.0791/Re^{0.25}$ for Re < 35000
		$0.046/Re^{0.20}$ for Re >35000

$$P_{final}=P_{initial} - (\frac{2ffpV^2 length}{D})$$

The superheat section's pressure drop was determined by the same method as above: its heat transfer was determined from

Nu	3.66	$0.023Re^{0.8}Pr^{0.4}$

To determine the pressure drop in the vaporizer, Martinelli-Lockhart's separated two phase model was used for x less than 0.88, and homogeneous flow model was used for x greater than 0.88 [34] (Appendix D). The heat transfer correlations used for x greater than 0.88 is the same as the one used for the superheater section. The heat transfer coefficient (h) correlation used for x less than 0.88 is [34]

$$h = 3.5 h_{fo} (\frac{1}{X_{tt}})^{0.5}$$

$$X_{tt} = (\frac{x}{1-x})^{0.9}(\frac{v_g}{v_f})^{0.5}(\frac{\mu_g}{\mu_f})^{0.1}$$

h_{fo}= heat transfer coefficient from preheater section at T_{sat}

g=vapor

f=liquid

Given the input variables of minimum and maximum lithium temperatures, the program initially assumed one tube and counter-flow heat exchanger with the mercury hydraulic diameter of 0.001 m and the lithium hydraulic diameter of 0.001 m. The program calculated the length and pressure drop for each incremental temperature rise (the preheater and superheater) and for each quality rise (vaporizer). The required conditions

at the exit were i)vapor velocity under Mach 1; ii) mercury pressure drop of less than 2%; and iii) lithium pressure drop of less than 0.01 %. The mercury and lithium hydraulic diameters were accordingly swept up from 0.001 if any of the conditions were not met. Then the whole process was repeated for a new number of tubes upto 20. The thickness of pipes was assumed to be 0.0005 m for mass calculation. Of the acceptable models, the following were chosen.

Maximum Li T	1255 K	1400 K
Mass	2.381 kg	1.292 kg
Number of Tubes	7	10
Length	1.322 m	0.669 m
Hg Hydraulic Diameter	0.004 m	0.003 m
Li Hydraulic Diameter	0.006 m	0.004 m
Exit Hg Pressure	4.9126 MPa	4.9113 MPa
Exit Li Pressure	0.0999 MPa	0.0999 MPa

initial Hg pressure 5.0 MPa

initial Li pressure 0.1 MPa

D. Container Design

Figure 40 shows one possible container configuration. During the insolation valves A and B are open, pump B is off and pump A is on. The pressure difference between the hot and the cold lithium, due to pressure drop in the heat exchanger and plumbing, will push the piston to the left, filling the container with hot lithium. During the eclipse, valves A and B are closed, pump A is off and pump B is on. Pump B's action raises the cold lithium's pressure above that of the hot lithium; thus, piston is pushed to the right, filling the container with cold lithium. Once the insolation resumes, opening of valves A and B and the action of pump A decreases the pressure of cold lithium in the container to that of cold lithium at the heat exchanger exit and the cycle repeats itself.

To accomodate the volume change of lithium (~10%) over the temperature range, the container can be designed for the higher volume (at the maximum temperature) with the lithium accumulator attached to the cold end. The hot lithium will completely fill the container volume; 10% volume void, which forms with the cold lithium, can be filled by injecting more lithium into the container from the accumulator. Thus, the lithium loop can be controlled.

6.6. Results

The complete data on the optimized collector-receiver assembly is as follows.

Maximum Li T	1255 K	1400 K

Mirror

required mirror area	100.9315 m²	101.7165 m²
outer radius of mirror	5.6736 m	5.6956 m
inner radius of mirror	0.25 m	0.25 m
rim angle	45 degrees	45 degrees

Receiver

aperture radius	0.11 m	0.11 m
axial length of conical section	0.10 m	0.10 m
final radius of conical section	0.20 m	0.20 m
axial length of cylindrical section	0.10 m	0.10 m
radius of cylindrical section	0.20 m	0.20 m
radius of the spherical section	0.20 m	0.20 m
gap between the shells	0.002 m*	0.002 m*
thickness of each shell	0.001 m	0.001 m

Heat Exchanger

number of tubes	7	10
heat exchanger length	1.322 m	0.699 m
Hg diameter	0.004 m	0.003 m
Li diameter	0.006 m	0.004 m
thickness of pipe	0.0005 m	0.0005 m

*tested case: results in neligigible Li pressure drops in both receivers of
less than 0.2 Pa which is less than 2.0×10^{-4} % of the initial 0.1 MPa.

Shield Thickness

Receiver	0.4734×10^{-3} m	0.4734×10^{-3} m
Li Container	0.6888×10^{-3} m	0.6391×10^{-3} m
Heat Exchanger	0.3533×10^{-3} m	0.2740×10^{-3} m

Insulation layers

Recever	19	19
Li Container	27	25
Heat Exchanger	14	11

Radiation Loss (% of $Q_{receiver\ cavity}$)

Receiver	0.1048 %	0.1503 %
Li Container	0.456 %	0.523 %
Heat Exchanger	0.079 %	0.056 %

Mass breakdown is as follows.

	1255 K	1400 K
Maximum Li T	1255 K	1400 K
Mass of Li TES	106.7525 kg	70.9518 kg
Mass of Mirror	302.7945 kg	305.1495 kg
Mass of Receiver	9.7928 kg	9.7928 kg
Mass of Li Container	19.3119 kg	14.7036 kg
Mass of Heat Exchanger	2.381 kg	1.292 kg
Mass of Shield	16.2395 kg	11.7991 kg
Assembly Mass	457.2722 kg	413.688 kg
Assembly Mass Predicted from Initial Sensitivity Analysis	459.2103 kg	418.9645 kg

The probability of protection against damage by meteorites was set at 0.90 to calculate the required mass. The mass data shows a good agreement between the initial assumed values and the actual design values. It seems reasonalble to believe that optimization of each component would reduce the total assembly mass.

6.7. Conclusion

This section discussed a receiver concept using liquid lithium as the TES. The concept's advantages are the lack of TES containment problem, the ability to handle uneven heat flux and the reduction in specific mass. The collector-receiver specific masses for concept two, concept eight with $T_{max} = 1255$ K, and concept eight with $T_{max} = 1400$ K are, respectively, 6.57 kg/kWt (18.43 kg/kWe), 6.52 kg/kWt (18.30 kg/kWe), 5.90 kg/kWt (16.5 kg/kWe). The last case provides a 10% specific mass reduction over the first two cases. Creep, which occurs at high temperaure and pressure (over 200 MPa) is avoided by using lithium at one atm, or 0.1 MPa. Furthermore, dividing TES/receiver/boiler (concepts one through five) into separate components achieves simplicity, easier maintenance, and higher reliability.

Chapter 7

Conclusions and Future Work

A study was done to improve the performance of a binary Rankine cycle solar dynamic space power system. Three key technical issues were examined: effective sealing and containment of the system's fluids; radiator mass reduction; receiver TES material containment and mass reduction. The attention was focused on the radiator and the receiver because their specific masses account for over 80% of the system's total specific mass; therefore, their mass reduction would significantly affect the system's performance.

The main results of this study suggests the following. First, fluid control system which shows potential for zero leakage can be designed, using gas-lubricated bearings and ferrofluidic seals. Gas lubrication reduces bearing power consumption and eliminates cavitation risk. Ferrofluidic seals show zero-leakage potential and static sealing capability. Second, a rotating film radiator in which a film flowing on a rotating disk rejects heat directly into space can reduce the heat pipe radiator specific mass by half to 5.59 kg/kW$_t$ or 3.52 kg/m^2. Third, a receiver using liquid lithium TES can circumvent the problems of TES containment and hot spot formation while simultaneously reducing the collector-receiver's specific mass to 5.90 kg/kW$_t$. From the above results, it seems possible to reduce the mass of current solar dynamic power system's mass without much new research and development.

Using the RFR and the lithium TES receiver would lead to a combined collector-receiver assembly and radiator mass of 642.2 kg which is less than the 888 kg assumed by Fox. Assuming the same masses for the other components, the new specific mass is 28.29 kg/kWe. This result shows that the specific mass of 38.12 kg/kWe assumed by Fox is reasonble and that it can be achieved with reliable methods.

To validate the assumptions and correlations used in this study, following set of work, to be done before full-fledged development of each component, is recommended. For bearing and seals, better analytical methods for gas foil bearing stability prediction need to be developed. Furthermore, experimental data is needed on suitability of toluene as a lubricant; foil bearing's response in magnetic imbalance in zero-gravity; and ferrofluidic seal's performance under simulated EPS conditons. For the RFR, experiments on both toluene

condensation and rotating film flow/heat transfer need to be carried out in space environment. For receiver, the compatiblity between lithium and molybdenum need to be experimentally determined. Furthermore, experimental data on lithium TES's charging/discharging time and of its ability to maintain maximum mercury temperature are needed.

The applicability of lithium TES and RFR to other systems need further exploration, especially to the Brayton cycle. Brayton cycle's heat addition and rejection over a range of temperatures makes it more appropriate for the lithium TES and RFR than the Rankine cycle. One key issue will be minimization of gas-liquid heat exchanger mass. Also development of a low-density radiator fluid would reduce the RFR's mass even further. Thus, the concepts discussed in this study not only shows potential for improving the performance of binary Rankine EPS but also looks applicable to other solar dynamic EPS.

Tables

Table 1 - Properties of Lubricant Candidates

Property	Air	Nitrogen	Toluene	Mercury
k (W/m K)	0.0388	0.0327	0.0242	0.011
C_p (kJ/kg K)	1.014	1.045	1.550	0.106
ρ (kg/m^3)	0.8711	0.8425	22.4	3.70
μ (N s/m^2)	230 x 10^{-7}	220 x 10^{-7}	570 x 10^{-7}	622 x 10^{-7}

all properties are at 400 K, except those of mercury which are at 633 K

Table 2: Rotating Film Radiator Output

radius	Re	Re$_{wave}$	T	δ
0.1000	8.6375	1.7299	348.0000	0.002626
0.1500	5.7583	1.6445	347.9604	0.002004
0.2000	4.3187	1.5864	347.8946	0.001655
0.2500	3.4550	1.5427	347.8200	0.001426
0.3000	2.8792	1.5080	347.7193	0.001263
0.3500	2.4679	1.4792	347.6100	0.001139
0.4000	2.1594	1.4547	347.4747	0.001042
0.4500	1.9194	1.4334	347.3311	0.000964
0.5000	1.7275	1.4147	347.1616	0.000898
0.5500	1.5705	1.3979	346.9842	0.000843
0.6000	1.4396	1.3828	346.7810	0.000795
0.6500	1.3288	1.3690	346.5703	0.000754
0.7000	1.2339	1.3564	346.3342	0.000718
0.7500	1.1517	1.3448	346.0909	0.000685
0.8000	1.0797	1.3340	345.8225	0.000657
0.8500	1.0162	1.3239	345.5474	0.000631
0.9000	0.9597	1.3145	345.2476	0.000607
0.9500	0.9092	1.3056	344.9416	0.000586
1.0000	0.8637	1.2973	344.6112	0.000566
1.0500	0.8226	1.2894	344.2753	0.000548
1.1000	0.7852	1.2819	343.9154	0.000531
1.1500	0.7511	1.2748	343.5505	0.000516
1.2000	0.7198	1.2680	343.1621	0.000501
1.2500	0.6910	1.2616	342.7694	0.000488
1.3000	0.6644	1.2554	342.3536	0.000475
1.3500	0.6398	1.2495	341.9343	0.000463
1.4000	0.6170	1.2438	341.4923	0.000452
1.4500	0.5957	1.2384	341.0475	0.000442
1.5000	0.5758	1.2332	340.5806	0.000432
1.5500	0.5573	1.2281	340.1116	0.000422
1.6000	0.5398	1.2233	339.6210	0.000414
1.6500	0.5235	1.2186	339.1291	0.000405
1.7000	0.5081	1.2140	338.6161	0.000397
1.7500	0.4936	1.2096	338.1025	0.000390
1.8000	0.4799	1.2054	337.5685	0.000382
1.8500	0.4669	1.2013	337.0347	0.000375
1.9000	0.4546	1.1973	336.4809	0.000369
1.9500	0.4429	1.1934	335.9282	0.000363
2.0000	0.4319	1.1896	335.3560	0.000356
2.0500	0.4213	1.1859	334.7857	0.000351
2.1000	0.4113	1.1824	334.1965	0.000345
2.1500	0.4017	1.1789	333.6100	0.000340
2.2000	0.3926	1.1755	333.0050	0.000335
2.2500	0.3839	1.1722	332.4037	0.000330
2.3000	0.3755	1.1690	331.7844	0.000325
2.3500	0.3676	1.1659	331.1696	0.000320
2.4000	0.3599	1.1628	330.5372	0.000316
2.4500	0.3526	1.1598	329.9102	0.000311
2.5000	0.3455	1.1569	329.2660	0.000307
2.5500	0.3387	1.1540	328.6282	0.000303
2.6000	0.3322	1.1512	327.9734	0.000299
2.6500	0.3259	1.1485	327.3260	0.000295
2.7000	0.3199	1.1458	326.6620	0.000292
2.7500	0.3141	1.1432	326.0063	0.000288
2.8000	0.3085	1.1406	325.3341	0.000285
2.8500	0.3031	1.1381	324.6713	0.000281
2.9000	0.2978	1.1356	323.9923	0.000278
2.9500	0.2928	1.1332	323.3234	0.000275
3.0000	0.2879	1.1308	322.6387	0.000272
3.0500	0.2832	1.1285	321.9650	0.000269

3.1000	0.2786	1.1262	321.2755	0.000266
3.1500	0.2742	1.1239	320.5981	0.000263
3.2000	0.2699	1.1217	319.9051	0.000261
3.2500	0.2658	1.1196	319.2249	0.000258
3.3000	0.2617	1.1174	318.5292	0.000255
3.3500	0.2578	1.1153	317.8474	0.000253
3.4000	0.2540	1.1133	317.1501	0.000250
3.4500	0.2504	1.1112	316.4676	0.000248
3.5000	0.2468	1.1092	315.7694	0.000245
3.5500	0.2433	1.1073	315.0871	0.000243
3.6000	0.2399	1.1053	314.3891	0.000241
3.6500	0.2366	1.1034	313.7078	0.000239
3.7000	0.2334	1.1016	313.0108	0.000237
3.7500	0.2303	1.0997	312.3314	0.000234
3.8000	0.2273	1.0979	311.6361	0.000232
3.8500	0.2244	1.0961	310.9593	0.000230
3.9000	0.2215	1.0943	310.2666	0.000228
3.9500	0.2187	1.0926	309.5932	0.000226
4.0000	0.2159	1.0909	308.9036	0.000225
4.0500	0.2133	1.0892	308.2343	0.000223
4.1000	0.2107	1.0875	307.5485	0.000221
4.1500	0.2081	1.0859	306.8839	0.000219
4.2000	0.2057	1.0842	306.2026	0.000217
4.2500	0.2032	1.0826	305.5433	0.000216
4.3000	0.2009	1.0811	304.8670	0.000214
4.3500	0.1986	1.0795	304.2136	0.000212
4.4000	0.1963	1.0780	303.5428	0.000211
4.4500	0.1941	1.0764	302.8958	0.000209
4.5000	0.1919	1.0749	302.2310	0.000208
4.5500	0.1898	1.0734	301.5910	0.000206

Table 3: Properties of various PCMs

PCM	melting T	heat of fusion	density
K_2CO_3	1170 K	236 kJ/kg	kg/m^3
KF	1125	454	2480
Na_2CO_3	1125	279	2530
Ca	1123	221	1540
LiF	1121	1,044	2640
Li BO_2	1108	698	1400
75 NaF+ 25 MgF	1105	649	2680
62.5 NaF+ 22.5 MgF+ 15 KF	1082	607	2630
NaCl	1074	484	2180
CaI	1057	142	3490
KCl	1043	372	1990
Li	453	442	534

Table 4 :Properties of TES Materials

Metal	Melting T	Boiling T	Specific Heat	Density
Li	452 K	1590 K	4161 J/kg K	534 kg/m^3
Na	371 K	1156 K	1268 J/kg K	780 kg/m^3

Table 5 : Mo, Nb, Ta Properties

parameter	Mo	Nb	Ta
melting point (K)	2883	2741	3269
k (W/m K)	126	58	59
E (GPa)	230	90	150
UTS (MPa)	260	100	135
YS (MPa)	100	*	50
creep strength (MPa)	110	20*	60***
fatigue strength	*	*	*
fracture toughness	*	*	*
oxidation onset temp (K)	773	673	573
resistant against	liquid metals mineral acids molten gases halogen vapor refractory oxides	liquid metals	liquid metals acids organic chem. salt solution gases
weak against		strong alkali mineral acids HF acid gases at high T	strong alkali halogen gases
fabricability	okay	good	good

* no available data

** 0.2 % at 973 K

*** 0.5 % at 1093 K

Table 6

A.1   REFERENCE CYCLE

ELECTRICITY OUTPUT = 25 kWe
PMAD EFFICIENCY*ALTERNATOR EFFICIENCY = 0.8309
CYCLE EFFICIENCY = 0.4293
Q INTO TES DURING INSOLATION = 41.5744 kW
Q INTO MERCURY DURING CYCLE = 70.0825 kW
TOTAL Q NEEDED IN THE CAVITY = 111.6569 kW
ORBIT = 35 MIN ECLIPSE AND 59 MIN INSOLATION = 94 MIN

MERCURY FLOWRATE = 0.2127 kg/s
TOLUENE FLOWRATE = 0.0978 kg/s
POWER FROM MERCURY CYCLE = 15.9033 kW
POWER FROM TOLUENE CYCLE = 14.1831 kW
Q FROM MERCURY CYCLE = 54.193 kW
Q INTO TOLUENE CYCLE = 54.193 kW

MAXIMUM LI T	LITHIUM FLOWRATE
1400 K	0.0366 kg/s
1255 K	0.0506 kg/s

A.2   MERCURY PROPERTIES USED

	LIQUID	VAPOR
THERMAL CONDUCTIVITY	13.56 W/m K	17.16E-3 W/m K
SPECIFIC HEAT	0.142 kJ/kg K	0.106 kJ/kg K
VISCOSITY	0.787E-3 Ns/m^2	984.4E-7 Ns/m^2

A.3   LITHIUM PROPERTIES USED

THERMAL CONDUCTIVITY	53.5 W/m K
SPECIFIC HEAT	4161.2 J/kg K
VISCOSITY	0.4316e-03 Ns/m^2

FOR LISTING TYPE "1", ELSE "0"

K	R-0 W	V-0 W	S-0 W	QR-0 W/M^2	TS D-C	TW1 D-C	TW2 D-C	TF D-C	
0	3872.	0.	3598.	101852.	(LOSS THROUGH APERTURE)				
1	2703.	0.	747.	163297.	1039.				
2	2676.	0.	830.	143329.	998.			(626.)	
3	962.	0.	579.	46311.	639.	638.	638.	631.	O
4	1110.	0.	660.	48475.	651.	650.	650.	644.	O
5	1273.	0.	736.	50893.	664.	663.	663.	657.	O
6	1448.	0.	797.	53390.	678.	677.	677.	671.	O
7	1113.	0.	615.	53145.	689.	688.	688.	683.	O
8	1171.	0.	804.	55914.	701.	700.	699.	693.	O
9	1243.	0.	1047.	59360.	715.	714.	714.	706.	O
10	1334.	0.	1345.	63682.	733.	732.	731.	722.	O
11	1446.	0.	1679.	69043.	754.	753.	752.	741.	O
12	1580.	0.	2018.	75449.	778.	777.	776.	763.	O
13	2629.	0.	3612.	86942.	813.	811.	810.	795.	O
14	3029.	0.	4417.	101636.	859.	858.	856.	839.	O
15	3433.	0.	4858.	118697.	907.	907.	906.	887.	O
16	3765.	0.	4819.	136274.	956.	955.	953.	935.	O
17	3952.	0.	4376.	152455.	998.	997.	995.	978.	O
18	3980.	0.	3846.	166917.	1033.	1032.	1031.	1015.	O
19	3845.	0.	3313.	179489.	1062.	1061.	1060.	1046.	O
20	3551.	0.	2787.	190069.	1085.	1084.	1083.	1070.	O
21	3113.	0.	2270.	198638.	1104.	1103.	1102.	1090.	O
22	2551.	0.	1759.	205217.	1118.	1117.	1116.	1105.	O
23	1893.	0.	1263.	210008.	1128.	1128.	1127.	1116.	O
24	1175.	0.	883.	215240.	1139.	1138.	1137.	1123.	O
25	987.	0.	795.	539498.	1521.			(1127.)	

SOLAR ENERGY INPUT: 119092. W.; ENERGY OUT: 119091. W
RSS OF (Q2-Q1) = 0.45 NO. OF ITERATION = 21

ALPHA-E	EPSILON-E	(T,CAV)MEAN,C
0.969788	0.967181	894.26

--------- Q-TABLE ---------

K	CO-CUM W	PCT	CO W	PCT	QS-IN W/M^2	QC-OUT W/M^2
2	0.	0.0	0.	0.0	1218.	0.
3	2600.	2.3	2600.	2.3	1114.	125123.
4	5396.	4.8	2796.	2.5	1033.	122107.
5	8450.	7.6	3055.	2.7	967.	122152.
6	11662.	10.4	3211.	2.9	914.	118415.
7	13796.	12.4	2134.	1.9	25738.	101913.
8	16400.	14.7	2603.	2.3	51570.	124301.
9	19574.	17.5	3174.	2.8	85724.	151556.
10	23429.	21.0	3855.	3.5	128387.	184052.
11	28025.	25.1	4596.	4.1	176731.	219459.
12	33296.	29.8	5271.	4.7	225650.	251667.
13	42351.	37.9	9055.	8.1	300267.	299447.
14	52783.	47.3	10432.	9.3	396362.	350106.
15	63718.	57.1	10934.	9.8	462221.	378055.
16	74070.	66.4	10353.	9.3	483811.	374760.
17	83023.	74.4	8952.	8.0	465059.	345319.
18	90496.	81.1	7473.	6.7	440046.	313370.
19	96608.	86.5	6112.	5.5	417841.	285331.
20	101504.	90.9	4896.	4.4	399576.	262078.
21	105320.	94.4	3816.	3.4	385125.	243489.
22	108169.	96.9	2849.	2.6	373838.	229144.
23	110166.	98.7	1996.	1.8	369443.	221517.
24	111622.	100.0	1456.	1.3	441181.	266598.
25	111622.	100.0	0.	0.0	772483.	0.

RECEIVER EFFICIENCY = 111622./119092. = 0.93727

INLET TEMP. (TO) = 626. DEG-C; HM(TO) = -65670. W FOR 424.84 LBM/HR

Table 8: CVT2 output for $T_{max,Li}$ = 1255 K

FOR LISTING TYPE '1', ELSE '0'

K	R-0 W	V-0 W	S-0 . W	QR-0 W/M^2	TS D-C	TW1 D-C	TW2 D-C	TF D-C	
0	2990.	0.	3574.	78645.	(LOSS THROUGH APERTURE)				
1	2294.	0.	742.	138582.	988.				
2	2260.	0.	824.	121069.	948.			(649.)	
3	970.	0.	575.	46669.	658.	657.	657.	652.	0
4	1097.	0.	655.	47902.	664.	664.	663.	658.	0
5	1232.	0.	731.	49252.	671.	671.	670.	665.	0
6	1373.	0.	792.	50620.	679.	678.	678.	673.	0
7	1055.	0.	610.	50391.	685.	684.	684.	680.	0
8	1090.	0.	797.	52066.	692.	692.	691.	686.	0
9	1134.	0.	1038.	54160.	701.	701.	700.	694.	0
10	1189.	0.	1334.	56784.	713.	712.	711.	703.	0
11	1257.	0.	1668.	60013.	726.	726.	725.	715.	0
12	1337.	0.	2005.	63828.	742.	741.	740.	728.	0
13	2133.	0.	3591.	70537.	766.	764.	763.	747.	0
14	2355.	0.	4393.	79019.	797.	796.	794.	777.	0
15	2562.	0.	4830.	88597.	831.	830.	828.	809.	0
16	2713.	0.	4789.	98217.	864.	862.	861.	842.	0
17	2773.	0.	4354.	106952.	893.	891.	890.	872.	0
18	2736.	0.	3819.	114749.	917.	916.	914.	898.	0
19	2606.	0.	3290.	121637.	938.	937.	935.	920.	0
20	2383.	0.	2769.	127536.	956.	954.	953.	938.	0
21	2075.	0.	2254.	132390.	970.	968.	967.	953.	0
22	1693.	0.	1746.	136178.	981.	979.	978.	965.	0
23	1253.	0.	1254.	138975.	989.	988.	987.	974.	0
24	776.	0.	874.	142197.	998.	996.	995.	980.	0
25	935.	0.	789.	511313.	1499.			(982.)	

SOLAR ENERGY INPUT: 118317. W.; ENERGY OUT: 118310. W
RSS OF (Q2-Q1) = 0.42 NO. OF ITERATION = 19

ALPHA-E	EPSILON-E	(T,CAV)MEAN,C
0.969790	0.955034	824.64

-------- Q-TABLE --------

K	CQ-CUM W	PCT	CQ W	PCT	QS--IN W/M^2	QC-OUT W/M^2
2	0.	0.0	0.	0.0	1194.	0.
3	2059.	1.8	2059.	1.8	1093.	99077.
4	4317.	3.9	2257.	2.0	1013.	98578.
5	6800.	6.1	2483.	2.2	949.	99309.
6	9438.	8.4	2638.	2.4	898.	97253.
7	11267.	10.1	1830.	1.6	25327.	87354.
8	13546.	12.1	2279.	2.0	50867.	108807.
9	16390.	14.7	2844.	2.5	84765.	135792.
10	19916.	17.8	3526.	3.2	127221.	168351.
11	24195.	21.7	4279.	3.8	175415.	204315.
12	29190.	26.1	4995.	4.5	224236.	238508.
13	37927.	33.9	8736.	7.8	298617.	288908.
14	48239.	43.2	10312.	9.2	394315.	346068.
15	59272.	53.0	11033.	9.9	459675.	381484.
16	69940.	62.6	10667.	9.5	480836.	386143.
17	79396.	71.1	9456.	8.5	462817.	364756.
18	87475.	78.3	8079.	7.2	436816.	338799.
19	94258.	84.4	6783.	6.1	414957.	316643.
20	99830.	89.3	5572.	5.0	397017.	298243.
21	104269.	93.3	4439.	4.0	382456.	283247.
22	107647.	96.3	3378.	3.0	371224.	271682.
23	110044.	98.5	2397.	2.1	366705.	265911.
24	111746.	100.0	1702.	1.5	436677.	311670.
25	111746.	100.0	0.	0.0	765952.	0.

RECEIVER EFFICIENCY = 111746./118317. = 0.94446

INLET TEMP. (TO) = 649. DEG-C; HM(TO) = -91042. W FOR 639.49 LBM/HR
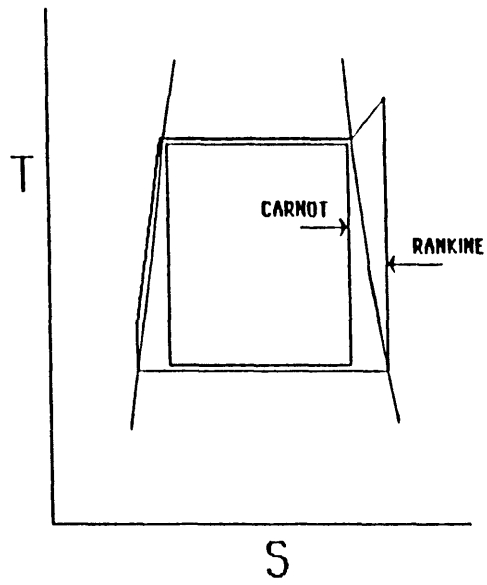
Figure 1 – Rankine and Carnot Cycles on
Temperature-Entropy Diagram
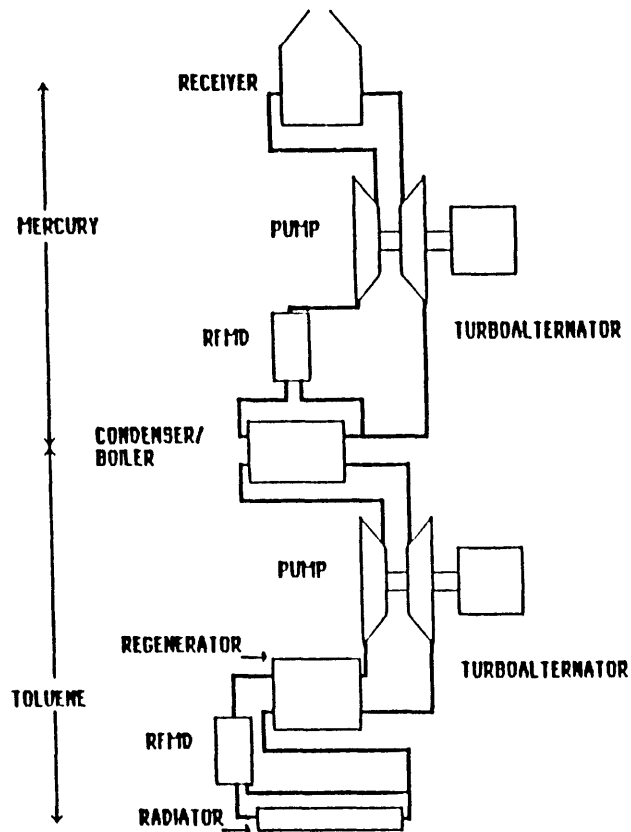
Figure 2 –   Binary Cycle Schematic
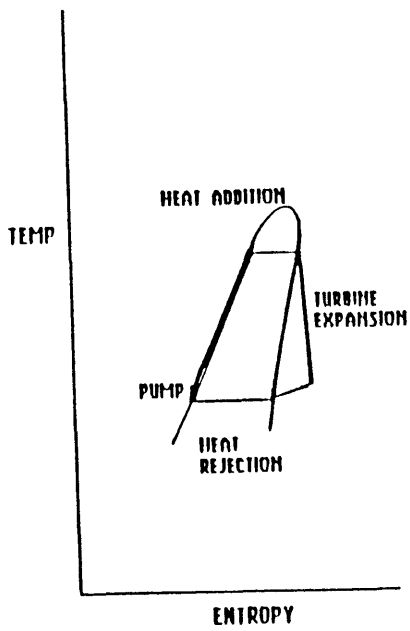
Figure 3 - Organic Rankine Cycle
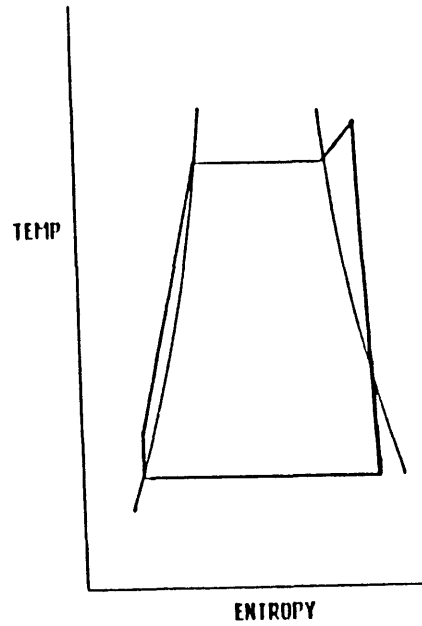
Figure 4 - Mercury Rankine Cycle with Superheat

	T(K)	P(MPa)
1	654	0.156
2	655	5.0
3	963	5.0
4	963	5.0
5	1033	5.0
6	654	0.156

	T(K)	P(MPa)
1	350	0.034
2	354	5.17
3	359	5.03
4	489	4.62
5	644	4.14
6	538.5	0.042
7	375	0.038
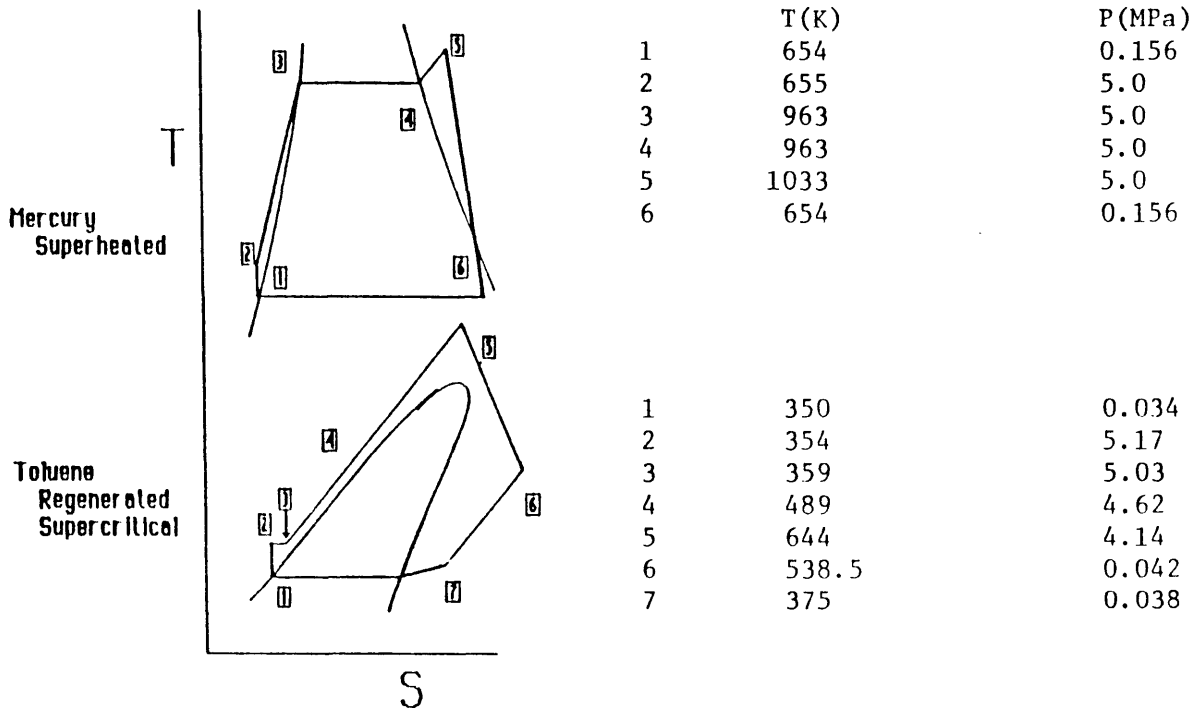
Figure 5: The reference cycle from Fox and Cotton

Bearings

Rolling Element   Fluid Film

Gas Lubrication   Liquid Lubrication

Hydrodynamic   Hydrostatic   Hybrid   Hydrostatic   Hydrostatic   Hybrid
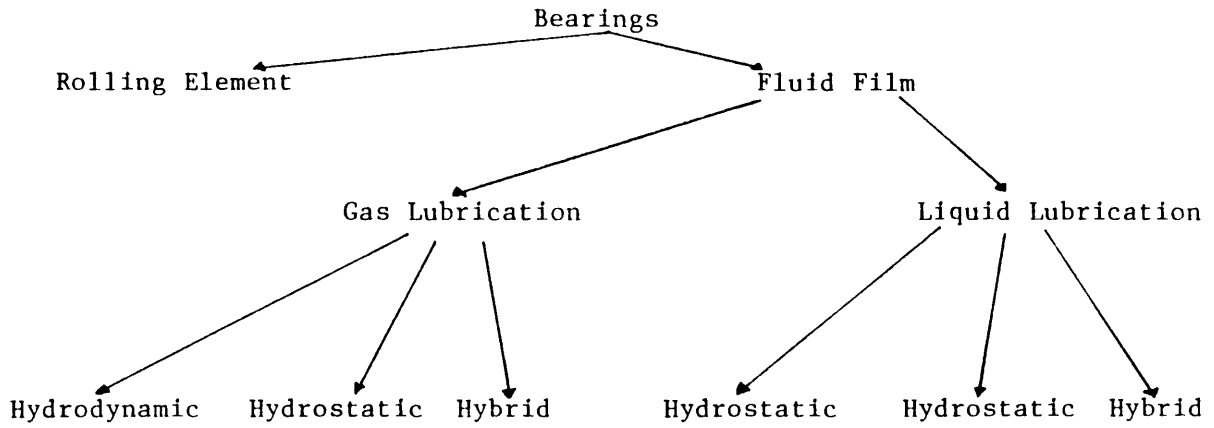
Figure   6 :   Classification of Bearings

P

W

P_{amb}

P_{supply}

P

W

U

P_{amb}
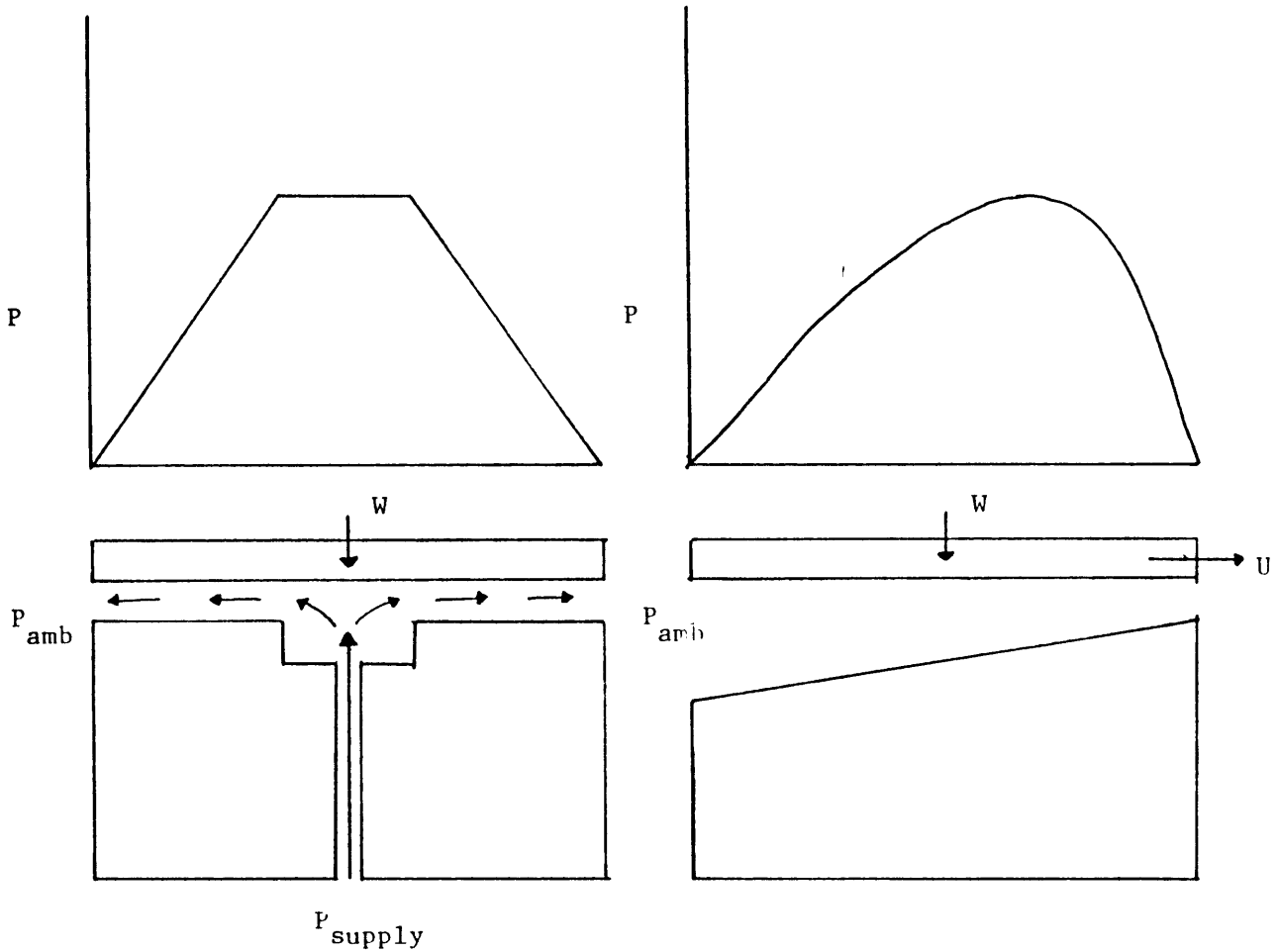
Figure   7 :   Hydrostatic (L) and Hydrodynamic (R) Bearings

FOIL HOUSING

ASSEMBLED
FOIL SEGMENTS

FOIL SEGMENT
REMOVED

"WEDGE" REGION

JOURNAL
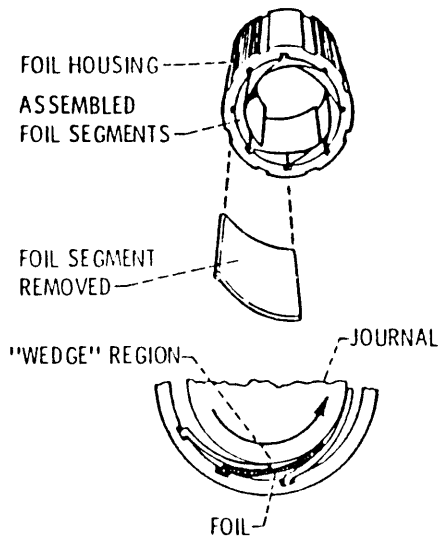
FOIL

CANTILEVERED FOIL BEARING

CLAMP
GUIDE
FOIL

90°

GUIDE

JOURNAL

LOCK
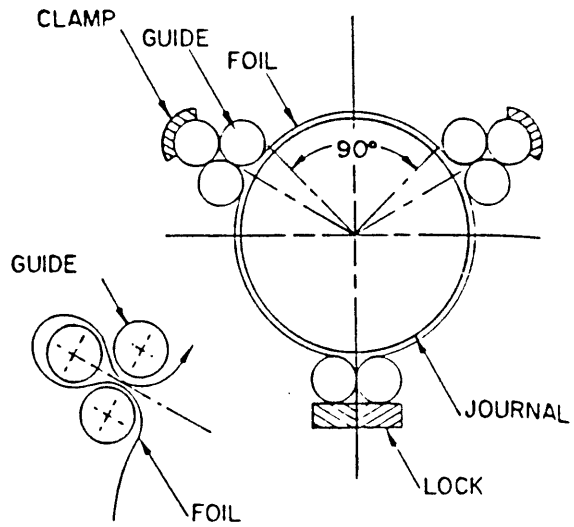
FOIL

TENSION FOIL BEARING

Figure 8: Cantilevered and Tensioned Foil Bearing

h_g h_r

ω

r_i

r_o

$p = p_a$

r_m

$p = p_a$ r

r_i

a_r

a_g

Depth, $h_g - h_r$

β

Pump-in
design

(inward
pumping)
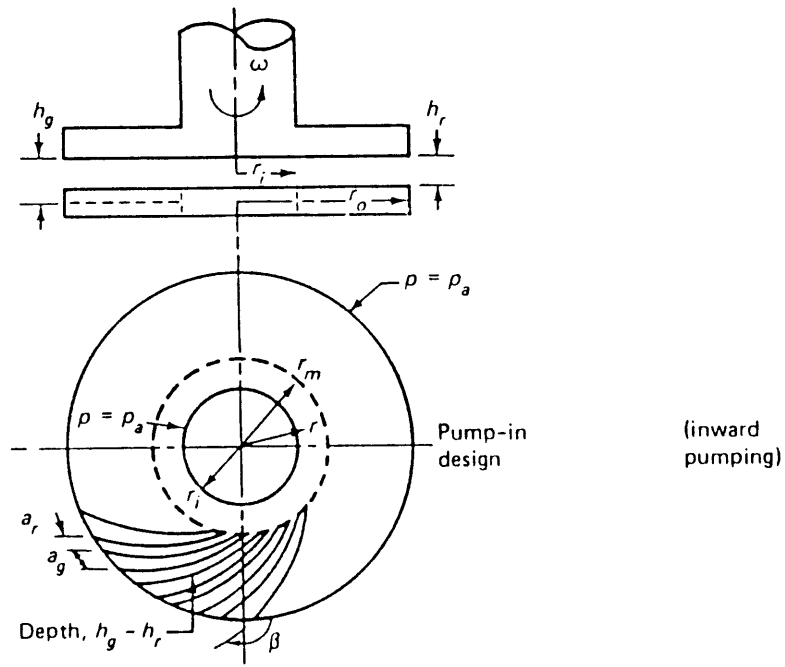
b)   Grooves on the bearing disc   (Ref. 11)

Figure 9: Bidirectional Spiral Groove Thrust Bearing

62
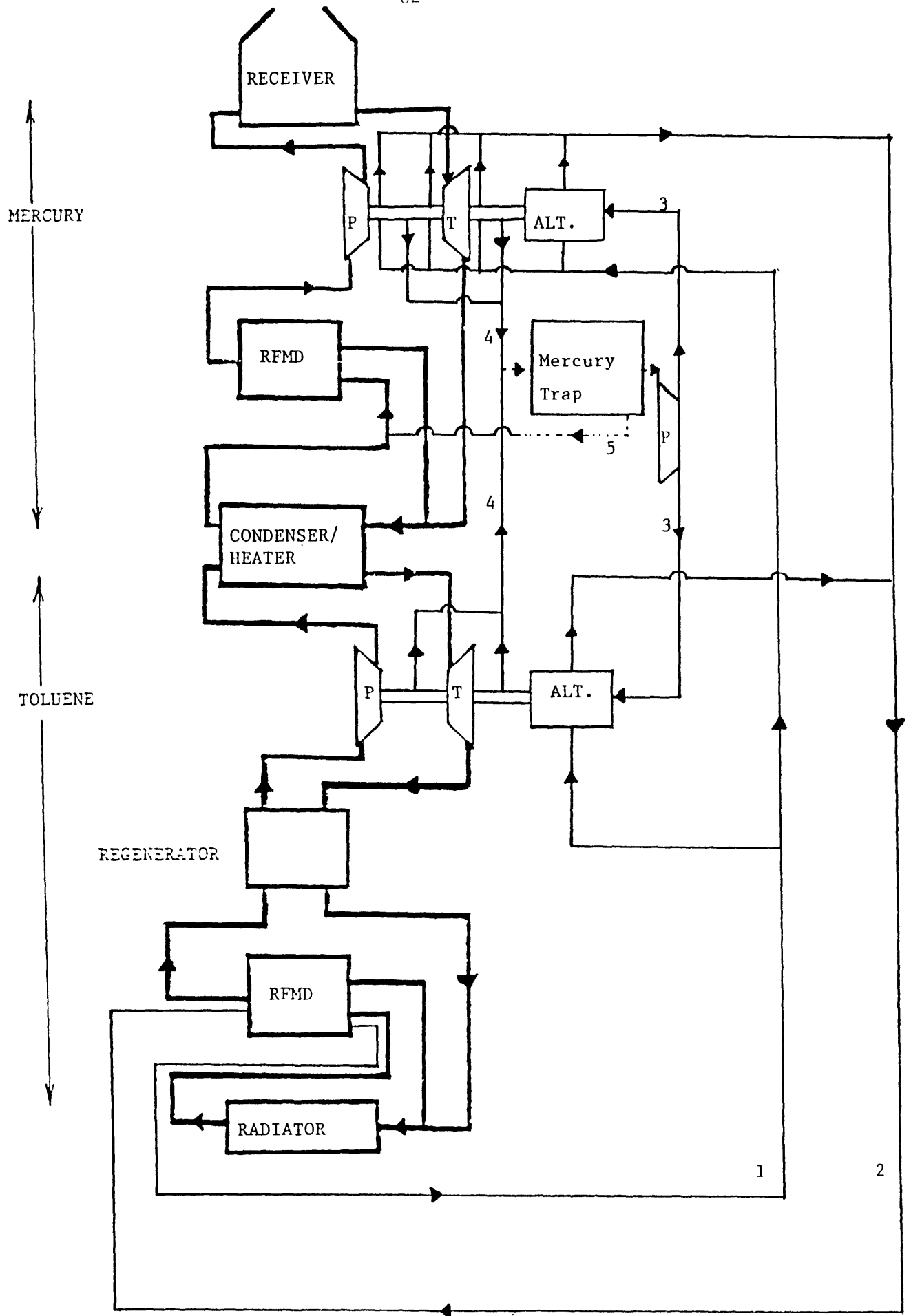
Figure10: System Schematic with Nitrogen Bearings and Mercury Trap
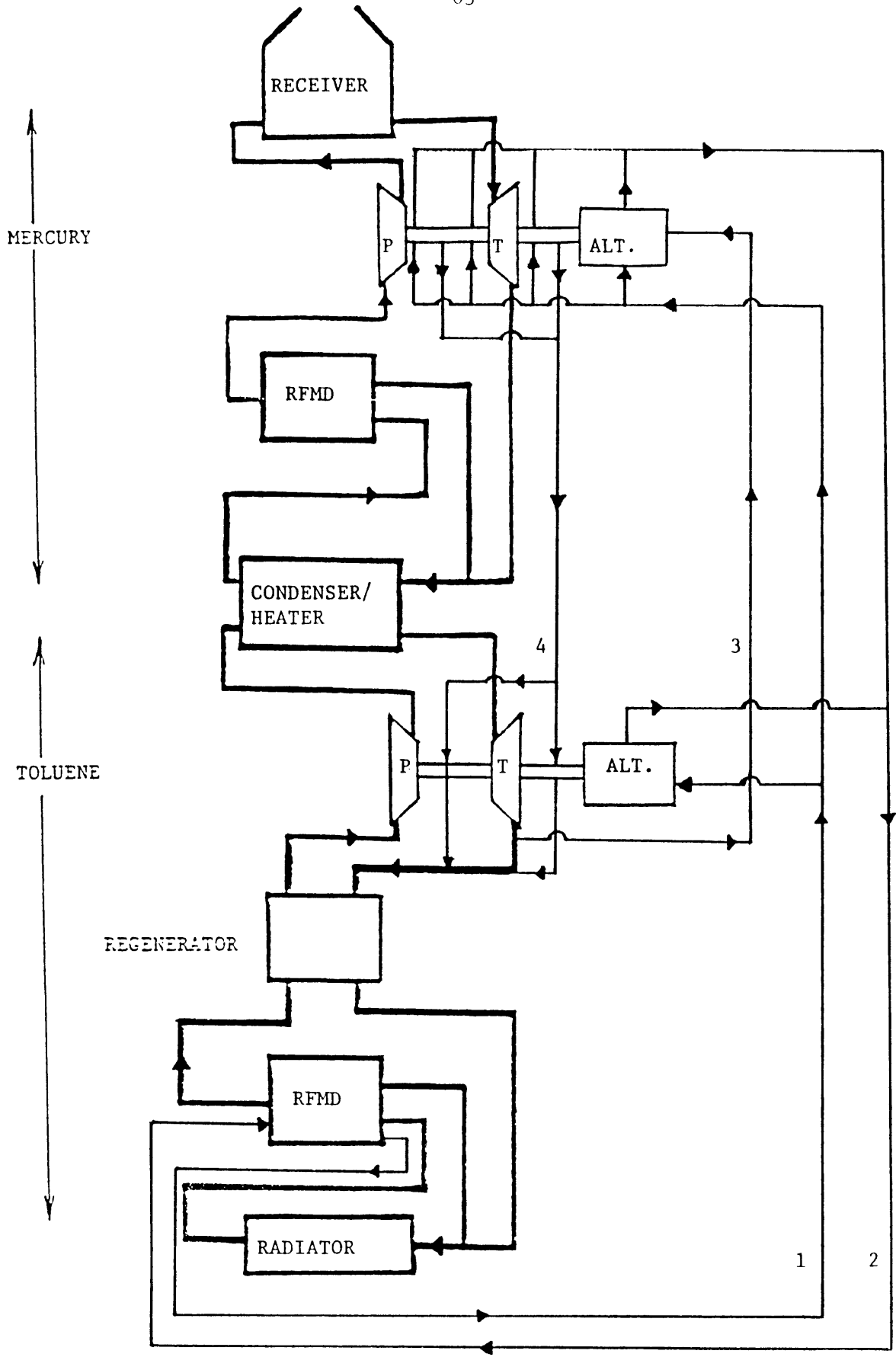
Figure 11: System Schematic with Toluene Bearings w/o Mercury Trap
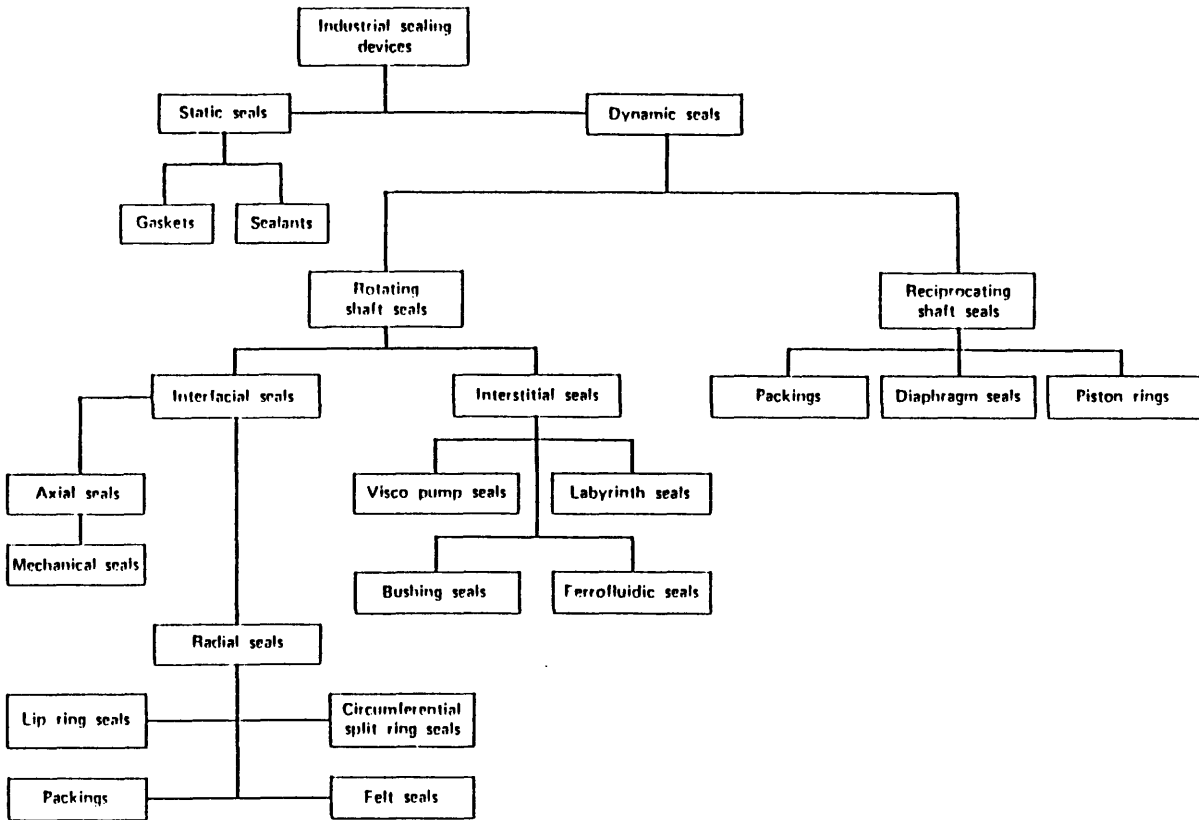
Figure 12:   Total Classification Diagram
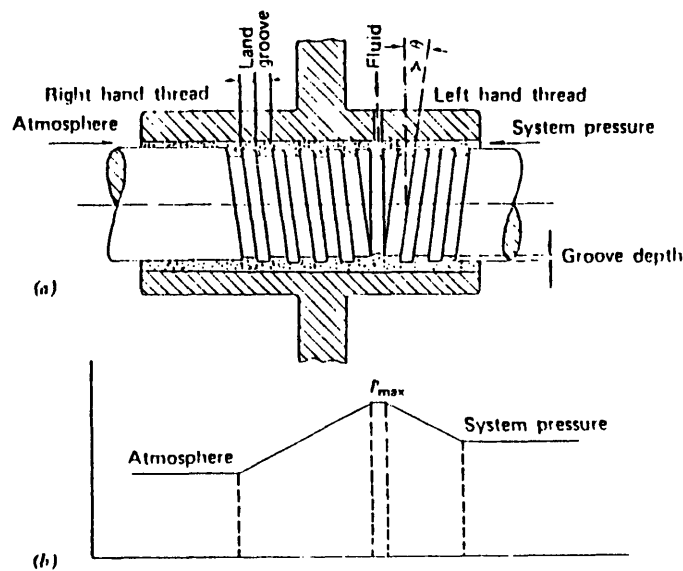
Figure 13:   a) Diagram of Crosssection of a Viscoseal

b) Axial Pressure Distribution Diagram
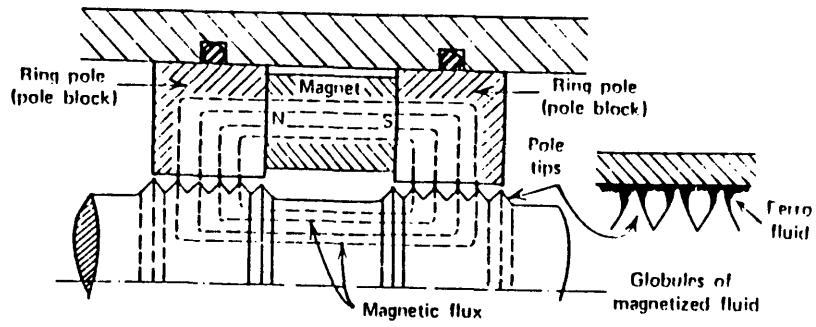
Fig. 14 : Functional mechanism of ferrofluidic seal.
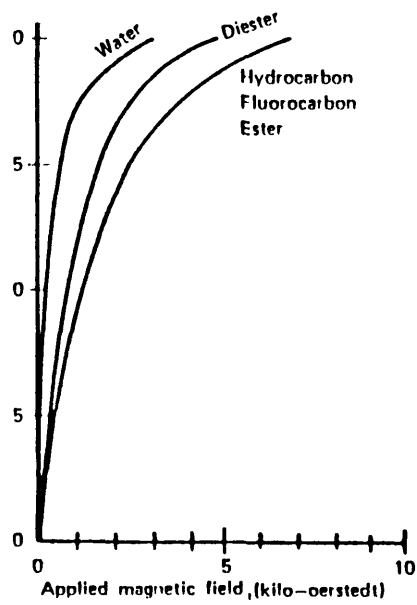
Fig. 15a Magnetization behavior of fluids.
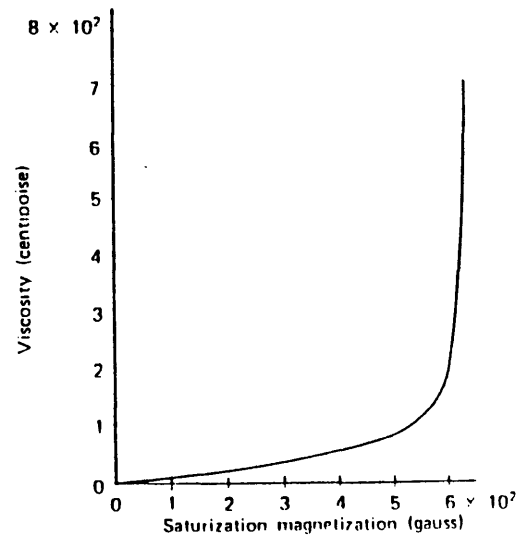
Fig. 15b Viscosity as function of magnetic saturation of ferrofluids
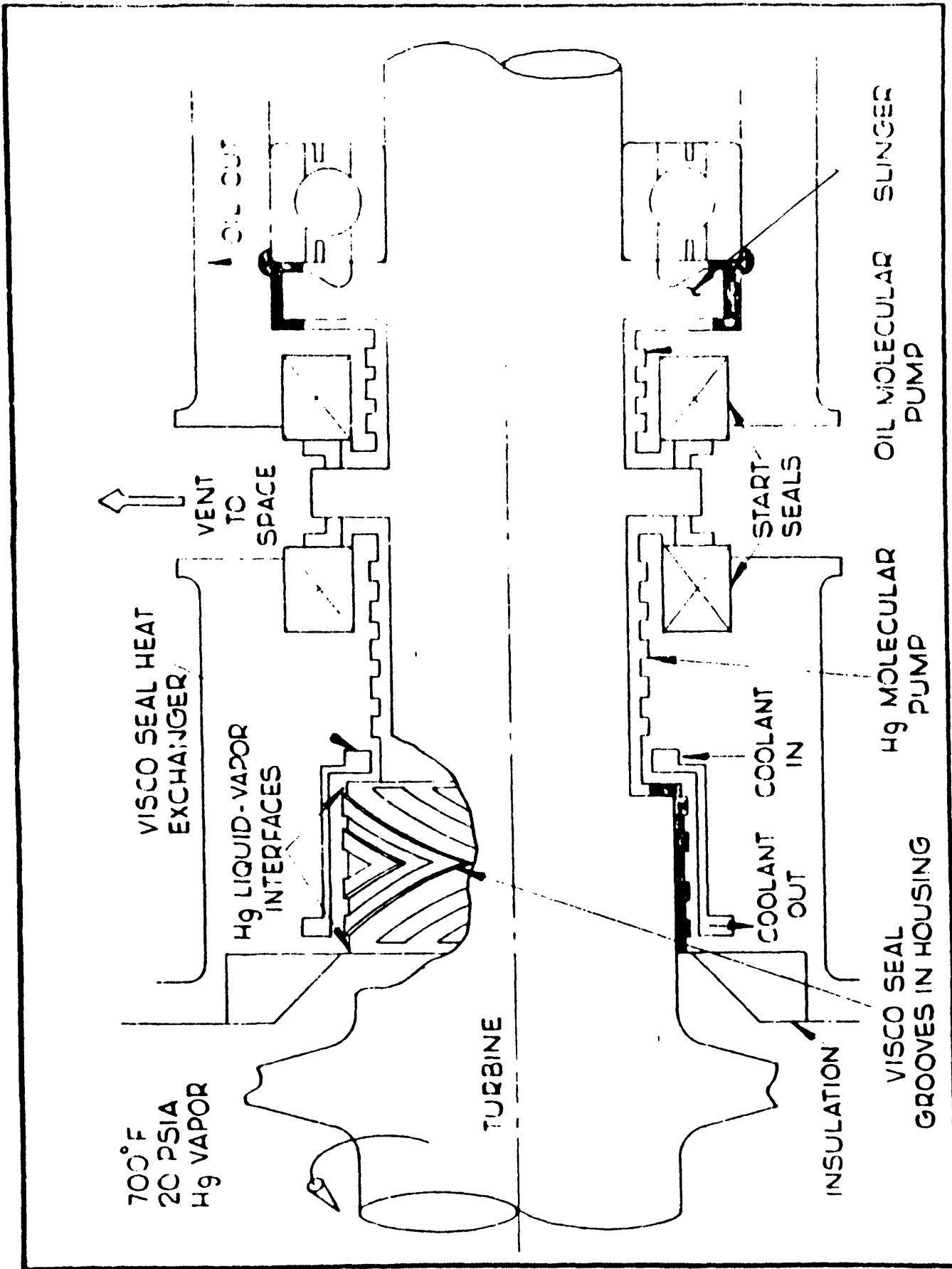
Figure16: Current Configuration - SNAP-8 Seal-To-Space
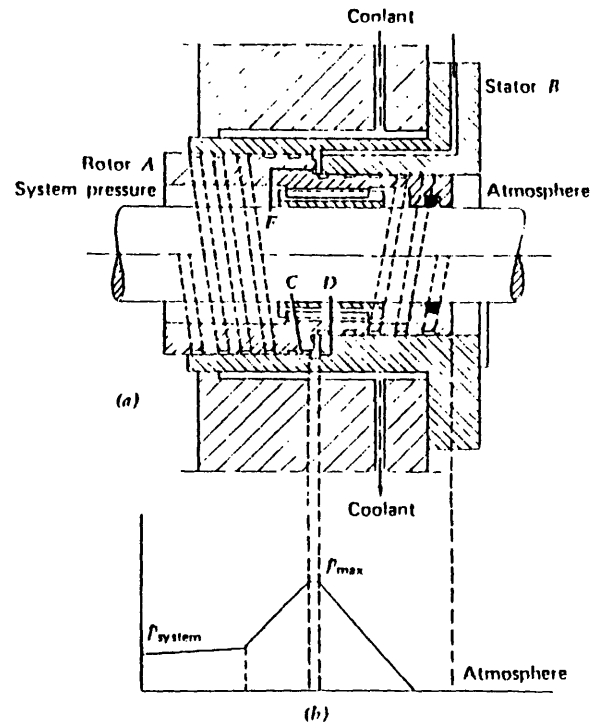
Fig. 17 : Provision of static sealing of visco seal design. (a) Static sealing provision. (b) Pressure diagram [From (3,4), courtesy of *Chemie Ingenieur-Technik.*]
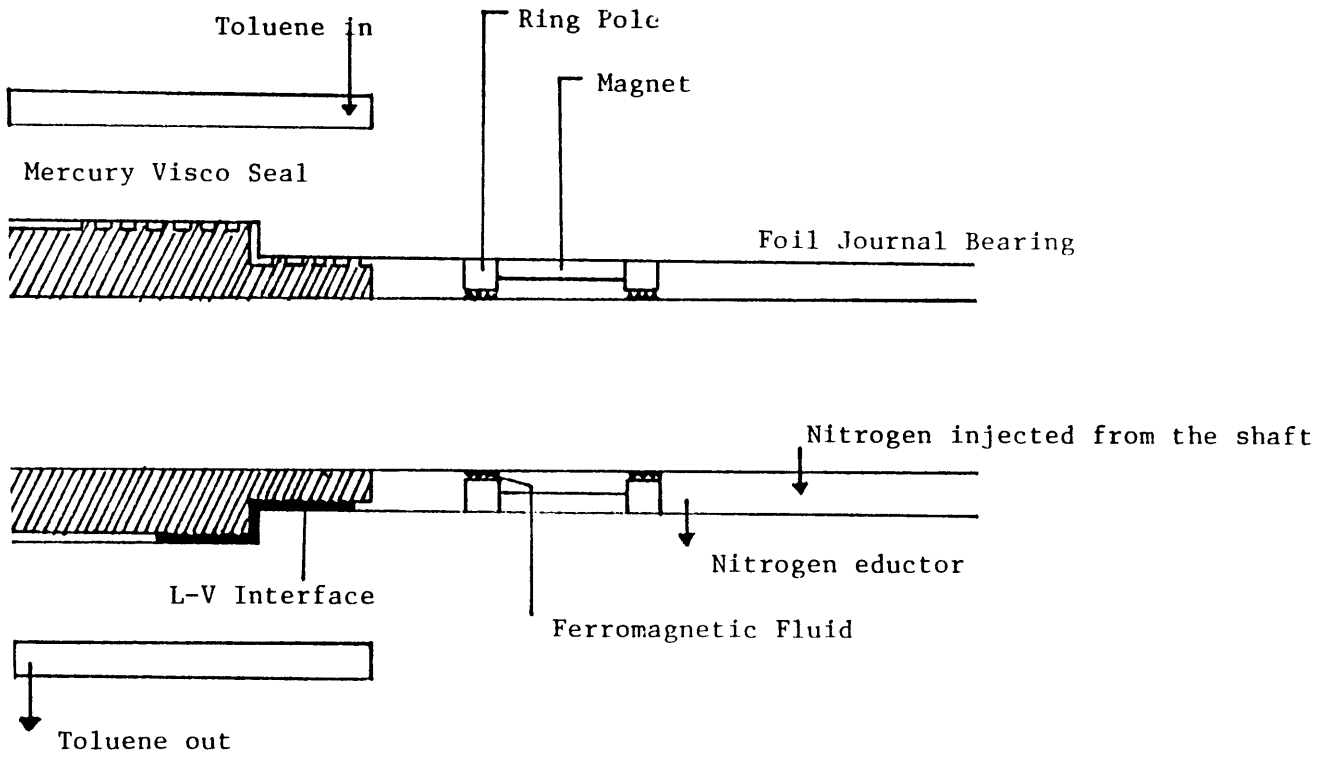
Figure 18: Visco Seal − Ferrofluidic Seal Combination
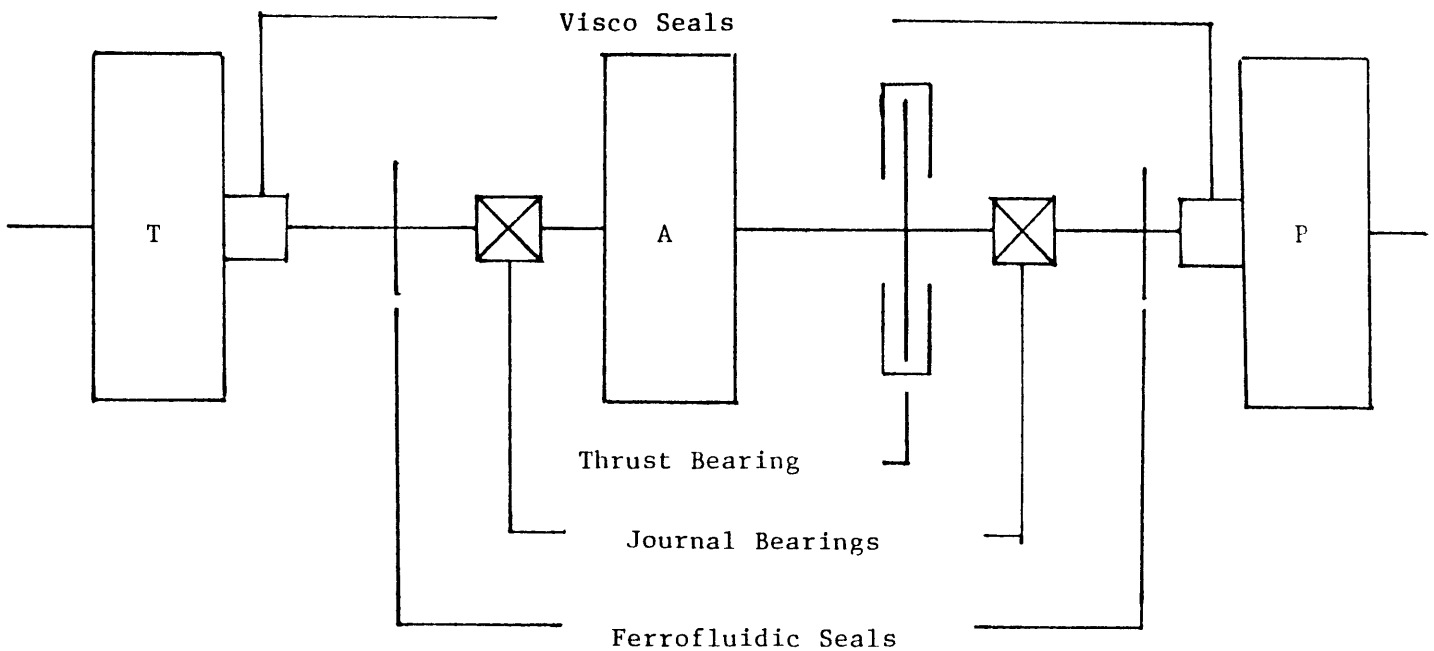
Figure 19: Turbine-Alternator-Pump Assembly

return pump

collector
trough

film

disk

nozzle

ω

support
structure

rotating platform

seal

z

Θ

r

heat exchanger
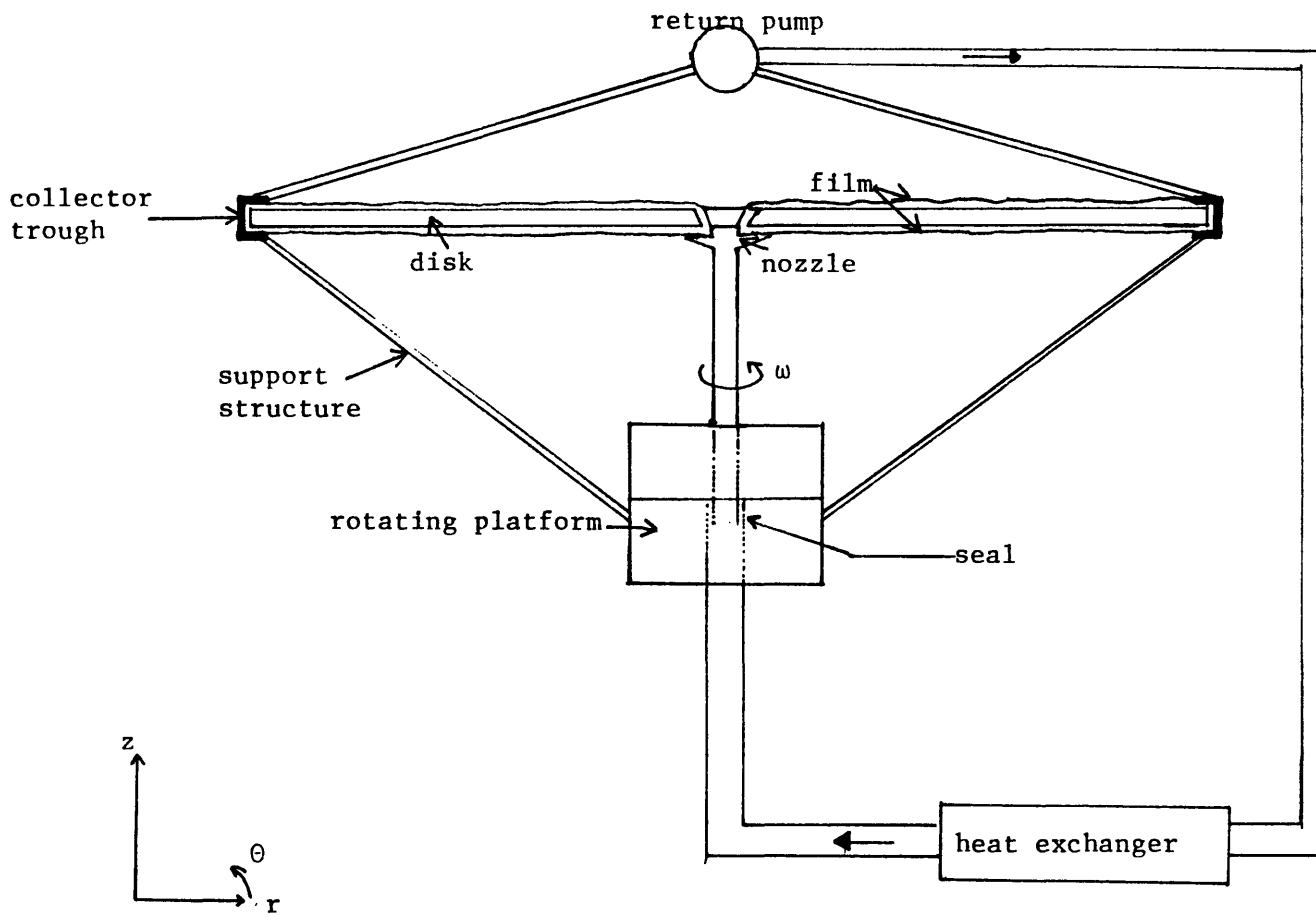
Figure 20: Rotating Film Radiator Schematic

to system

collector

condensate layer

nozzle

ω

rotating platform

vapor seal

from system
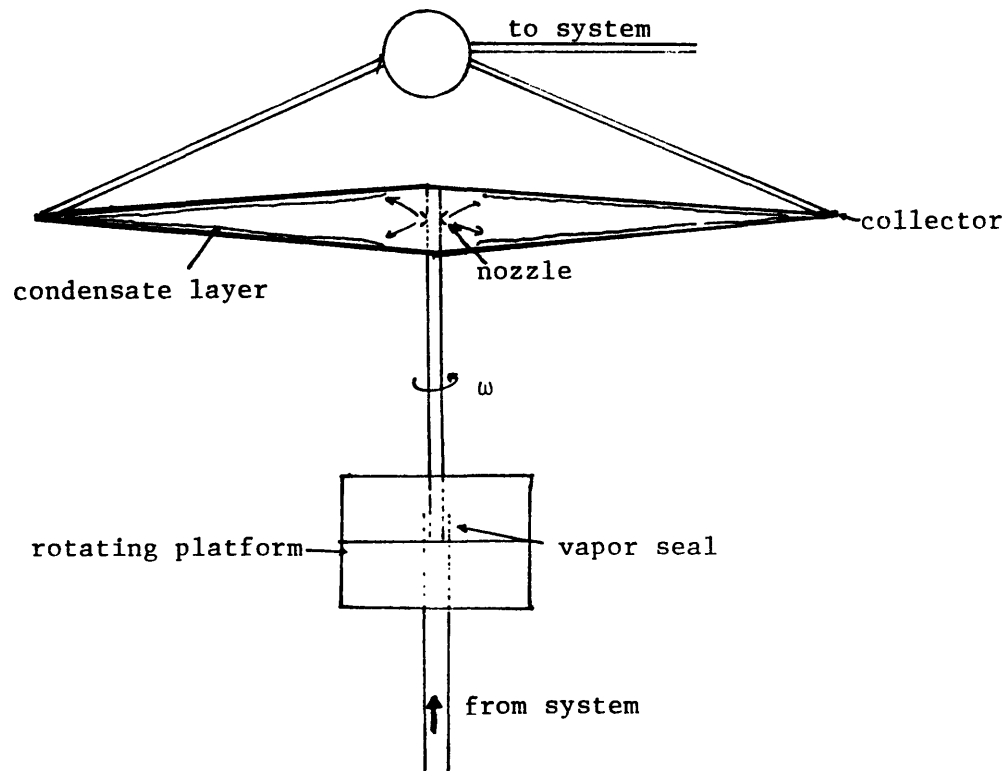
Figure 21: Rotating Bubblue Membrane Radiator Schematic

MASS VS ANGULAR VELOCITY
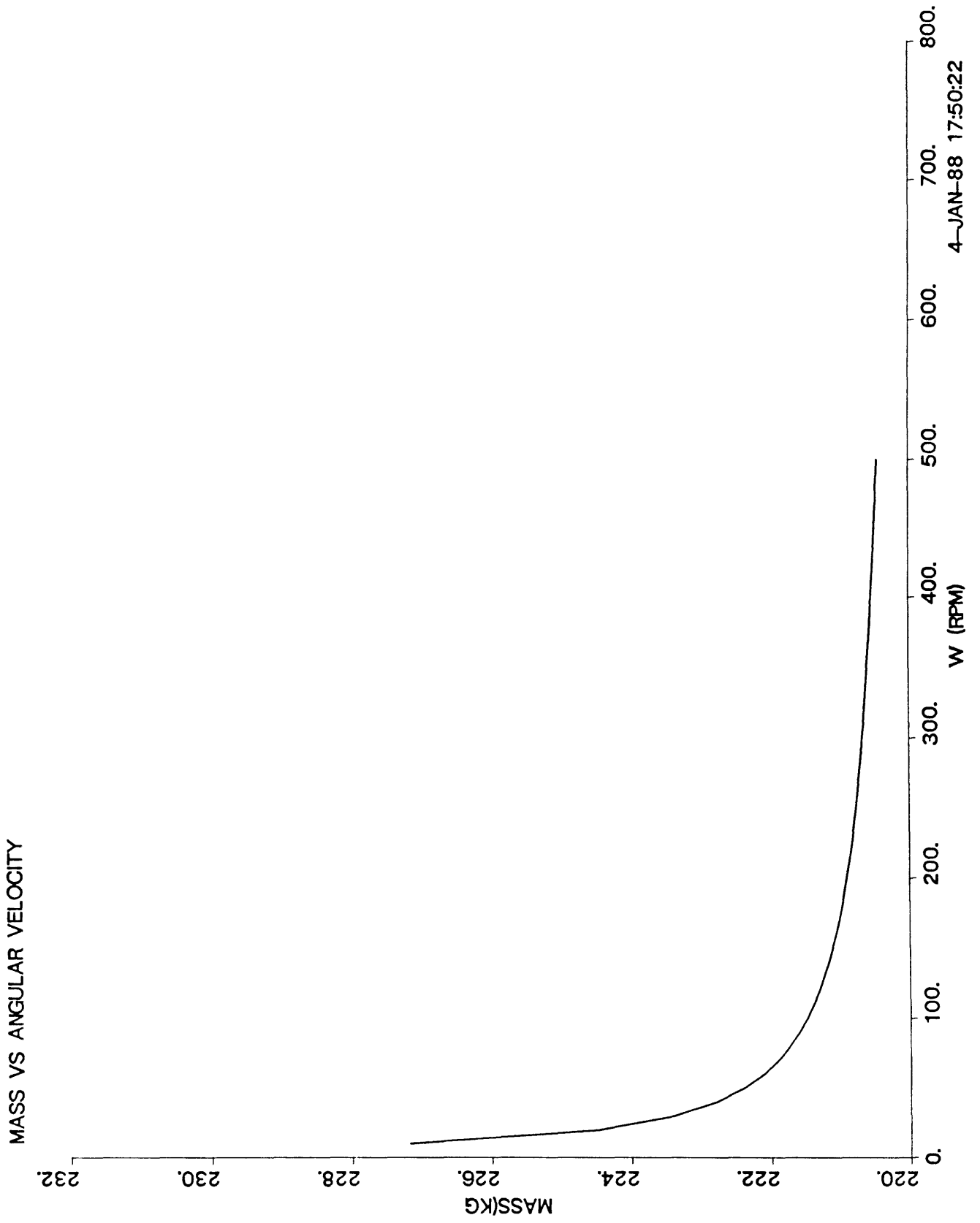
Figure 22 : RBMR Mass vs Rotational Speed
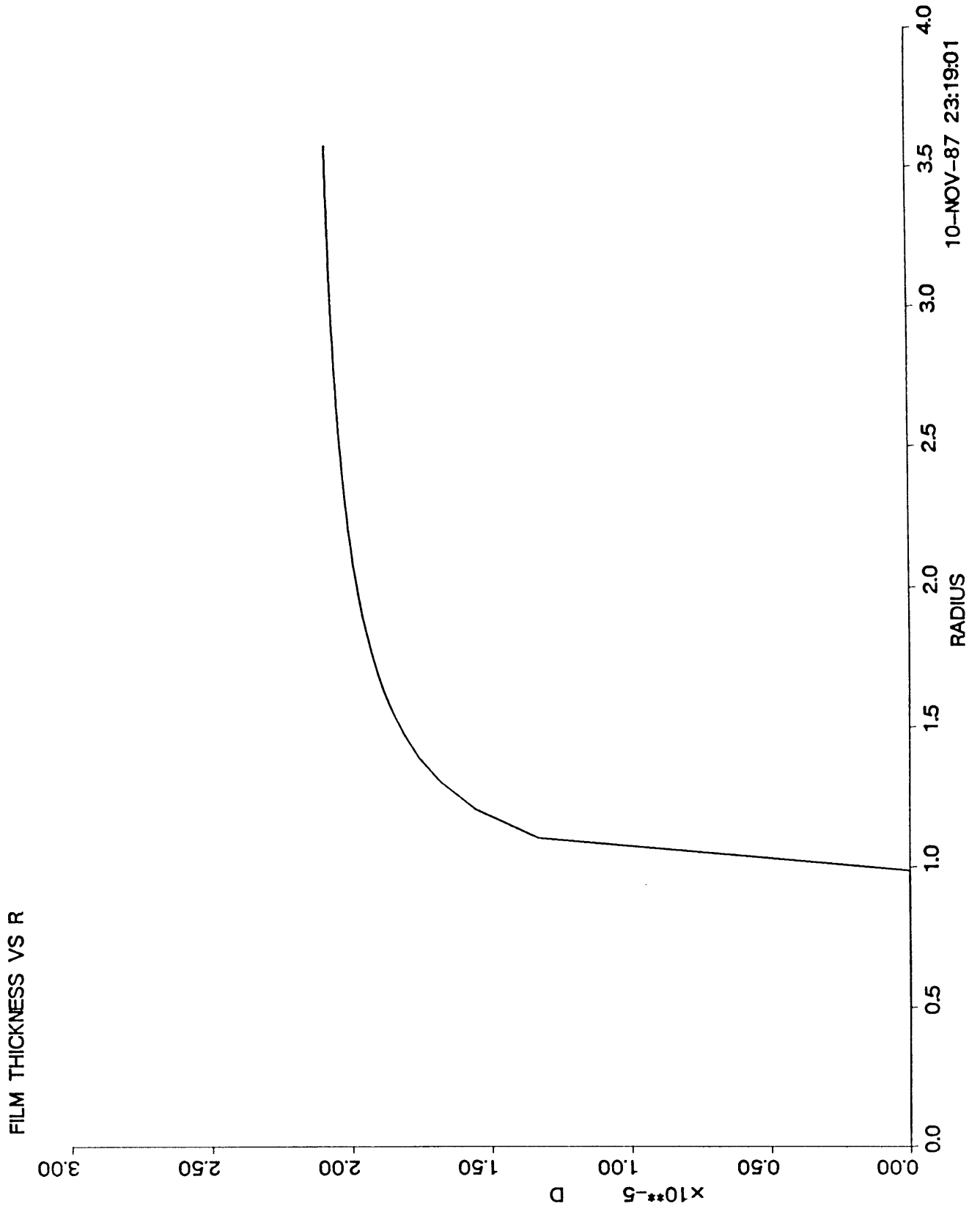
Figure 23 : Film Height vs Radius for RBMR
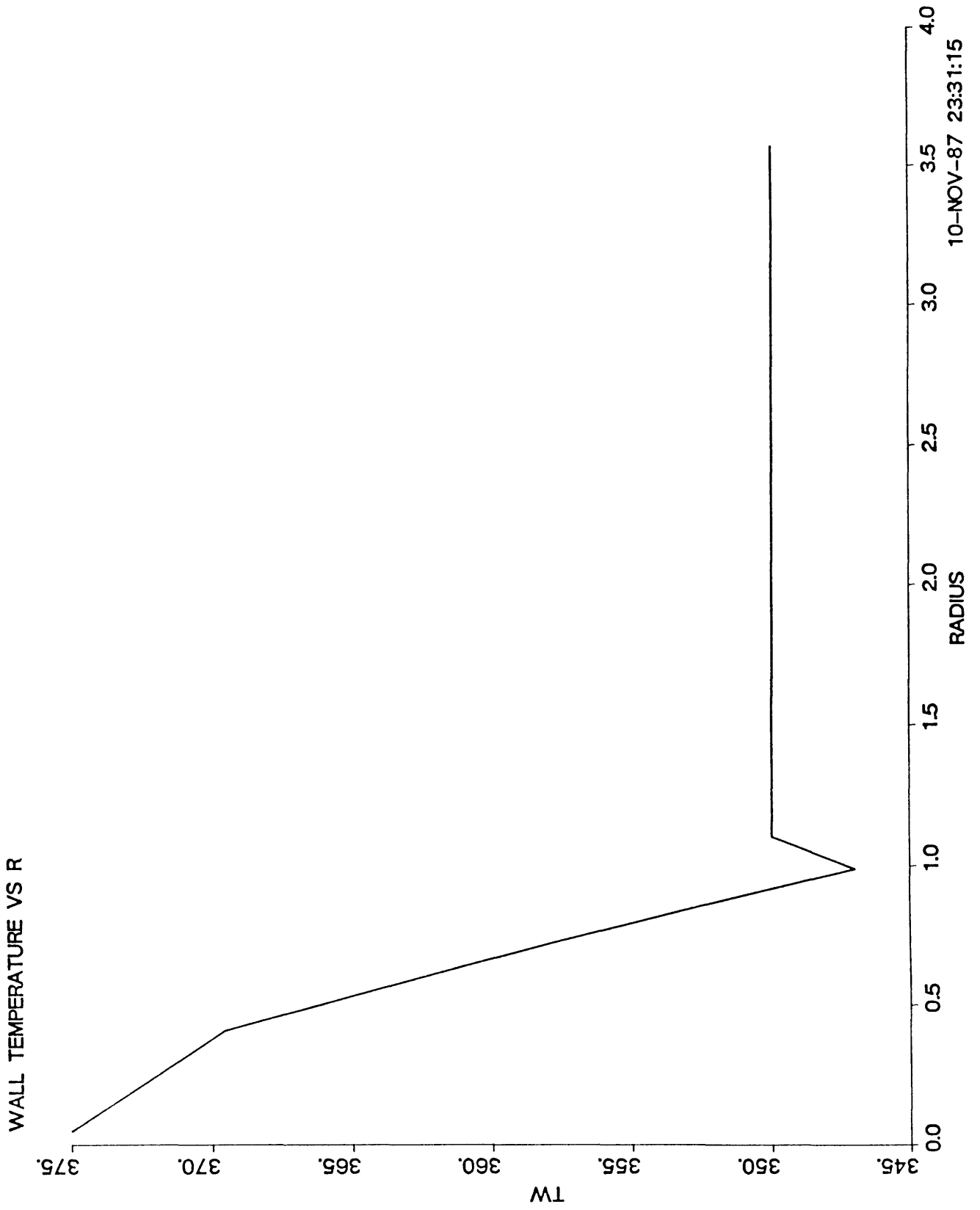
Figure 24 : Wall Temperature vs Radius for RBMR
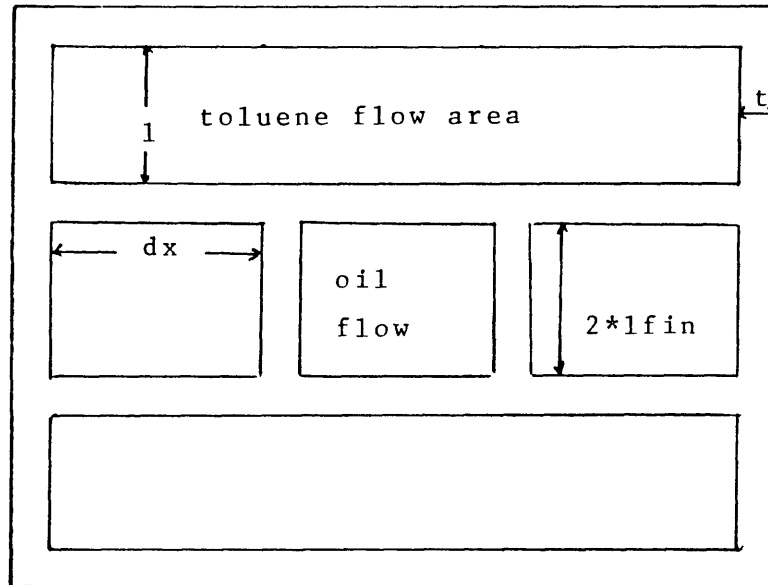
Figure 25: Heat Exchanger for Rotating Film Radiator

FILM THICKNESS VS. RADIUS
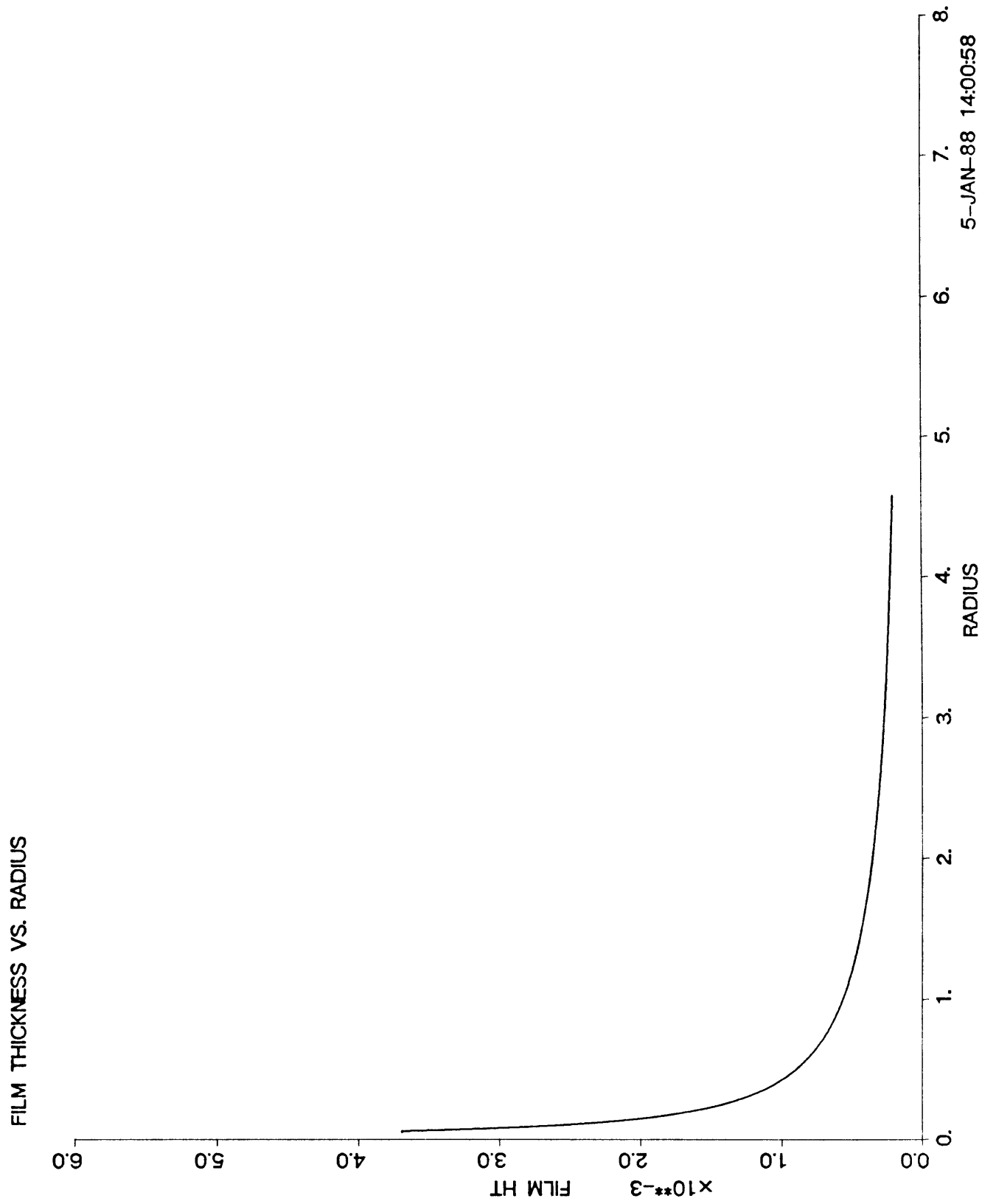
Figure 26: Film Height vs Radius for RFR

TEMPERATURE VS RADIUS
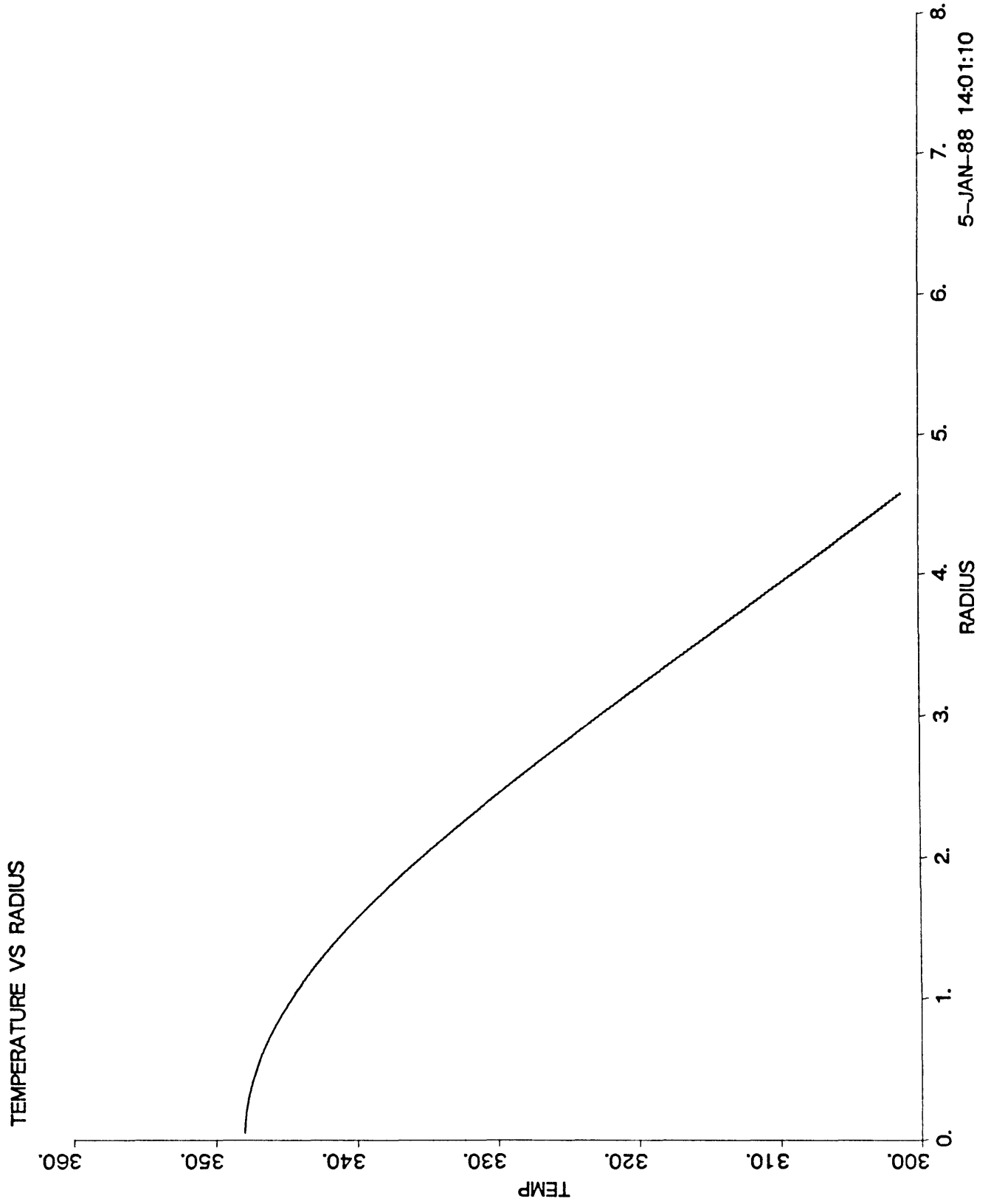
Figure 27: Film Temperautre vs Radius for RFR
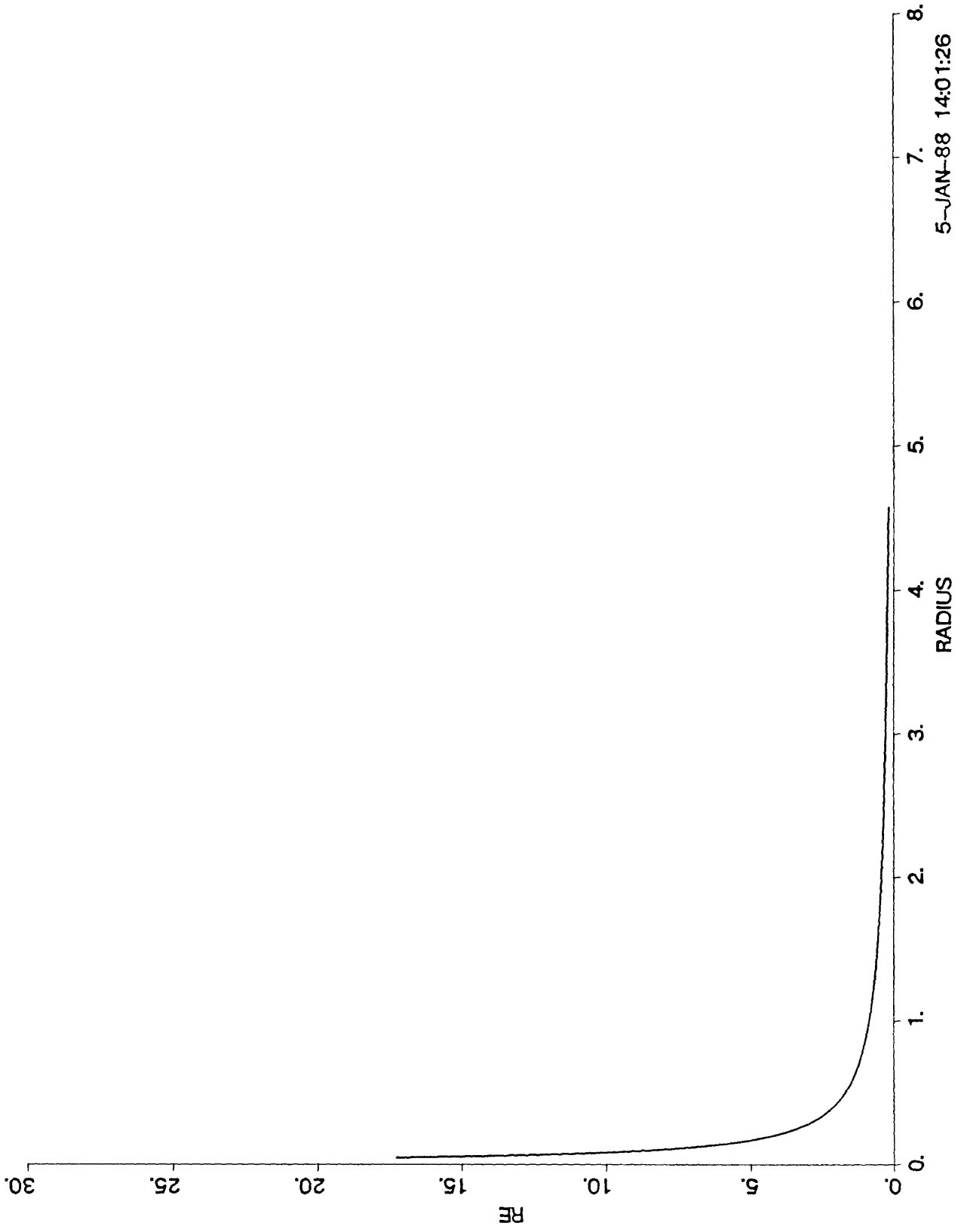
Figure 28: Reynolds Number vs Radius for RFR

TES

CONCEPT 1

HEAT PIPE

CONCEPT 2

TES

CONCEPT 3

TES
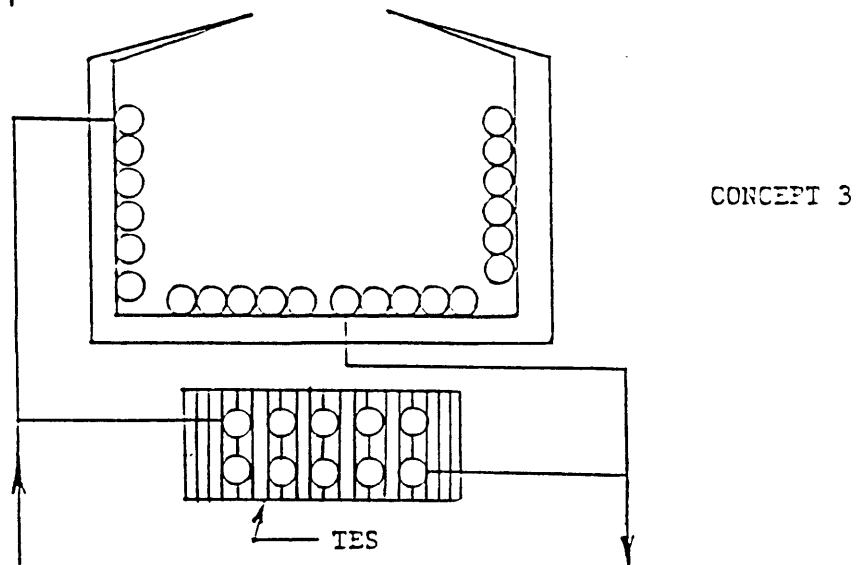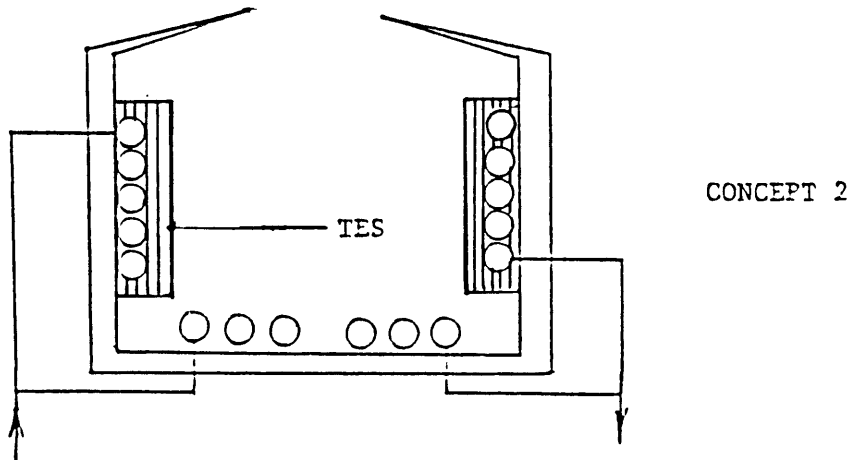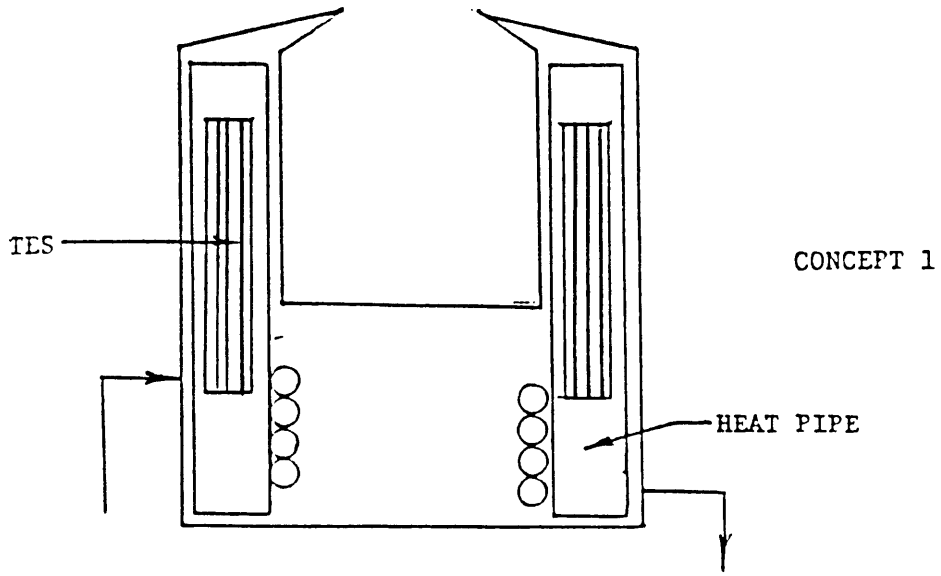
Figure 29: Receiver Concepts

Hg(1)

CONCEPT 4

TES (LiF)

Hg(v)

LiF/Li(c)

LiF/Li(h)

CONCEPT 5

Hg(1)

Hg(v)

TES (LiF/Li)

LiF/Li(c)

LiF/Li(h)

CONCEPT 6

Hg(1)

Hg(v)

TES (LiF/Li)

Heat Exchanger/Boiler

Hg(v)

Hg(1)

CONCEPT 7

Li(c)

Li(h)

TES (LiF/Li)

Li(cooled)

Heat Exchanger/Boiler

Hg(v)

Hg(1)

CONCEPT 8

Li(c)

Li(h)

Li(c)

Li(h)

Heat Exchanger/Boiler

Hg(1)

Hg(v)

INSOLATION

ECLIPSE
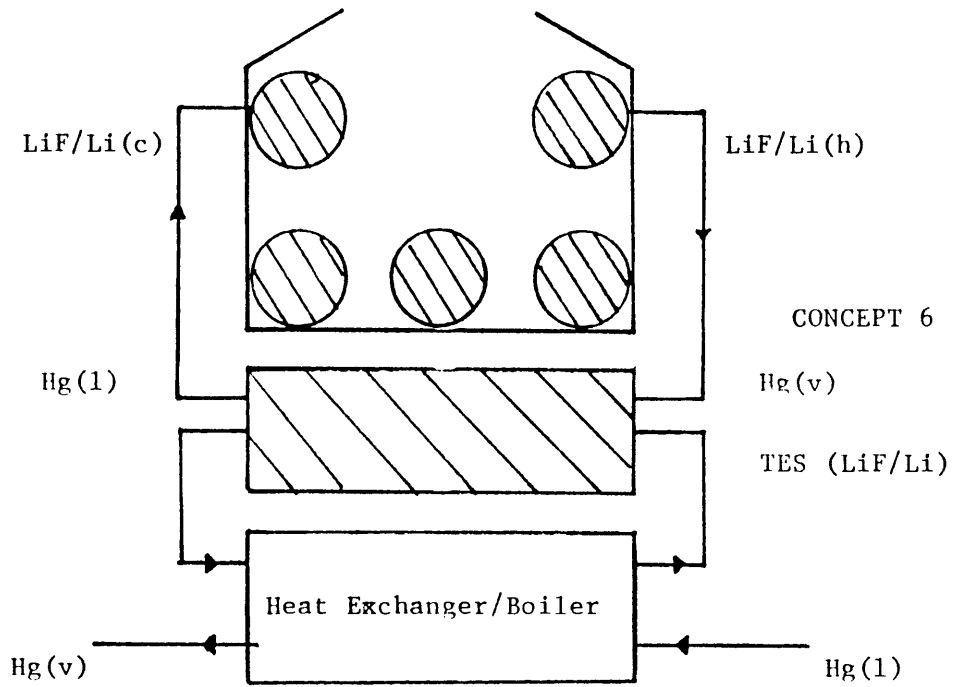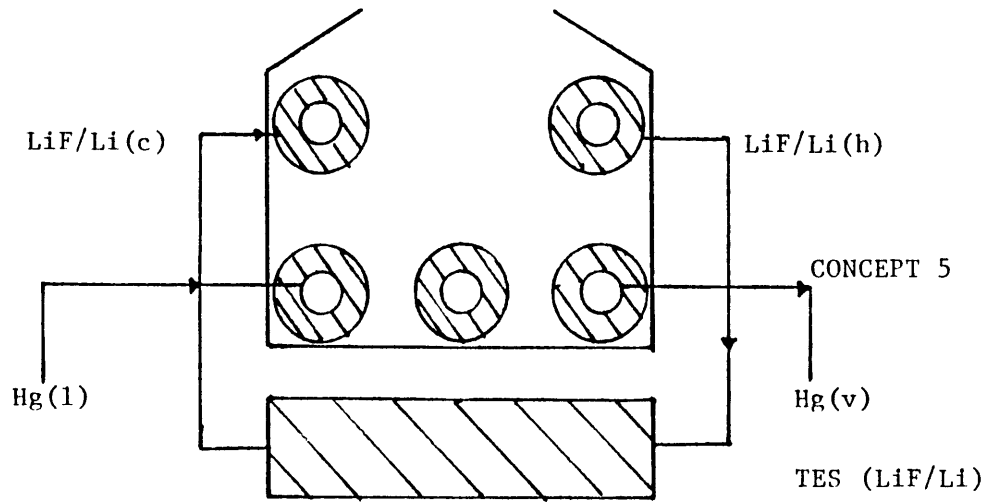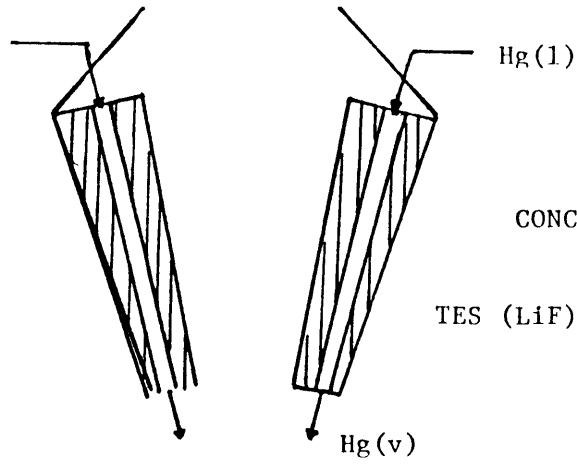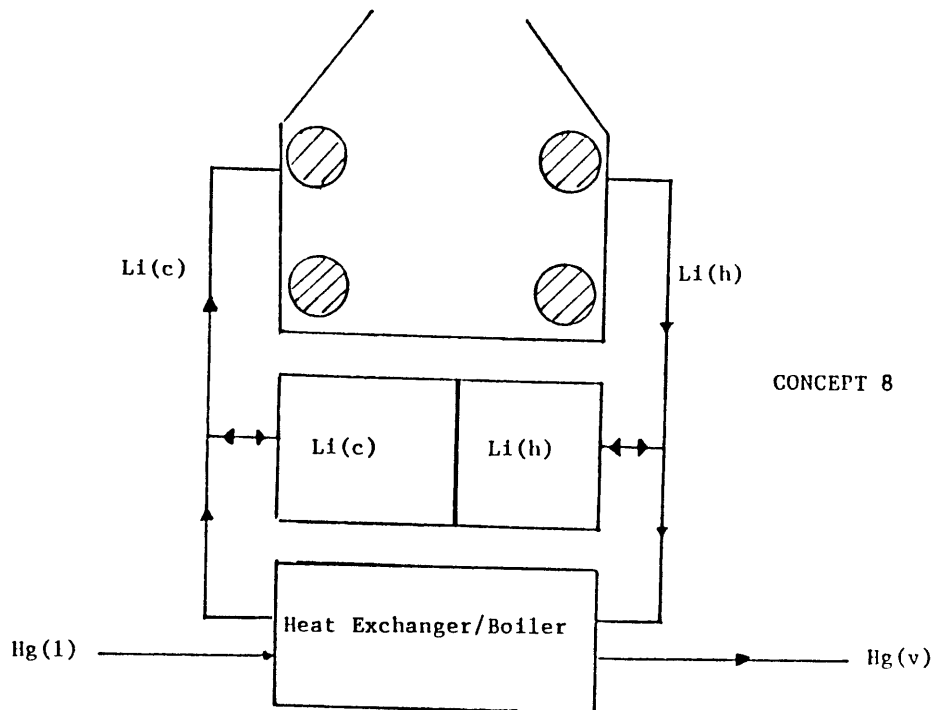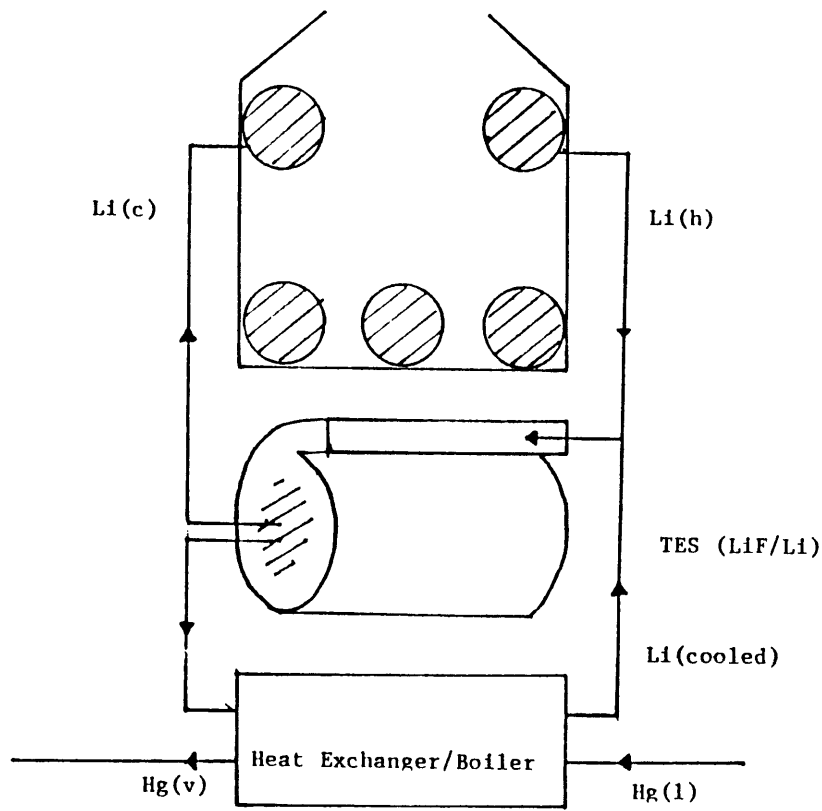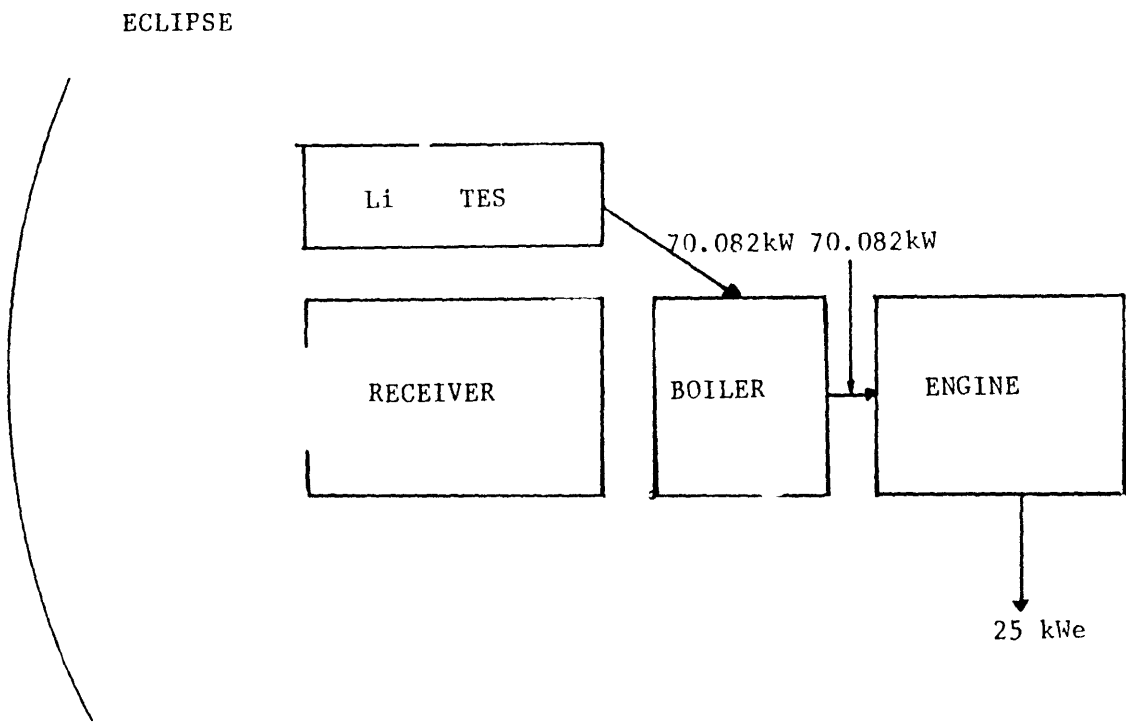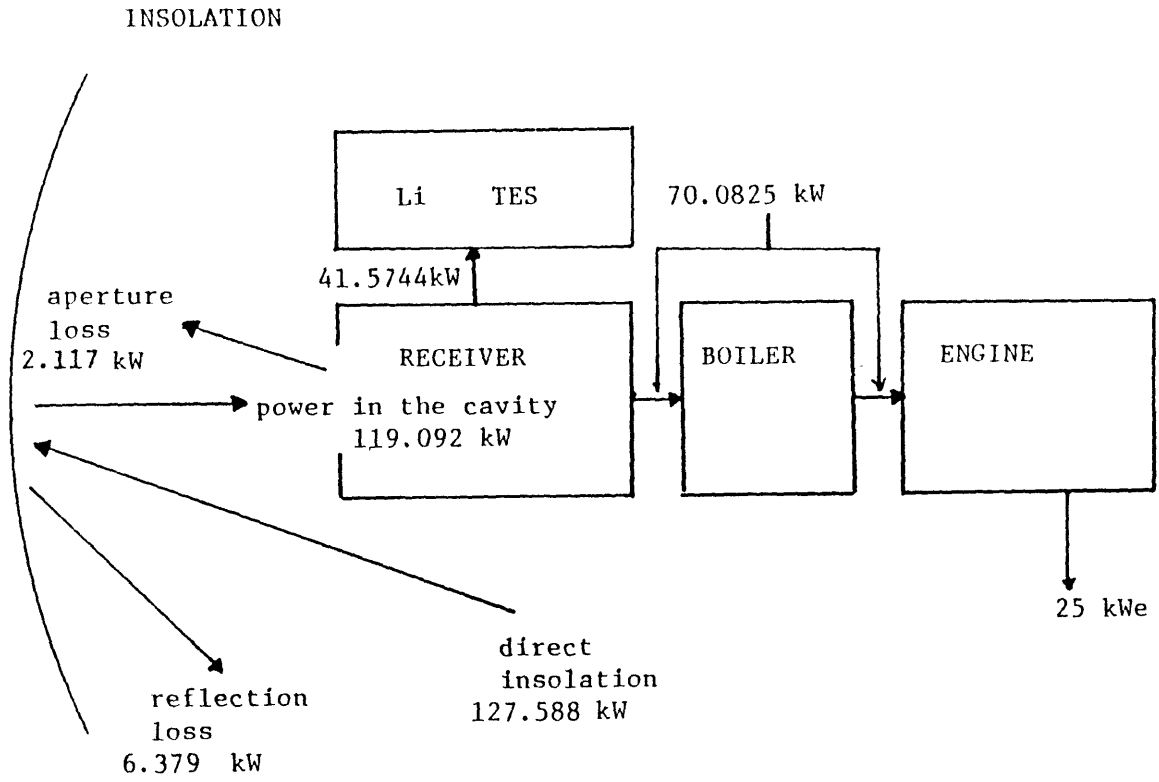
Figure 30 : Energy-flow Diagram for the final 8th concept design

Maximum Li Temperature = 1400 K
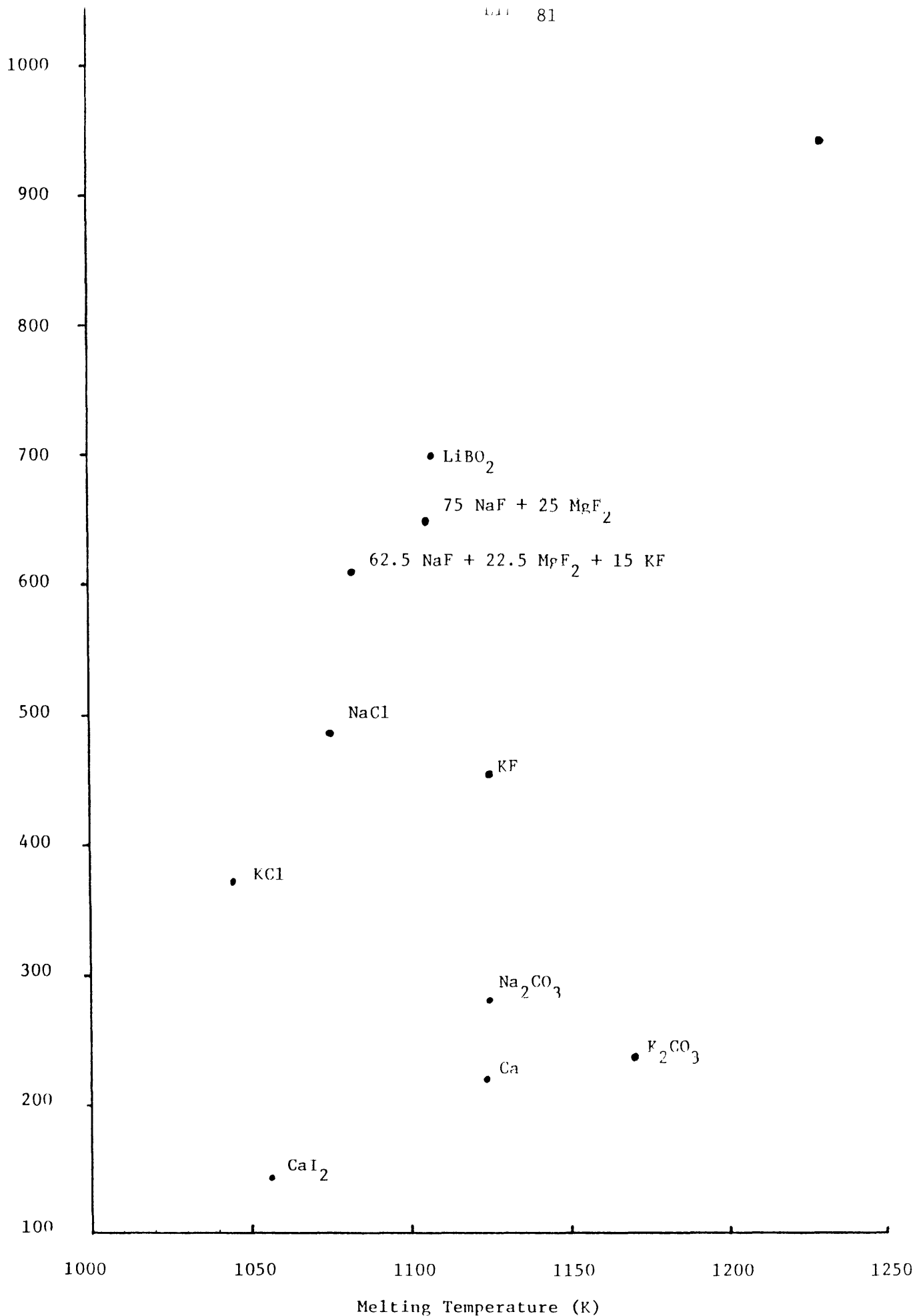
Figure 31 Heat of Fusion vs. Melting T of various PCMs
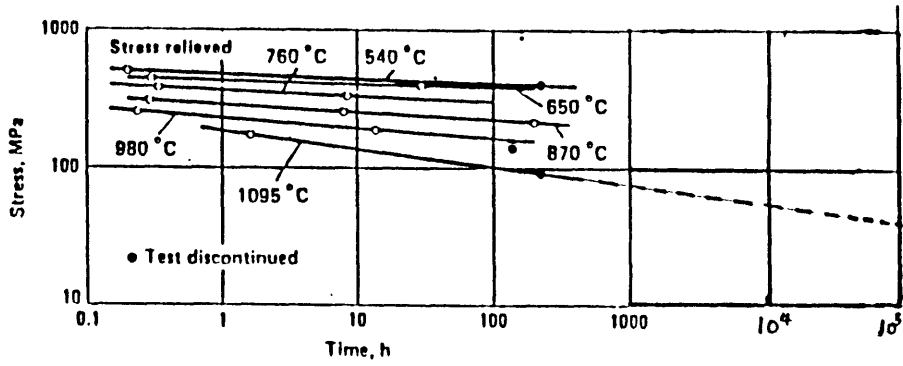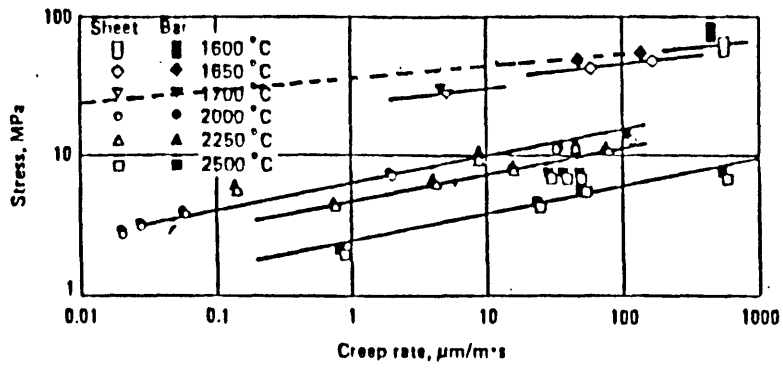
Figure 32 : Creep data of Molybdenum
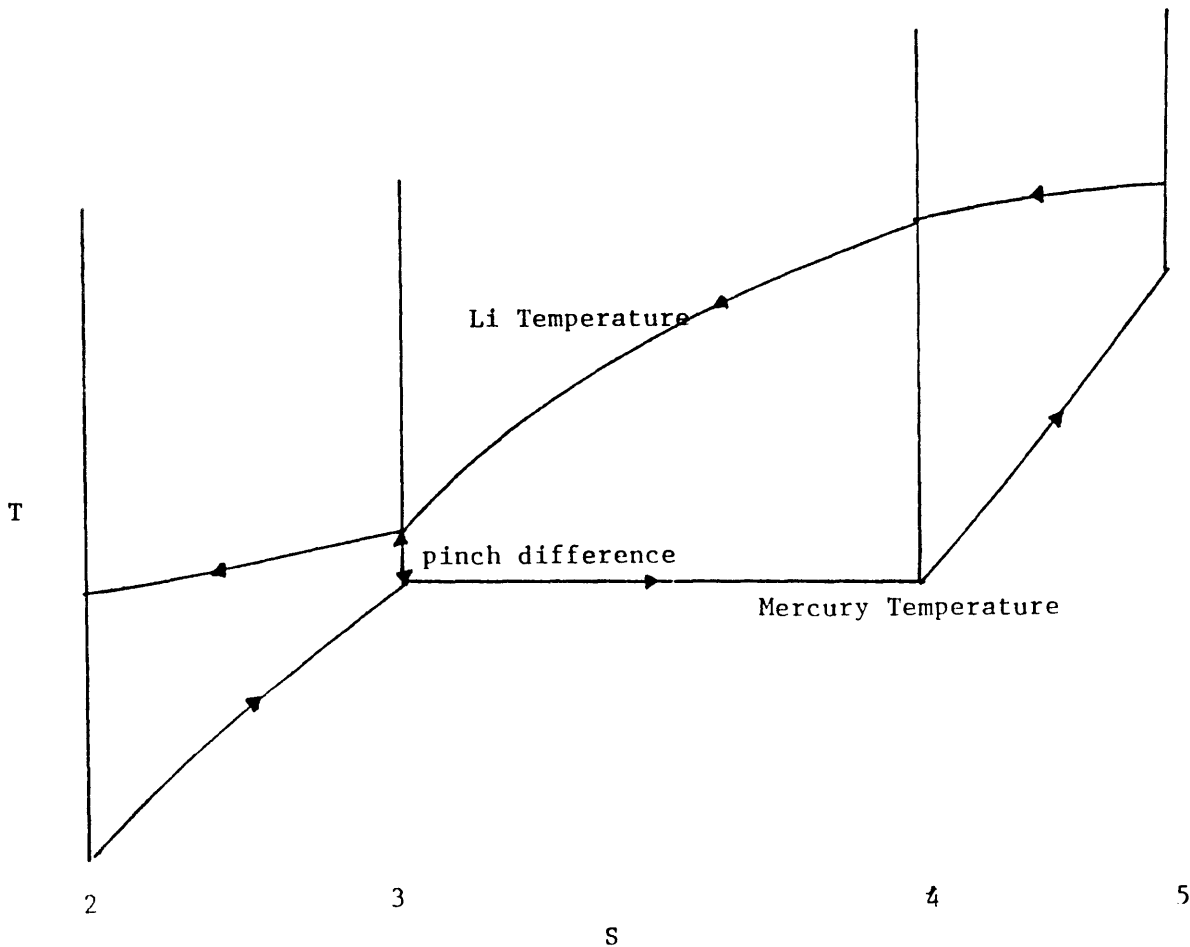
Figure 33 Heat Exchanger Temperature Profile
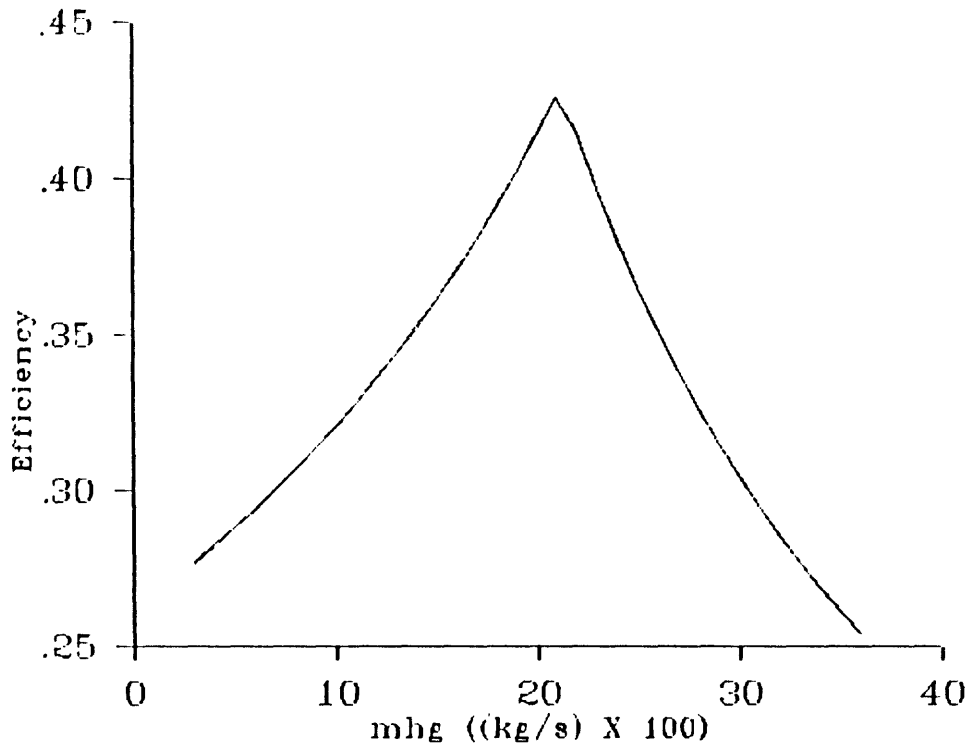
Figure 34 a: Overall Cycle Efficiency vs
Mercury Mass Flow Rate
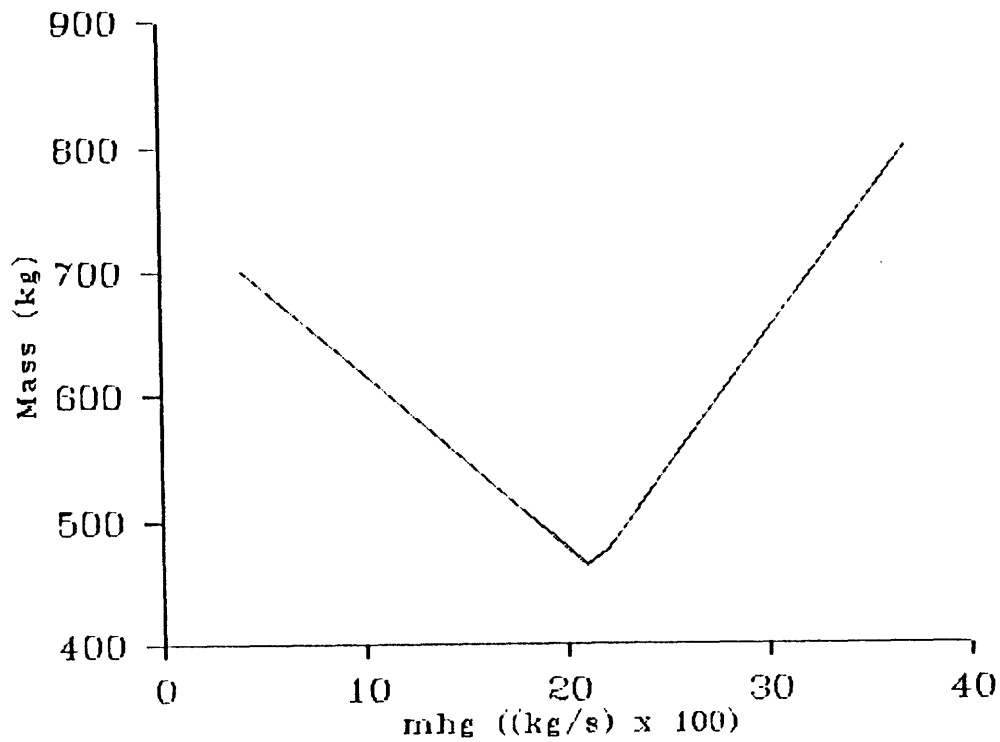
Figure 34 b: Overall Mass vs Mercury Mass Flow Rate
for Concept Two
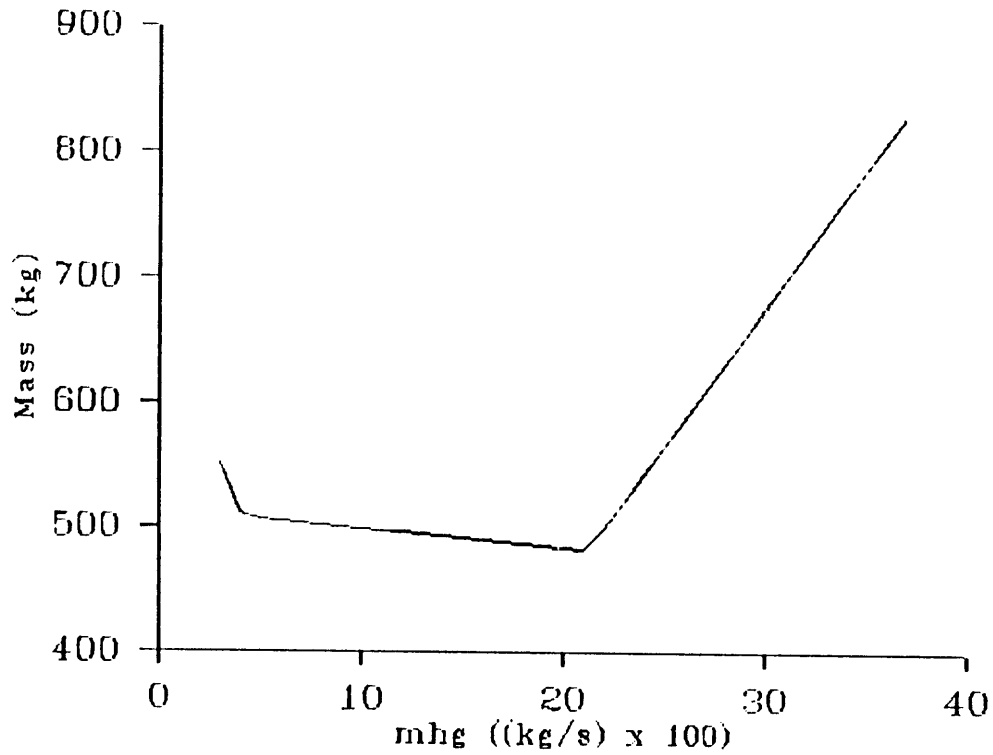
Figure 34 c: Overall Mass vs Mercury Mass Flow Rate
for Concept Eight with $T_{max\ Li}$ = 1255 K
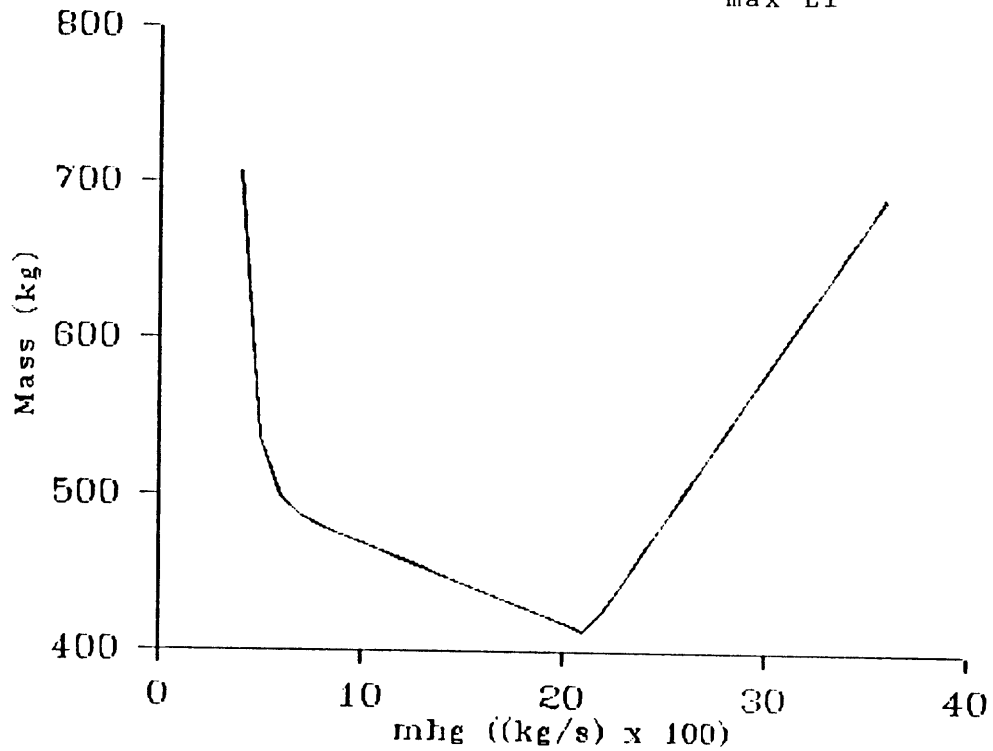
Figure 34d: Overall Mass vs Mercury Mass Flow Rate
for Concept Eight with $T_{max\ Li}$ =1400 K
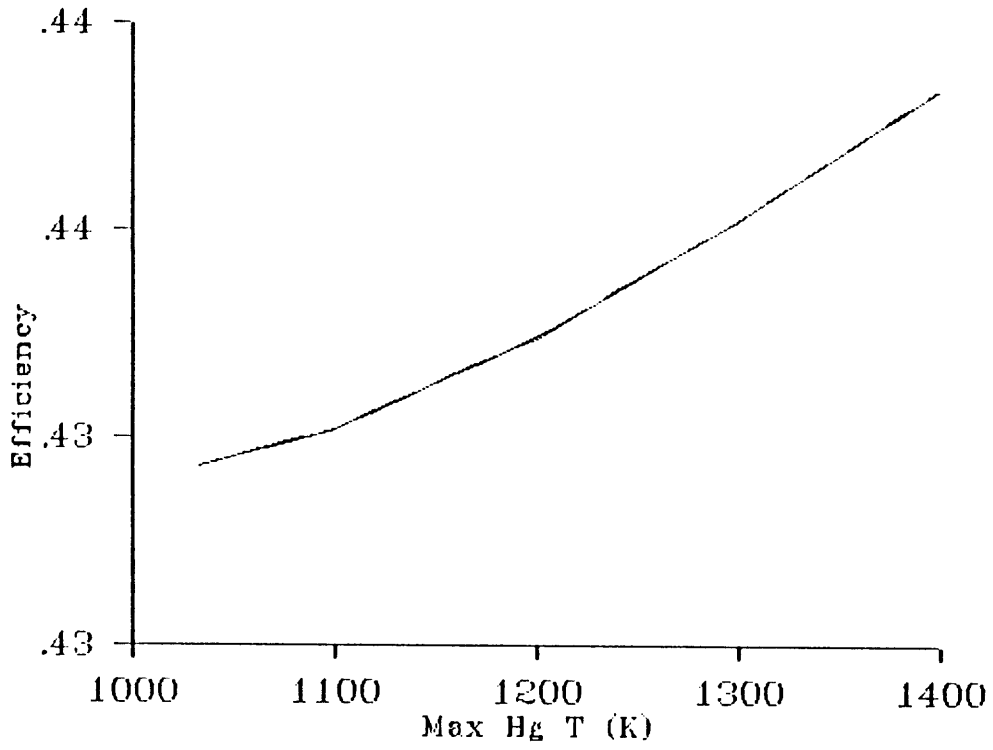
Figure 35 :Overall cycle efficiency vs Max Hg T

Max Li T = 1200 K

Concept 3 (LiF TES located outside the receiver)

Concept 2 (LiF TES located inside the receiver)

Max Li T = 1255 K

Max Li T = 1300 K

Max Li T = 1350 K

Max Li T = 1400 K

System Mass (kg)

Max Hg T (K)
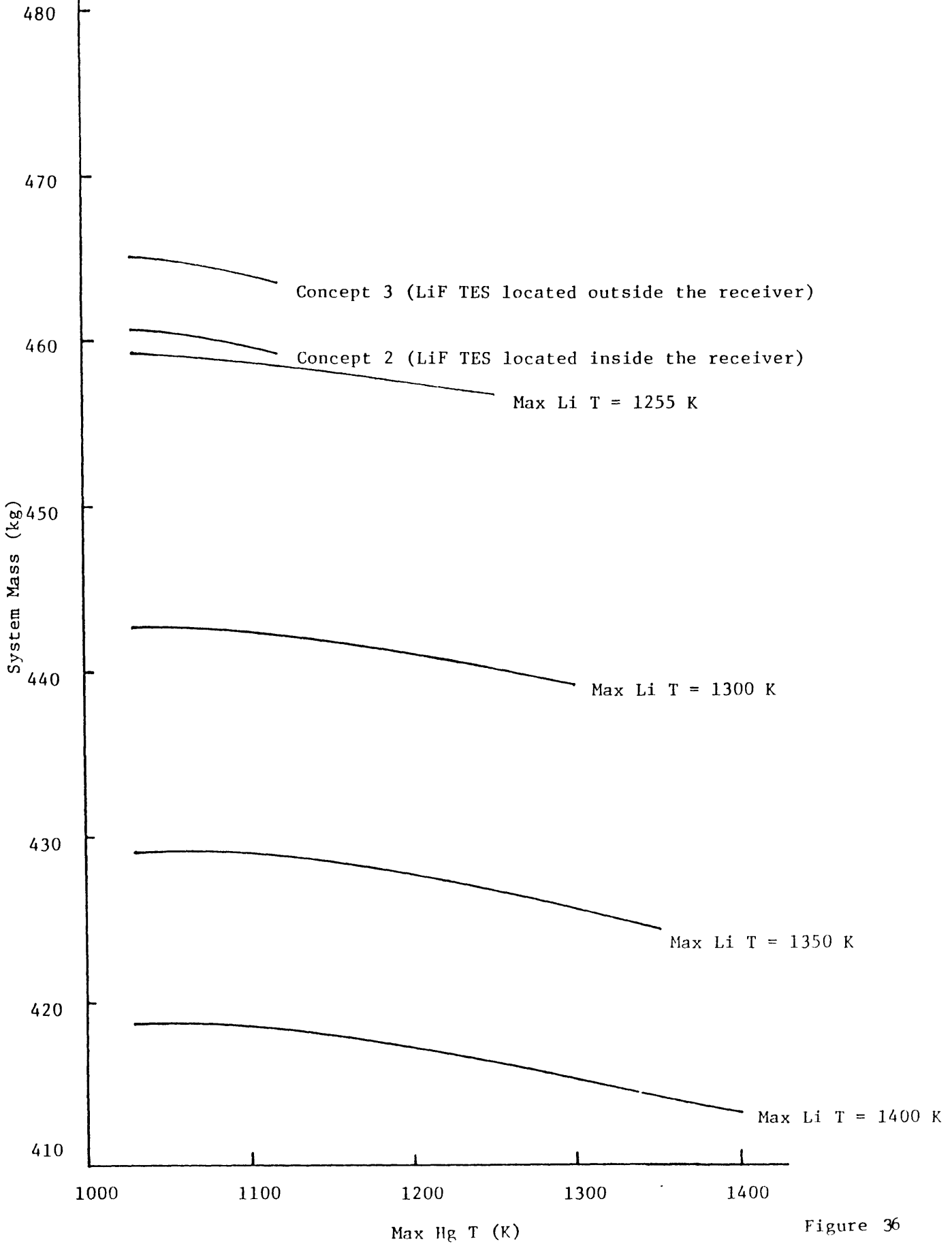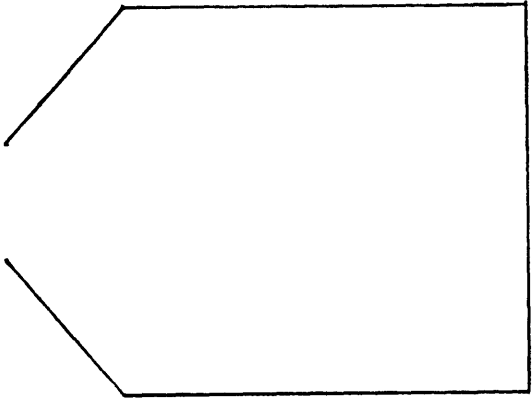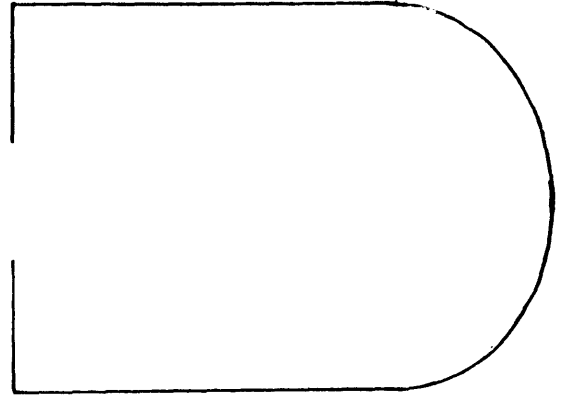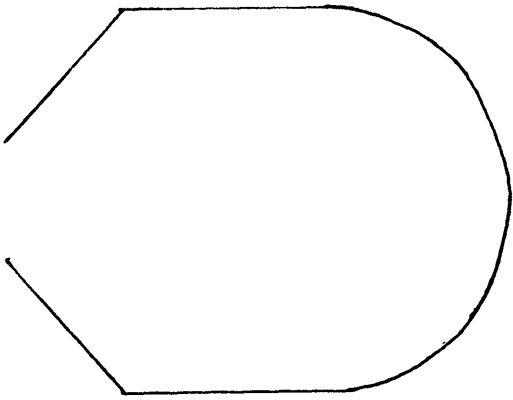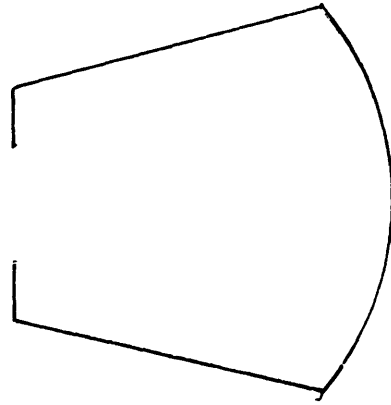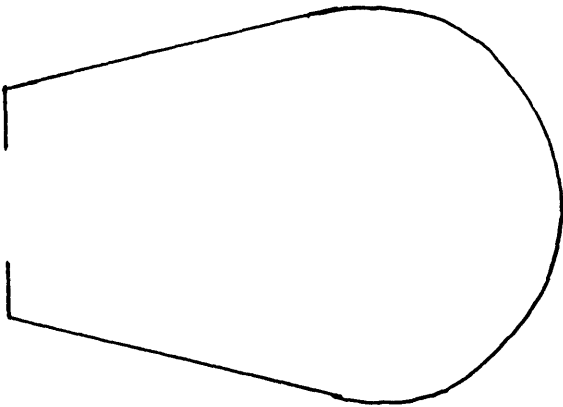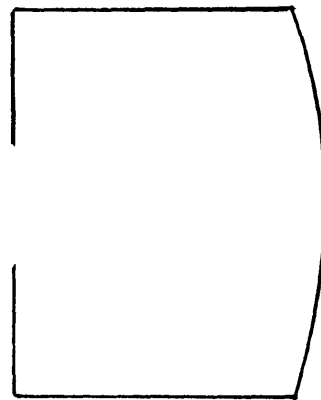
Figure 36

Figure 37: Different Receiver Geometries

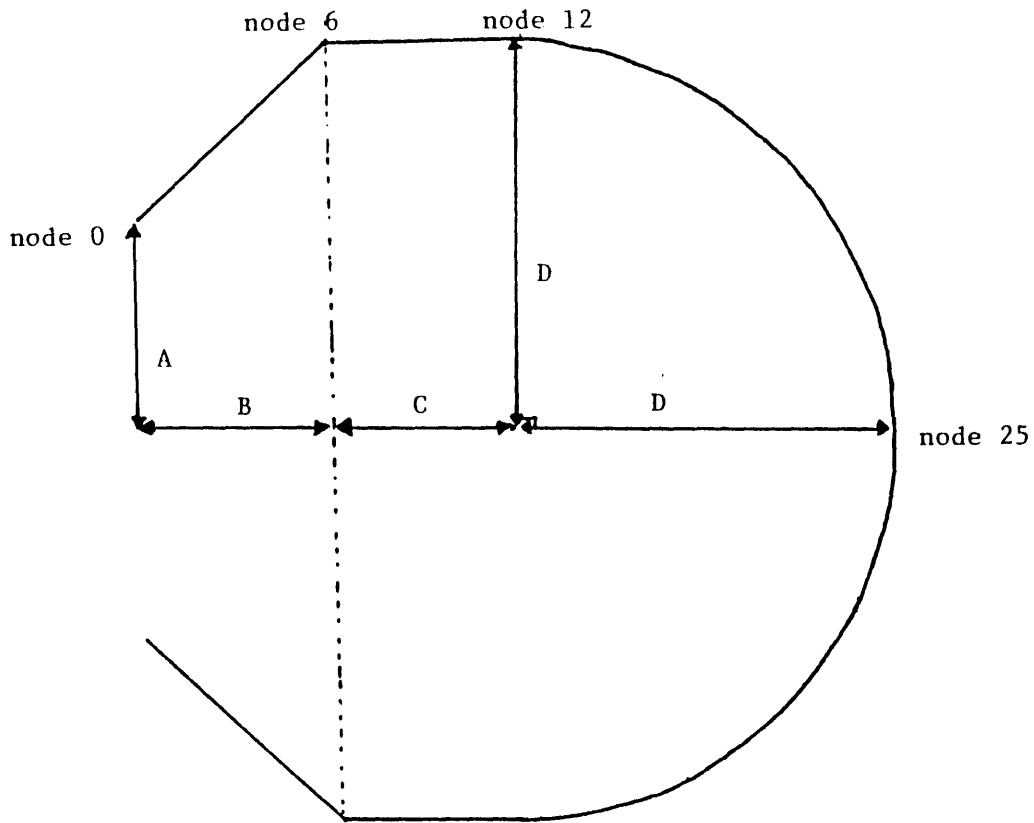0.002 m · thickness of Li flow donut area

radius of the inner shell

aperture radius

0.2 m

0.2 m

0.1 m

0.1 m

0.11 m

0.1 m
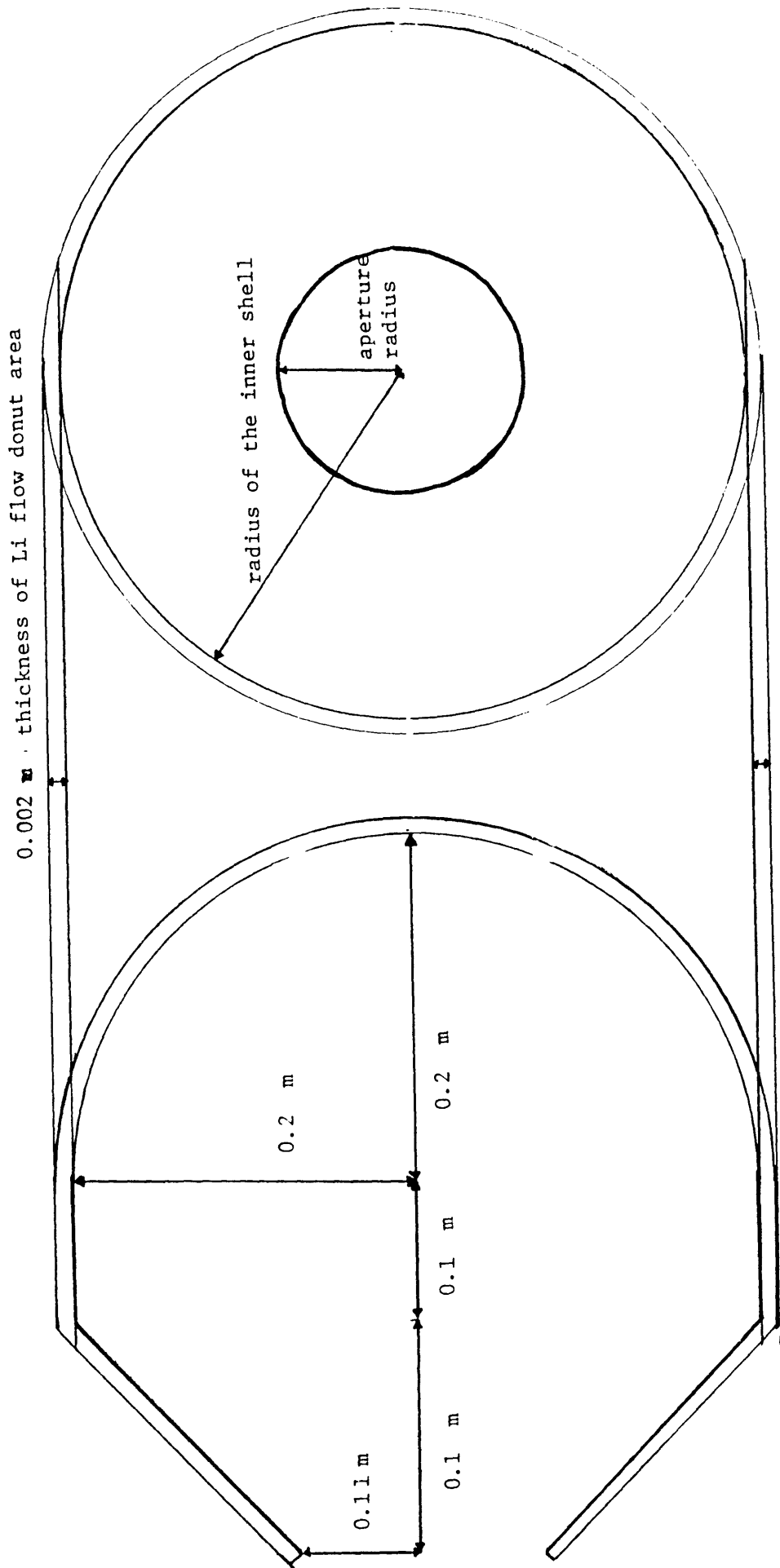
Figure 38 : Final Dimensions of the Recommended Receiver

Receiver Type C

Receiver	A	B	C	D
C1	0.1	0.075	0.075	0.15
C2	0.11	0.1	0.1	0.2
C3	0.11	0.17	0.08	0.25
C4	0.11	0.17	0.13	0.28

the dimensions in meters

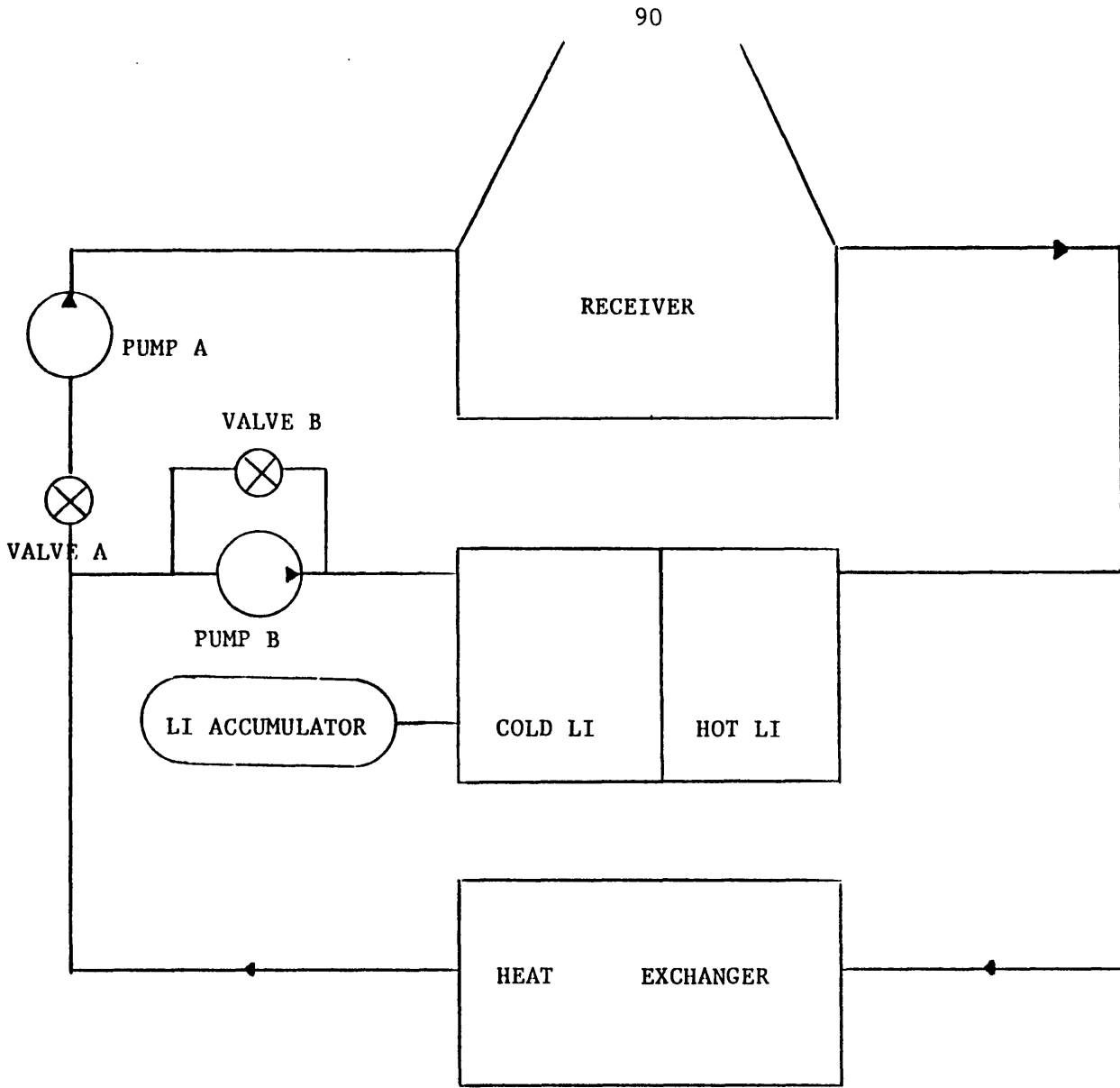Figure 39: Trial Receiver Sizes of Type C

Figure 40:   Li loop configuration with the Li accumulator

Appendices

<div align="center">Appendix A</div>

The shear stress in rz direction (Figure 20) is expressed by (A.1).

$$\tau_{rz} = \mu \left(\frac{\delta V_r}{\delta z} + \frac{\delta V_z}{\delta r}\right) + \tau_g \tag{A.1}$$

Neglecting V_z, τ_g, and ρ_g, equation (A.1) was simplified to equation (A.2) where the gravity term g is a function of the rotational speed.

$$\mu\left(\frac{\delta V_r}{\delta z}\right) = \rho g(\delta - z) \tag{A.2}$$

$$g = r\omega^2 \tag{A.3}$$

V_r expression was derived by integrating equation (A.2)

$$V_r = \int_0^\delta \frac{\rho g}{\mu}(\delta - z)dz \tag{A.4}$$

Since the condensate mass flow rate can be expressed by (A.5).

$$m_{tol\,per\,side}(r) = \int_0^\delta 2\pi r \rho V_r dz \tag{A.5}$$

the film height δ for a given condensate mass flow rate was determined by substituting for V_r and integrating equation (A.5)

$$\delta(r) = \sqrt[3]{\frac{3\mu m_{tol\,per\,side}}{2\pi r^2 \rho^2 \omega^2}} \tag{A.6}$$

Then

$$h(r) = \frac{k}{\delta} \tag{A.7}$$

Next the energy balance equation

$$h(T_{sat}-T_w)-\varepsilon\sigma(T_w^4-T_{space}^4) = q''_i - q''_o = 0 \qquad (A.8)$$

was solved for T_w by Newton-Raphson method for each segment. Then dQ, the amount of heat transferred, was determined for each segment.

$$dQ = m_{tol}C_p dT \text{ in vapor cooler} \qquad (A.9)$$

$$dQ = dm_{tol}h_{fg} \text{ in condenser} \qquad (A.10)$$

dT was 5 K and dm_{tol} was 2% of toluene mass flow rate per side. Since the inner radius r_i of the segment is known from the previous segment analysis, outer radius r_o was determined by equation (A.11).

$$r_o = \sqrt{r_i^2 + \frac{dQ}{q_o\pi}} \qquad (A.11)$$

The rotational speed and the number of container were varied to determine their effect on RBMR's total mass.

Appendix B: Mass Analysis for Varying m_{Hg}

Input: $Tmax_{Li}$

Assign: $Tpinch_{Li} = T_2$ in Figure 5 = 968 K

For each $\dot{m}_{Hg}$ from 0.03 to 0.38

B.1. η_{cycle} calculation

$$Power_{Hg} = 74.7831 \frac{kW}{(kg/s)} \dot{m}_{Hg}$$

$$Power_{toluene} = 30.08642 \text{ kW} - Power_{Hg}$$

$$\dot{m}_{toluene} = Power_{toluene} / 144.99 \text{ kW/(kg/s)}.$$

$$Q_{into\ toluene} = 554 \frac{kW}{(kg/s)} \dot{m}_{toluene}$$

$$Q_{out\ of\ Hg} = 254.834 \frac{kW}{(kg/s)} \dot{m}_{Hg}$$

if $Q_{into\ toluene} > Q_{out\ of\ Hg}$ **

$$\eta_{cycle} = \frac{30.08642}{\dot{m}_{Hg}\ (h_5 - h_2) + (Q_{into\ toluene} - Q_{out\ of\ Hg})}$$

else

$$\eta_{cycle} = \frac{30.08642}{\dot{m}_{Hg}\ (h_5 - h_2)}$$

** h_5 = Hg enthalpy @ 5 in Figure 4.

It was assumed that for $Q_{toluene} > Q_{Hg}$, Li will be used to provide the extra heat for toluene and that for $Q_{toluene} < Q_{Hg}$, an extra radiator would reject heat for the mercury cycle.

B.2. Li mass calculation

$$\dot{m}_{Li} = \frac{\dot{m}_{Hg}\ (h_5 - h_2)}{Cp_{Li}\ (Tmax_{Li} - T_{pinch})} = \frac{\dot{m}_{Hg}\ (h_5 - 79.2555)}{4.1612\ (Tmax_{Li} - T_{pinch})}$$

Li mass = $2100s \; \dot{m}_{Li}$

if $Q_{toluene} > Q_{Hg}$

$$T \; min_{Li} = 968 - \left(\frac{\dot{m}_{Hg} \; (h_3 - h_2) + Q_{toluene} - Q_{Hg}}{\dot{m}_{Li} \; Cp_{Li}} \right)$$

else

$$T \; min_{Li} = 968 - \left(\frac{\dot{m}_{Hg} \; (h_3 - h_2)}{\dot{m}_{Li} \; Cp_{Li}} \right)$$

B.3. Mirror Mass

$$\Phi = 1 - \left(\frac{2 \; sf^2 \; 5.67 \times 10^{-8} \; (T_{reciever}^4 - T_{sink}^4)}{I \; \rho \; G} \right)$$

$$CR = 1/(2 \; sf^2 \; \ln(\frac{1}{1-\Phi}))$$

$$\eta_{collector} = \rho \; G \; \Phi - \frac{5.67 \times 10^{-8} \; (T_{receiver}^4 - T_{sink}^4)}{I \; CR}$$

$sf^2 = 4.308 \times 10^{-5}$ for rim angle = 45°
pointing error = 0 mrad
slope error = 2 mrad
specularity error = 0.5 mrad
angular spread of sum = 0.0023 mrad

$$T_{receiver} = \text{Average Receiver Temperature} = \left[\frac{Tmax_{Li}^4 + Tmin_{Li}^4}{2} \right]^{0.25}$$

ρ = reflectivity = 0.95
G = shadow factor = 0.95
I = insolation density = 1330 W/m^2
Φ = intercept factor
CR = concentration ratio

Mirror Mass = Area of Mirror * Mirror Mass Density

$$= \frac{\left(\dfrac{30.08642}{\eta_{cycle}}\right)\left(1 + \dfrac{35}{59}\right)}{\left(1.33\right)\left(\eta_{collector}\right)} \quad \frac{3 \ kg}{m^2}$$

B.4. Heat Exchanger Mass

Heat Exchanger Mass = $0.017285 \dfrac{kg^2}{kJ}$ $(h_5 - h_2)$

B.5. Receiver Mass and Area

Receiver Mass = $0.237014 \dfrac{kg}{kWt} \left(\dfrac{30.08642}{\eta_{cycle}}\right)$

Receiver Area = $\dfrac{Receiver\ Mass}{(Mo\ density)(Receiver\ thickness)}$ = $\dfrac{Receiver\ Mass}{(10240)(0.002)}$

B.6. Li container mass and area

Li container volume = Li mass / Li density = Li mass / 534

Optimum container radius = $\left(\dfrac{Container\ volume}{2\pi}\right) 0.33333$

Minimum container area = $\left(\dfrac{2\ volume}{radius}\right) + (2\pi\ radius^2)$

Container mass = Container area (Mo density)(Container thickness)

= Container area (10240)(0.001).

B.7. Shielding mass equations [43]

(Receiver and Li container areas were input separately to calculate the shielding mass required for each)

Probability of no damage = 1 - NAT = 0.9

N = flux of meteorites
A = exposed area = receiver area, container area, or heat exchanger area
T = exposed time in seconds = 10 yr = 31536000 seconds

$$N = \frac{0.1}{31536000 \ (Area)}$$

$$\text{mass of meteorite} = \left[10^{\left[\frac{-14.37 - \log_{10}(N)}{1.213} \right]} \right] 10^{-3} \ kg$$

$$\text{shield thickness} = 4.25 \left(\frac{\rho_{meteorite}}{\rho_{Mo}} \right)^{1/3} \left(\frac{mass_{meteorite}}{\rho_{Mo}} \right)^{1/3} \left(\frac{V_{meteorite}}{V_t} \right)^{2/3}$$

$$\rho_{meteorite} = 4.4 \times 10^{-3} \ kg/m^3$$

$$V_t = 22 \ m/s$$

total shielding mass = (Mo density) [(Receiver Shield Thickness)(Receiver Area) + (Container Shield Thickness)(Container Area) + (Heat Exchnger Thickness)(Heat Exchanger Area)]

Total Mass =   Li Mass
               Mirror Mass
               Receiver Mass
               Li Container Mass
               Shielding Mass

B.8. Concept 2 Mass calculation

Total Mass = LiF Mass
             Mirror Mass (@ $T_{receiver}$ = 1121 K)
             Receiver Mass

B.9. Concept 3 Mass calculation

Total Mass = LiF Mass
                Mirror Mass (@ $T_{receiver}$ = 1121 K)
                Receiver Mass
                Insulation Mass

Appendix C: Mass Analysis for Varying T max$_{Hg}$

Input: T max Li

T max Hg (T_5)

C.1. $\dfrac{P_{out}}{\dot{m}_{Hg}}$, $\dfrac{Q_{out}}{\dot{m}_{Hg}}$ calculation

interpolate h_5 from Table in [44]

$$x_{6s} = \frac{(s_5 - s_f)}{(s_g - s_f)}$$ s_f, s_g found from Table in [44]

$h_{6s} = h_f + x_{6s} (h_g - h_f)$ h_f, h_g found from Table in [44]

$h_6 = h_5 + \eta_{turbine} (h_{6s} - h_5)$ $\eta_{turbine} = 0.75$

$x_6 = (h_6 - h_f) / (h_g - h_f)$

$s_6 = s_f + x(s_g - s_f)$

$$\frac{P_{out}}{\dot{m}_{Hg}} = (h_5 - h_6) - (h_2 - h_1)$$

$$\frac{Q_{out}}{\dot{m}_{Hg}} = 654 (S_6 - S_f) \qquad T_6 = T_1 = 654 \text{ K.}$$

C.2. Maximum η_{cycle} calculation

$$\dot{m}_{Hg} = \left(\frac{30.08642}{\dfrac{P_{out}}{\dot{m}_{Hg}} + \dfrac{144.99 \, Q_{out}/\dot{m}_{Hg}}{554}} \right)$$

$$Q_{out} \text{ of Hg} = \frac{P_{out}}{\dot{m}_{Hg}} \quad \dot{m}_{Hg}$$

$$P_{Hg} = \frac{P_{out}}{\dot{m}_{Hg}} \quad \dot{m}_{Hg}$$

$P_{toluene} = 30.08642 \text{ kW} - P_{Hg}$

$$\dot{m}_{toluene} = P_{toluene} \; / \; 144.99 \; kW/(kg/s)$$

$$Q_{into \; toluene} = 554 \; kW/(kg/s) \; \dot{m}_{toluene} = Q_{out \; of \; Hg}$$

$$\eta_{cycle} = \frac{P_{Hg} + P_{toluene}}{\dot{m}_{Hg} \; (h_5 - h_2)}$$

The rest of mass analysis C.3 - C.8 is the same as B.2 - B.7.

Appendix D

D.1 Separated Flow Model for $x < 0.88$

Total Mass Flow = G Area = $\dot{m}_{gas} + \dot{m}_{fluid}$ = GAx + GA (1-x)

$$G = \underbrace{Gx}_{G_{gas}} + \underbrace{G(1-x)}_{G_{fluid}}$$

$$Re_g = \frac{GxD}{\mu_g} \qquad\qquad Re_f = \frac{G(1-x)D}{\mu_f}$$

if $Re_g > 2000$ & $Re_f > 2000$

$$X_2 = \frac{Re_g^{0.2}}{Re_f^{0.2}} \left(\frac{GA(1-x)}{GAx}\right)^2 \frac{\rho_g}{\rho_f}$$

$$\phi_f^2 = 1 + \frac{20}{X} + \frac{1}{X^2}$$

if $Re_g > 2000$ & $Re_f < 2000$

$$X^2 = \frac{Re_g^{0.2}}{Re_f^{0.2}} \frac{16}{0.046} \left(\frac{GA(1-x)}{GAx}\right)^2 \frac{\rho_g}{\rho_f}$$

$$\phi_f^2 = 1 + \frac{12}{X} + \frac{1}{X^2}$$

if $Re_g < 2000$ & $Re_f > 2000$

$$X^2 = \frac{Re_g^{1.0}}{Re_f^{0.2}} \frac{0.046}{16} \left(\frac{GA(1-x)}{GAx}\right)^2 \frac{\rho_g}{\rho_f}$$

$$\Phi_f^2 = 1 + \frac{10}{X} + \frac{1}{X^2}$$

if $Re_g < 2000$ & $Re_f < 2000$

$$x^2 = \frac{Re_g^{1.0}}{Re_f} \quad \frac{16}{16} \quad \left(\frac{GA(1-x)}{GAx}\right)^2 \quad \frac{\rho_g}{\rho_f}$$

$$\Phi_f^2 = 1 + \frac{5}{X} + \frac{1}{X^2}$$

$$\left.\frac{dp}{dx}\right)_{2\ phase} = \left[\frac{2\ f_{fo}\ G^2\ v_f}{D}\right]\Phi_{fo}^2$$

f_{fo} = frictional factor of all if the massflow were in fluid phase

$$\Phi_{fo}^2 = \Phi_f^2 (1 - x)^{1.75}$$

D.2. Homogeneous Flow Model for $x > 0.88$

Assume $\frac{1}{\mu} = \frac{x}{\mu_g} + \frac{(1-x)}{\mu_f}$

$$\Phi_{fo}^2 = \left[1 + x\left(\frac{v_{fg}}{v_f}\right)\right]\left[1 + x\left(\frac{\mu_{fg}}{\mu_g}\right)\right]^{-0.25}$$

$$\left.\frac{dp}{dx}\right)_{2\ phase} = \left(\frac{2f_{fo}\ G^2\ v_f}{D}\right)\Phi_{fo}^2$$

D.3. f and g values of Hg @ 963 K

Property	Fluid (f)	Vapor (g)
$k\left(\dfrac{W}{mK}\right)$	14.53	16.61×10^{-3}
$Cp\left(\dfrac{J}{kgK}\right)$	147.2	100.9
$\mu\left(\dfrac{Ns}{m^2}\right)$	0.7416×10^{-3}	951.1×10^{-7}
$\rho\left(\dfrac{kg}{m^3}\right)$	11891	131.509
Pr	0.007513	0.5777

References

1. Fox, Allen G., "A Conceptual Study of Solar Power System Based on a Combined Mercury-Toluene Rankine Cycle," Masters Thesis, Department of Mechanical Engineering, M.I.T., Cambridge, MA, January, 1987.

2. Cotton, Randy M., "Design of a Condenser-Boiler for a Binary Mercury-Toluene Organic Rankine Cycle Solar Dynamic Space Power System," Masters Thesis, Department of Aeronautics and Astronautics, M.I.T., Cambridge, MA, June 1987.

3. Chaudoir, D.W., et al., "A Solar Dynamic ORC Power System for Space Station Application," Sundstrand Corporation, Rockford, IL, 1985.

4. Bisson, Edmond, "Lubrication & Bearing Problem in the Vacuum of Space," NASA Lewis Research Center.

5. Geary, P. J., Fluid Film Bearings, British Scientific Instrument Research Association, London, 1962.

6. Houghton, P. S., Ball and Roller Bearings, Applied Science Publisher LTD., London, 1976.

7. Grassam, N. S., and Powell, J. W., Editors, Gas Lubricated Bearings, Butterworth & Co., LTD., London, 1964.

8. Dunn, J. H., "Inspection of 2 BRU After Extensive Endurance Testing," NASA N77-17563, 1977.

9. Frost, A. et al., "High Performance TA & Associated Hardware Volume II - Design of Gas Bearings," NASA CR-1291.

10. Dobler, F. X. et al., "Mini-BRU BIPS Foil Bearing Development Progress Report," NASA N79-11407, 1979.

11. Barnett, M. A. et al., "Application of Air Bearings to High Speed Turbomachine," SAE 700720, 1970.

12. Licht, L. et al., "Gas-Lubricated Foil Bearings for High Speed Turboalternator - Construction and Performance," Paper No. 73-LUB-5, ASLE-ASME Joint Lubrication Conference, Atlanta, GA, October 14-18, 1973.

13. English, Robert E., "Power Generation from Nuclear Reactors in Aerospace Application," NASA TM 83342, 1982.

14. Gross, William., Editor, Fluid Film Lubrication, John Wiley & Sons Inc., New York, 1980.

15. A note from R. Niggemann, Sundstrand Corporation, to Professor J. F. Louis, Department of Aeronautics and Astronautics, M.I.T.

16. Song, S. J. and Louis, J. F., "Assessment of Seals for the Mercury Cycle," Department of Aeronautics and Astronautics, M.I.T.

17. Kruchowy et al., "Performance of a Turboalternator Gas-Bearing System at Steady-State Condition," NASA TN D-5542, 1969.

18. Warring, R. H., Seals and Sealing Handbook, First Edition, Gulf Publishing Company, Houston, 1981.

19. Charles, S. W. et al., "Ferromagnetic Liquids," in Ferromagnetic Materials, Volume II, North-Holland Publishing Company, Amsterdam, 1980.

20. Lessley, R. L. et al., "SNAP-8 Seals-to Space Development Test Program, Volume IV: Integrated Seal Simulator," NASA N65-17273.

21. Cherry, M. G., "Mechanical Evaluation of TAA 5/4 After 10,823 Hours of Operation in PCS-1", NASA N71-38251.

22. McHugh, J. D., "Dyanamic Seal", US Patent 3,097,853, July 16, 1963.

23. Mizumoto, M. et al., "Development of a Centrifugal Magnetic Liquid Seal for Super Conducting Generator," Paper G4, 9th International Conference on Fluid Sealing, 1978.

24. Begg, Lester L. et al., "Comparison of High Temperature Heat Rejection Concepts to System-Related Requirement," IECEC 879286, 1987.

25. Feig, J., "Radiator Concepts for High Power Systems in Space," AIAA-84-0055, 1984.

26. Carlson, Albert, et al., "Solar Dynamic Space Power System Heat Rejection," IECEC 869476, 1986.

27. Metals Handbook, 9th Ed., American Society for Metals, Metals Park, Ohio, 1980.

28. Webb, B.J., et al., "Rotating Bubble Membrane Radiator for Space Applications," IECEC 869426, 1986.

29. Sparrow, E. M., et al., "A Theory of Rotating Condensation," Journal of Heat Transfer, May 1959.

30. Sparrow, E. M., et al., "The Effect of Vapor Drag on Rotating Condensation," Journal of Heat Transfer, February 1960.

31. Mattick, A. T., et al., "Liquid Droplet Radiators for Heat Rejection in Space," IECEC 809477, 1980.

32. Kirkpatrick, Allan T., "Wave Mechanics of Inclined and Rotating Liquid Films," PhD Thesis, Department of Mechanical Engineering, M.I.T., September, 1980.

33. Incropera, Frank P. et al., Fundamentals of Heat and Mass Transfer, John Wiley & Sons, Inc., New York, New York, 1985.

34. Collier, John G., Convective Boiling and Condensation, 2nd edition, McGraw-Hill, Berkshire, UK, 1981.

35. Espig, Hans, et al., "Waves in Thin Liquid Layer on a Rotating Disk," Journal of Fluid Mechanics, vol. 22., part 4, 1965.

36. Fox, Allen G., "Receiver Preliminary Design," Department of Mechanical Engineering, M.I.T., 1986.

37. Fox, Allen G., "Receiver Concepts for Solar Space Power system," Department of Mechanical Engineering, M.I.T., 1986.

38. Lurio, Charles A., "An Evaluation of Solar Mercury Rankine Space Power," Masters Thesis, Depart ment of Aeronautics and Astronautics, M.I.T., 1983.

39. Burns, R. K., "Preliminary Thermal Performance Analysis of Solar Brayton Heat Receiver," NASA TN D-6268, March, 1971.

40. "TES/Receiver," Sundstrand Corporation, October, 1984.

41. Lacy, Dovie E. et al., "Selection of High Temperature Thermal Storage Materials for Advanced Solar Dynamic Space Power Systems, IECEC 879223, 1987.

42. Weast, Robert C., Editor, Handbook of Chemistry and Physics, 53rd edition, The Chemical Rubber Company, Cleveland, Ohio, 1972.

43. Rohsenow, Warren, Handbook of Heat Transfer, McGraw-Hill, NY 1973.

44. Classnote from MIT Course 16.042: Heat and Mass Transfer, Fall, 1986.

45. Reynolds, W. C., Thermodynamic Properties in SI," Department of Mechanical Engineering, Stanford University Press, 1979.